FIRST-PRINCIPLES INVESTIGATION OF THERMODYNAMIC AND KINETIC PROPERTIES IN TI-H SYSTEM AND B2-NIAL COMPOUND: PHASE STABILITY, POINT DEFECT COMPLEXES AND DIFFUSION

By

Qingchuan Xu

A dissertation submitted in partial fulfillment
of the requirements for the degree of
Doctor of Philosophy
(Materials Science and Engineering)
in The University of Michigan
2009

Doctoral Committee:

Assistant Professor Anton Van Der Ven, Chair
Professor Tresa M. Pollock
Assistant Professor Katsuyo Thornton
Assistant Professor Suljo Linic

2009

Acknowledgements

I would like to extend my deepest gratitude to my thesis advisor, Prof. Anton Van Der Ven, for his mentoring, support, encouragement and patience throughout my graduate study. The guidance of this gentleman has been outstanding. Further appreciation is due to the members of the dissertation committee, Prof. Pollock, Prof. Thornton and Prof. Linic, for their guidance and suggestions.

I gratefully acknowledge financial support from NSF, Grant No DMR-0605700 and DMR-0748516.

I would like to thank my fellow graduate students and research group members: Jishnu Bhattacharya, Jessica Bickel, and John C. Thomas, who have assisted in this work and created an enjoyable atmosphere within which to work. Also, I would like to thank Kevin Worth who has helped me solving many technical computer problems. Thanks are also extended to the staff of the Center for Advanced Computing in the university of Michigan for their valuable help and advice in parallel computing.

I also wish to thank my friends, who have been part of my life throughout graduate school, for their friendship and help whenever needed.

Thanks to my parents in law, Zhiru Hu (胡稚如) and Zhiming Chen (陈志铭) for their support and lavish gifts.

I thank my parents and sister, Chengqing Li (李承青), Zude Xu (许祖德), and Lichuan

Xu (许丽川) for their unwavering support throughout my life and graduate career.

Most of all, I express my deepest appreciation to my wife, Xingzhi Chen (陈幸之) whose understanding, unconditional support and love was crucial to make this all possible. Special thank goes to my daughter, Louisa (许葭轩), who made my graduate career more delightful and productive.

Table of Contents

List of Figures

List of Appendices

Chapter 1

Introduction

Understanding the thermodynamic and kinetic properties of most materials of technological importance is of critical importance in both theoretical and applied research. The conventional approaches to investigating the thermodynamic and kinetic properties are through experiments or empirical simulations that are based on experimental results. Although experiment is the most reliable and direct method to obtain thermodynamic and kinetic properties, it is sometimes difficult to conduct or time consuming. Fortunately, the developments in statistical mechanics and density functional theory (DFT) have made it possible to predict thermodynamic and kinetic properties from first-principles electronic structure calculations. It is now possible to calculate multi-component phase diagrams and finite temperature phase stability to a high degree of accuracy without any experimental results [1-12].

This thesis will demonstrate how macroscopic thermodynamic and kinetic properties of real materials at finite temperature can be predicted from first principles and obtain a deep microscopic insight into the macroscopic thermodynamic and kinetic properties. The approach relies on statistical mechanical techniques that link electronic structure calculations to relevant free energies and phenomenological kinetic constants such as diffusion coefficients. The two systems we are interested in are the Ti-H system, which is a representative of interstitial solids, and the Ni-Al system, which is a representative of substitutional solids; both play very important roles in industrial applications.

1.1 Thermodynamics in Ti-H system

The tendency of a solid to form hydrides makes it a potential hydrogen storage material. This tendency also makes structural materials susceptible to hydrogen embrittlement. An understanding of the thermodynamics and kinetics of hydride formation is therefore required in the design of new hydrogen storage materials as well as alloys that are resistant to hydrogen embrittlement.

The insertion of hydrogen into a host material for storage purposes is often accompanied by phase transformations, whereby a hydride phase consumes the original host phase [13]. In a good hydrogen storage material, these phase transformations proceed reversibly and with minimal mechanical damage that may arise from differences in volume between the various phases participating in the transformation.

Hydrogen embrittlement has several origins depending on the environment and loading conditions. These include: (i) the formation of brittle hydrides [14-16], (ii) a hydrogen induced reduction in cohesive strength of the solid [17-20], and (iii) hydrogen enhanced local plasticity (HELP) whereby the presence of hydrogen atoms lubricate dislocation glide [21-23]. In a particular alloy, all three mechanisms may play a role, with hydride formation followed by hydride cleavage typically dominating under slow loading rates and the HELP mechanism dominating at high strain rates [15]. The change in mechanism with loading rate arises from kinetic factors that prevent the rapid formation of brittle hydride phases as the solid is strained.

A first step to understanding hydride formation in hydrogen storage materials or during mechanical loading in structural materials is a determination of hydride phase stability. Often hydrides are compounds in which hydrogen orders over interstitial sites of the host material. Not all hydrides are stoichiometric, though, and can exhibit considerable configurational disorder.

Since hydrogen is the lightest element, zero-point vibrational energy is potentially also important in determining hydride phase stability. Finally, hydrides often form in the solid state, where coherency strains and internal stresses may alter relative stabilities of various hydride phases.

This thesis investigates different factors that determine hydride phase stability from first principles. We focus on hydride formation in Ti, an important structural material that is well known to be susceptible to hydrogen embrittlement [15, 24-26]. Ti based alloys are used as structural components in aircraft and exhibit exceptional mechanical properties as well as corrosion resistance. Nevertheless, the unique bonding properties between Ti and hydrogen make Ti-alloys susceptible to hydrogen embrittlement. The mechanisms of hydrogen embrittlement in Ti have their origin in the interaction between Ti and hydrogen at the electronic and atomic scale, making their study ideally suited for a first-pinciples investigation.

While Ti in and of itself is currently not considered a viable hydrogen storage material, the thermodynamic and kinetic principles that dominate hydride formation in this metal are similar to those occurring in well-known hydrogen storage materials such as Ni-based alloys (with rare-earth elements [27] or with transition metal ions [28]). Furthermore, Ti can serve as an alloying element in Ni and Fe based metal hydride storage materials [29,30], while the addition of $TiCl_3$ to $NaAlH_4$, a promising hydrogen storage material, has been shown to significantly enhance its hydrogen (de)-sorption reactions [31].

The hydrides that form in Ti are crystallographically identical to those that form in Zr [32,33], an important component in nuclear fuel rod cladding. In pure α-Ti (hcp), three hydride phases can form [34-37]: (i) δ-TiH_{2-z} (where z ranges between 0 and 0.5), (ii) ε-TiH_2, which is a tetragonally distorted form of δ and (iii) γ-TiH. We explore the role of configurational degrees of freedom, vibrational degrees of freedom and coherency strains in affecting hydride phase

stability with a particular focus on the relative stability of γ-TiH, as this hydride is believed to be metastable but is nevertheless observed experimentally in the form of coherent precipitates [35-37]. We also explore the nature of the cubic to tetragonal phase transformation of TiH_2 that occurs around room temperature [34].

1.2 Diffusion in Ni-Al system

NiAl based alloys are of importance in aircraft industry. The gas turbine blades are coated with the functional layers that protect the structural component (Ni-based superalloy) from the combustion environment. This protection consists of a chemical barrier made of a thin layer of Al_2O_3 and outer thermal barrier made of a thicker layer of yttria-doped ZrO_2 [150]. The chemical barrier protects the core against in –diffusion of deleterious elements from the combustion environment, while the thermal barrier keeps the structural core within an acceptable temperature range. In addition to the chemical and thermal barriers, a bondcoat is also required to both form and subsequently adhere the Al_2O_3 thermally grown oxide (TGO) chemical barrier to the super-alloy structural core. An important class of bond coats is made of B2-NiAl based alloys. The bond coat is expected to withstand creep and to serve as a diffusion barrier or sink to refractory elements such as Mo, Re, Ta and W from the superalloy core [38].

Since the B2-NiAl based bond coat is between a Ni-rich superalloy substrate and the Al-rich TGO chemical barrier, large concentration gradient are present, and the system becomes susceptible to interdiffusion, which can lead to functional degradation. Often a thin layer of Pt is placed between the nickel aluminide and the TGO adding to the complexity of interdiffusion phenomena [39,40]. In fact, net fluxes of vacancies due to the Kirkendall effect associated with interdiffusion in substitutional solids can lead to local swelling. Interdiffusion also affects the

superalloy substrate, producing a diffusion-affected zone there that locally degrades its mechanical properties [38].

This thesis tries to understand the interdiffusion phenomena within the B2-NiAl compound from first-principles and these insights will form a solid basis from which to investigate ternary-alloying elements that suppress local swelling due to net fluxes of vacancies in the future.

B2 NiAl is a unique intermetallic in that it can accommodate remarkably high concentrations of vacancies and anti-site defects. Its crystal structure is isomorphic to CsCl, which is a bcc based ordered compound consisting of two cubic sublattices, with Ni occupying one cubic sublattice and Al the other (Figure 2-1). While B2 NiAl has a simple crystal structure, the defects that accommodate off-stoichiometry in B2-NiAl can be quite complex [41-44]. At finite temperature and for off-stoichiometric compositions, intrinsic defects are created that include anti-site disorder (Ni on the Al sublattice and vice-versa) as well as vacancies. Excess Ni is realized with Ni anti-site defects on the Al sublattice while excess Al is achieved through the creation of vacancies on the Ni sublattice [41-44]. Experiment [41] and mean field predictions [42-44] have indicated a strong asymmetry in the dominant defects as a function of the alloy composition relative to the stoichiometric NiAl composition. Although Al atoms can occupy the Ni sublattice, they do so very rarely and the overwhelming majority of defects on this sublattice are vacancies, which can reach concentrations of several percent in Al-rich B2 compounds [41-43]. The Al sublattice, in contrast, only accommodates vacancies at very low concentrations while its Ni concentration can be substantial [41-43]. The high concentrations of point defects in B2-NiAl can lead to the formation of a variety of long-lived defect clusters, including the triple

defect, which consists of a pair of vacancies on the Ni-sublattice next to a Ni antisite on the Al sublattice.

Point defects and defect clusters often play an important role in mediating atomic diffusion [45,46]. However, the complexity of the defect structure of B2-NiAl as a function of alloy concentration has made a comprehensive understanding of atomic transport in this compound very difficult. A variety of atomic hop mechanisms have been proposed and studied in B2-NiAl, ranging from simple atom-vacancy exchanges to complex hop sequences that involve defect clusters [42,43,47-67]. As any nearest neighbor hop in B2-NiAl results in a local disordering of the compound, complicated hop sequences have been proposed that result in the net migration of atoms and vacancies without disrupting the B2-ordering. Several candidate diffusion mechanisms in this system include next-nearest-neighbor (NNN) vacancy jumps, six-jump-cycle (6JC) [47,63,66] that is also called Huntington-McCombie-Elcock (HME) mechanism, the anti-structural-bridge (ASB) mechanism [52], and the triple-defect mechanism [49,67].

Under the NNN vacancy mechanism a vacancy is jumping along one specific sublattice by exchanging with NNN atoms. This mechanism is equivalent to a normal vacancy mechanism on the simple cubic lattice formed by Ni or Al atoms. In contrast to the NNN mechanism, the six-jump cycle mechanism involves only nearest neighbor (NN) jumps of vacancies. It includes six successive cycle displacements of a vacancy between the two sublattices [47,66]. After completing the six-jump cycle, a vacancy on Ni sublattice site exchanges its position with a Ni atom also on an Ni-sublattice site; at the same time two Al atoms on the Al sublattice sites exchange positions with each other. The degree of order in the initial and final states of the lattice does not change. Kao *et al* proposed another important diffusion mechanism, referred to as the

anti-structural bridge mechanism (ASM) [52], which involves the migration of a vacancy along a percolating network of anti-site atoms, thereby avoiding any increase in local disorder. This mechanism requires sufficient anti-site atoms and is only expected to become viable for alloy concentrations that deviate from the NiAl stoichiometry. Frank *et al* proposed a mechanism that relies on the net migration of a triple defect, causing a direct exchange of a Ni atom and an Al atom [49,67]. Combining with the ASB mechanism, Frank used the triple-defect mechanism to explain the experimental observation of Ni diffusion behavior and he also excluded the NNN jump from the dominant diffusion mechanism [49]. However, in a recent embedded atomic model (EAM) study of diffusion mechanism in NiAl, Mishin questioned Frank's exclusion of NNN mechanism and pointed out that NNN jumps of a Ni vacancy have a low enough energy barrier and high enough rate constant to be considered as a plausible mechanism of Ni diffusion that can operate concurrently with other mechanisms [58]. From the above brief summary of the diffusion mechanisms in the NiAl system we can see that the diffusion process in this system is very complex and several atomic mechanisms can operate in NiAl concurrently and may depend on the temperature and composition.

A first step to understanding diffusion in B2-NiAl is a characterization of the dominant hop mechanisms that enable atomic transport. The importance of a particular hop mechanism is determined by (i) its migration barrier and (ii) the concentration of point defects and defect complexes that are needed to mediate the hop. Previous theoretical investigations of defects in B2-NiAl, while using a variety of methods to calculate defect formation energies (ranging from empirical potential methods to first-principles methods) always relied on a mean field approximation to estimate finite temperature defect concentrations [42,43,44,58]. This approach neglects interactions among defects, and is therefore valid only when defect concentrations are

very low. Furthermore, it cannot provide accurate predictions for the concentration of important diffusion mediating defect complexes, whose existence is a result of interactions between point defects.

In this thesis, we expand on previous studies of defects and atomic diffusion in B2-NiAl [42-44,47-67] and systematically analyze hop mechanisms from first principles to identify those with low migration barriers. This analysis will provide a deep understanding of proposed diffusion mechanism, lead to corrections of hop sequences and find possible new hop sequences. We have calculated the concentrations of point defects and defect complexes in B2-NiAl compounds at finite temperature by rigorously accounting for interactions among point defects with a cluster expansion in Monte Carlo simulations. The explicit inclusion of interactions among point defects enabled an accurate first-principles prediction of the concentrations of diffusion mediating complexes as a function of alloy concentration and sheds light on the relative importance of viable atomic hop mechanisms in B2-NiAl. Our calculations of defect cluster concentrations suggest the importance of different diffusion hops that are mediated by these defect clusters. Based on this information, we conducted kinetic Monte Carlo simulations to obtain the tracer diffusion coefficients, and further to calculate intrinsic diffusion coefficients and inter-diffusion coefficients for B2-NiAl compound.

The thesis is structured as follows. In chapter 2, we describe the first-principles methodology to investigate the thermodynamic and kinetic properties of Ti-H and Ni-Al systems. We will describe a cluster expansion approach to rigorously account for interactions among point defects within Monte Carlo simulations and show how thermodynamic and kinetic properties can be determined with grand canonical Monte Carlo simulations and kinetic Monte Carlo simulation. After chapter 2, we investigate in chapter 3 the thermodynamic properties of

the Ti-H system, such as phase stability, the effect of vibrational degrees of freedom, the effect of strain on the phase stability and the site preference of hydrogen atoms within Ti host. After investigating an interstitial solid, we will investigate a substitutional solid, B2-NiAl in chapter 4. There we systematically analyze migration barriers of important atomic hop mechanisms in B2-NiAl from first principles and conduct a comprehensive analysis of point defects and defect cluster concentrations at finite temperature using Monte Carlo simulations applied to a cluster expansion for B2-NiAl. All this information was used to conduct kinetic Monte Carlo simulations (chapter 5), which incorporated all well-known diffusion mechanisms, to obtain the tracer diffusion coefficients for B2-NiAl compound and to compare the relative importance of various diffusion mechanisms. Finally, in chapter 6 the calculations of self-diffusion coefficients and interdiffusion coefficients are presented and the link between these diffusion coefficients and the specific defect characteristic of B2-NiAl compound are investigated. Chapter 7 concludes the thesis.

Chapter 2

Thermodynamics and kinetics from first-principles

Thermodynamic and kinetic properties of solids are macroscopic properties that are collectively determined by the underlying atomic interactions. An ultimate understanding of these macroscopic properties should theoretically come from the understanding of the behavior of elementary atoms that form the solids. This means that in theory we should solve the quantum mechanical equations that govern the behavior of these elementary particles in the solids to understand the thermodynamic and kinetic properties. However, this is extremely difficult in practice. Fortunately, statistical mechanics serves as a bridge between the atomic-scale description of solids and macroscopic thermodynamic and kinetic properties and makes it possible to predict thermodynamic and kinetic properties from first principle. Over the past two decades some approaches have been developed to qualitatively or quantitatively predict thermodynamic and kinetic properties from first principle. This chapter will describe the methods and procedures employed to predict thermodynamic and kinetic properties.

2.1 The general procedure to predict thermodynamic and kinetic properties.

It is well known from statistical mechanics that the macroscopic thermodynamic and kinetic properties of a solid are the weighted average of values of the specific property within each microstate that the solid samples. Each microstate *s* has an energy E_s associated with it which is an eigenvalue of the Schrodinger equation of the solid. The weight, according to

statistical mechanics then, is the probability that a system is in a particular state *s*, and is given by [68,69]

$$P_s = \frac{\exp(-E_s / k_B T)}{Z}, \tag{2.1}$$

where k_B is the Boltzmann's constant, T is the absolute temperature and Z is the partition function defined as

$$Z = \sum_s \exp(-E_s / k_B T). \tag{2.2}$$

Equation (2.1) represents a distribution function that assigns the relative importance of different microstates in determining thermodynamic averages and reflects the fraction of time that a solid resides in each microstate *s*. In this way, average thermodynamic properties can be evaluated as

$$A = \sum_s A_s P_s, \tag{2.3}$$

where A is a macroscopic thermodynamic quantity and A_s is the value of that quantity when the solid is in microstate *s*. Also, a prediction of phase stability requires a comparison of free energies of different phases at finite temperature. The free energy G of a system for example is formally related to the partition function Z according to [69]

$$G = -k_B T \ln Z \tag{2.4}$$

The full evaluation of Eq. (2.1) – (2.4) require the knowledge of E_s for all excited states *s* of the solid, which includes configurational, vibrational, and electronic excitations. [First-principles energies are usually calculated at zero pressure p, and the pV_s term that should appear in the exponential of Eq. (2.1) and (2.2), where V_s is the volume of excited state *s*, can then be ignored.] In the system studied in this thesis, configurational degrees of freedom arise from all the possible ways of distributing hydrogen over the interstitial sites of the metal hosts in Ti-H system and all possible arrangements of Ni atoms, Al atoms and vacancies in Ni-Al system.

Often, vibrational and electronic excitations are neglected in first-principles investigations of thermodynamic and kinetic properties in multicomponent solids [2,4,6,7,11,95-98]; however, due to the low mass of hydrogen atoms in Ti-H system, zero-point vibrational energy can be important [99]. Thus, in this thesis we will neglect electronic excitations for both Ti-H system and investigate thermodynamic properties with and without vibration. For Ni-Al system, only configurational degrees of freedom are considered when evaluating thermodynamic and kinetic properties.

The excitation energies E_s should be calculated from first principles, but since the number of excitations is astronomically large, it is necessary to resort to a model that extrapolates first principle energies to allow the calculation of energies for any configuration. Once we can calculate the energies for arbitrary configurations, a statistical mechanical technique such as Monte Carlo simulations can be used to evaluate the thermodynamic and kinetic properties at finite temperature. Hence the methods used in this thesis to calculate first principles thermodynamic and kinetic properties in Ti-H and Ni-Al systems can be divided into three steps [2,70] that will be described in more detail in the next three sections and can be summarized as follows.

(i) First a variety of first principles total energies are calculated for various arrangements of H atoms within Ti hosts and various arrangements of Ni atom, Al atom and vacancies in Ni-Al system.

(ii) These energies are then used to parameterize a cluster expansion. An optimized cluster expansion enables an accurate and efficient calculation of the total energy of any configuration.

(iii) The cluster expansion is then used in Monte Carlo simulation to calculate thermodynamic and kinetic properties.

In section 2.2 we will briefly describe density functional theory [71] used to calculate the energy of the solid from first-principles. These energies were then used to determine the coefficients of a cluster expansion [1] for a particular system, as will be reviewed in section 2.3. Once the cluster expansions were constructed, thermodynamic and kinetic properties were calculated with Monte Carlo simulations [72] that will be described in section 2.4. Finally, due to the importance of vibrational degree of freedom in Ti-H system, a short description of the approach to calculate vibrational free energy is present in section 2.5.

2.2 First principle total energies

Total energies are essential inputs for any analysis of phase stability and diffusion. These energies must be calculated from first principles, that is, at 0K by solving the many-body time-independent Schrodinger equation:

$$\hat{H}\Psi = E\Psi, \tag{2.5}$$

where Ψ is the many-body wavefunction for the electrons, E is the total energy for the solid, and $\hat{H}$ is the Hamiltonian operator for the system of electrons and nuclei, which is defined as:

$$\hat{H} = -\frac{\hbar^2}{2m_e}\sum_i \nabla_i^2 + \sum_{i,I}\frac{Z_I e^2}{\left|\vec{r}_i - \vec{R}_I\right|} + \frac{1}{2}\sum_{i\neq j}\frac{e^2}{\left|\vec{r}_i - \vec{r}_j\right|} - \sum_I \frac{\hbar^2}{2M_I}\nabla_I^2 + \frac{1}{2}\sum_{I\neq J}\frac{Z_I Z_J e^2}{\left|\vec{R}_I - \vec{R}_J\right|}, \tag{2.6}$$

where e and m_e are the charge and mass of electrons respectively, Z_I and M_I are the charge and mass of nuclei respectively, $\vec{r}_i$ is the position of electron i and $\vec{R}_I$ is the position of nuclei I, $\hbar$ is the Plank constant/(2π)[73-75]. The first term in Eq (2.6) is the kinetic energy operator for the electrons, the second term is the potential energy due to the interaction between electrons and

nuclei, the third term is the electron-electron interaction, the fourth term is the kinetic energy operator for the nuclei and the final term is the classical nuclei-nuclei interaction. The fourth term is typically neglected according to the Born-Oppenheimer adiabatic approximation [76] since the inverse mass of the nuclei $1/M_I$ is very small. The total energy then is the expectation value of the Hamiltonian [75],

$$E = \frac{\left\langle \Psi \middle| \hat{H} \middle| \Psi \right\rangle}{\left\langle \Psi \middle| \Psi \right\rangle} \tag{2.7}$$

This many-body problem is impossible to solve for realistic solids [75,78]. Many approximations have been proposed to solve this problem, for example the Hartree [77] and the Hartree-Fock approaches [79]. However, the Hatree approach ignores both exchange and correlation effects [78], while the Hatree-Fock approach ignores the correlation effect [75]. The exchange effect is due to the Pauli exclusion principle, which indicates that around a spin-up (down) electron other nearby spin-up (down) electrons will be repelled. The correlation effect is caused simply by electrostatic repulsion between electrons [78]. In order to tackle this difficulty, Kohn and Sham [75,80] replaced the interacting many-body system with an independent-particle system where all many-body effects arising from exchange and correlation are grouped into an unknown exchange-correlation energy E_{xc}. This approach leads to Kohn-Sham Schrodinger-like equations [75,84]:

$$\left(-\frac{\hbar^2}{2m_e}\nabla^2 + V_{ext}(\vec{r}) + V_{Hartree}(\vec{r}) + V_{xc}(\vec{r}) \right) \psi_i(\vec{r}) = \varepsilon_i \psi_i(\vec{r}) \tag{2.9}$$

where ψ_i is the wave function of electronic state *i,* ε_i is the eigenvalue, V_{ext} is the external potential due to the nuclei and any other external fields, V_{Hatree} is the Hartree potential of the electrons given by $e^2 \int \frac{n(\vec{r})}{|\vec{r} - \vec{r}'|} d^3r$ [84], where $n(\vec{r})$ is the electronic density given by $2\sum_i |\psi_i(\vec{r})|^2$

[84]. The exchange-correlation potential, V_{xc}, is given by the functional derivative $\frac{\delta E_{xc}}{\delta n(\vec{r})}$ [84]. V_{xc} contains all quantum mechanical effects of the many-body problem and several well-known approximations for V_{xc} exist. Equation (2.9) has the form of independent-particle equations with a potential that must be found self-consistently with the resulting density. Equation (2.9) are independent of any approximation to the exchange-correlation functional E_{xc}, and would result in the exact ground state energy and density for the interacting system provided the exact exchange-correlation functional E_{xc} were known.

Although the exact form of exchange-correlation functional is unknown, it can be approximated as a local or nearly local functional of the electron density. Two well-known approximations for the exchange-correlation functional are the local density approximation (LDA) [80] and the generalized-gradient approximation (GGA) [80-83]. There are several different parameterizations of the GGA. Two widely used are the form of Perdew and Wang (PW91) [85] and the form of Perdew, Burke, and Enzerhof (PBE) [86]. In this thesis, we used PBE for Ti-H system and PW91 for Ni-Al system.

2.2.1 The pseudopotential method

The Kohn-Sham approach transfers the many-body problems into an equivalent single-particle problem. In general, there are many approaches to solving Kohn-Sham equations. The most common today are linearized augmented plane wave (LAPW) [87] method and the pseudopotential method [84,88]. The LAPW method is the most accurate and general method for electronic structure calculations but it is computationally demanding. It combines localized and delocalized basis sets for the electronic wavefunction. In this thesis we used a pseudopotential

method based on the projector augmented wave (PAW) method [89], which is fast and relatively accurate compared to the LAPW approach.

The pseudopotential method typically uses a plane wave basis set for the electronic wavefunctions and is based on the fact that physical properties of solids depend on the valence electrons to a much greater extent than on the core electrons [75,84,88]. Thus, the pseudopotential approach replaces the wavefunction near nuclei region with a smoother pseudo-wavefunction in such a way that the valence states are reproduced, but the core states with rapid variations are removed. This means that ionic potential and pseudopential are identical only outside the core electron region [75,84,88]. This way, a much smaller number of plane-wave basis functions are needed to expand the electronic wave function. As a variation based on the pseudopotential approach, the projector augmented wave (PAW) approach retains the entire set of all-electron core functions along with smooth parts of the valence functions. As a result the PAW approach has the advantage of both pseudopotential method (fast) and full-electron method (accurate) [75,89].

In this thesis, we perform the first-principle total energy calculations with the Vienna *ab initio* simulation package (VASP) [90,91]. This code implements the PAW pseudopotentials [89,92], which allows for plane wave expansions with significantly lower energy cutoffs than traditional pseudopotentials meanwhile achieving a relatively high accuracy, making it possible to investigate large and complicated systems.

2.3 Cluster expansion

As we have mentioned in section 2.1, in theory the energies of all possible microstates should be calculated from first principle in order to obtain the thermodynamic properties of a

system. However, it is impossible to calculate all these energies from first principle due to the huge number of them. So, we first calculated the energies of some configurations from first principle using the method described in section 2.2, then using these energies to fit a model that in turn can be used to calculate the energy of any configuration. This model is called cluster expansion [1]. Furthermore, cluster expansion can capture the interaction among point defects and atoms. This is very important for a system like B2-NiAl [93], which can accommodate high concentration of many types of point defects and consequently the interaction among these point defects cannot be neglected. Previous theoretical investigations of thermodynamic properties such as equilibrium point defect concentration in B2-NiAl compound, while using a variety of methods to calculate defect formation energies (ranging from empirical potential methods to first-principles methods) always relied on a mean field approximation to estimate finite temperature defect concentrations [42-44]. This approach neglects interactions among defects, and is therefore valid only when defect concentrations are very low. Furthermore, it cannot provide accurate predictions for the concentration of important diffusion mediating defect complexes, whose existence is a result of interactions among point defects. Consequently, a cluster expansion is needed to efficiently calculate energies of any configurations and to capture interactions among atoms and defects.

2.3.1 Conventional cluster expansion.

We will use Ti-H system as an example to explain binary cluster expansion formalism [94]. Assigning H atoms to interstitial sites in Ti host forms Ti-H hydrides. This means that an interstitial site can be occupied by either H atom or a vacancy. It is useful to introduce the occupation variable σ_i to each interstitial site that is +1(-1) if the interstitial site is occupied by H

atom (a vacancy). Consequently, by assigning an occupation variable σ_i to each interstitial hydrogen site *i* within the Ti host, it is possible to uniquely specify a particular hydrogen-vacancy configuration with the collection of occupation variable $\vec{\sigma} = \{\sigma_i\}$. Although the hydrogen atoms rarely reside exactly at these rigorously defined crystallographic sites, there is a one-to-one correspondence between each hydrogen atom and a crystallographic site. Sanchez *et al.* [1] showed that any property that depends on configuration could be expanded in terms of polynomials of the discrete occupation variables σ_i. The dependence of the fully relaxed energy on configuration, for example, then takes the form [1,93,94,106,107]

$$E(\vec{\sigma}) = V_0 + \sum_i V_i \sigma_i + \sum_{i,j} V_{ij} \sigma_i \sigma_j + \sum_{i,j,k} V_{ijk} \sigma_i \sigma_j \sigma_k + \cdots, \tag{2.10}$$

where the indices *i, j, k…* correspond to a collection of interstitial sites that form a cluster such as a pair cluster, a triplet cluster, etc. The coefficients V_0, V_{ij}, and V_{ijk} are called effective cluster interactions (ECI) and are constants. Equation (2.10) is referred to as a cluster expansion.

Equation (2.10) can be viewed as a generalized Ising model Hamiltonian including not only nearest neighbor pair interactions, but also all other pair and multibody interactions beyond the nearest neighbors. Equation (2.10) extends over all possible clusters of sites. From a practical point of view, however, it must be truncated after some maximal sized cluster, i.e. (2.10) is useful if it converges rapidly and there exists a maximal cluster such that all ECI corresponding to clusters larger than the maximal cluster are negligibly small. Experience indicates that convergence depends on the particular system and in general, the lower order clusters such as points or pairs within a limited range will have larger contribution than higher order clusters. Although Ti host, which is fixed, does not contribute to the configurational degrees of freedom and consequently there is no explicit reference to them in the cluster expansion, the cluster expansion describes the energy of the whole crystal since in Eq. (2.10) $E(\vec{\sigma})$ is the fully relaxed

energy of the whole crystal. The ECIs are simply linear expansion coefficients, which implicitly incorporates complicated interactions among atoms and vacancies and it is difficult to give them a simple physical interpretation.

2.3.2 Determination of ECI

The ECI of a cluster expansion of the configurational total energy $E(\vec{\sigma})$ need be determined from first principles. This then enables the calculation of thermodynamic properties with, for example, Monte Carlo simulations. Several techniques have been used to determine ECI from first principles, and most are based on a least squares fit of a truncated cluster expansion to the first-principles energies of different configurations [2,70]. The ECI obtained with this approach depends both on the truncation of Eq. (2.32) and on the selection of configurations used in the fit.

The cross-validation (CV) score is a useful criterion in selecting an optimal set of clusters [6]. The CV score is a measure of the ability of the cluster expansion to predict energies not included in the fit. There are different definitions of the CV score: the leave-one-out CV (LOO-CV) and the leave many out in which Monte Carlo sampling is used, which is called Monte Carlo CV (MCCV) [100,101]. Many investigations have shown that the performance of MCCV is better than LOO-CV in general. Especially, Shao pointed out that LOO-CV is too conservative in the sense that it tends to select unnecessarily large model and the performance of Monte Carlo Leave-Many-Out CV (MCCV) is stable and much better than LOO-CV [101]. This indicates that LOO-CV tends to select much more clusters many of which are not necessary than MCCV does. In this thesis, we will use the Monte Carlo CV to select the optimal cluster model unless it is impossible to explore it in the case where we have few energies to fit the model and LOO-CV is

used under this situation.

Suppose the energies of n configurations have been calculated from first principles. The algorithm involves the random removal of n_v configurations from the sample followed by a fit of the ECI to the remaining n_c structures. This procedure is repeated b times. The definition of the MCCV score is

$$(MCCV)^2 = \frac{1}{n_v b}\sum_{\vec{\sigma}}^{n_c}\left(\hat{E}(\vec{\sigma}) - E(\vec{\sigma})\right)^2 , \tag{2.11}$$

where $E(\vec{\sigma})$ is the calculated first-principles energy of a structure having a configuration $\vec{\sigma}$, and $\hat{E}(\vec{\sigma})$ is the cluster expansion predicted energy of $\vec{\sigma}$. Since it is impossible to enumerate all possible combinations of clusters, we search for an optimal set by using a genetic algorithm [102]. In this algorithm, a bunch of combinations of clusters were initially randomly generated to form a pool (parents pool). Then the MCCV score was evaluated for each combination in the pool. Based on these MCCV scores, a fraction of combinations that have best MCCV were retained to the next generation and the rest were replaced by the same number of new combinations (children), which were formed by the mating of parents. In the mating process, the parent with better MCCV score has the higher probability of passing its gene bit (inclusion of a specific cluster or not) on to the child than the parent with worse MCCV score. In this way, the preferred transfer of better genetic information is ensured. Once the new parent pool was formed, the same procedure was repeated.

The algorithm implemented in this work uses a slightly different criterion to pick clusters than that of Hart et al [102]: pairs are chosen in the order of their length while only triplet, quadruplet and larger clusters are chosen if their largest inter-site distance is less than the largest pair already included in the expansion. Once the optimal set of clusters is obtained, we use the

energies of all *n* structures to obtain the values for the optimal ECI. The resultant ECI can then be implemented in Monte Carlo simulations to calculate finite temperature free energies.

2.3.3 Local cluster expansion

Although in theory we can use conventional cluster expansion to evaluate the configurational total energy for any configuration of a multi-component solid such as ternary system, it sometimes becomes intractable and unnecessary. For example, While B2 NiAl is a binary alloy; the presence of large vacancy concentrations on the Ni sublattice suggests that it should be treated as a ternary system to accurately account for all relevant configurational degrees of freedom [103]. However, a ternary cluster expansion means we will encounter a large number of configurations (if there are M crystal sites, then each site can be occupied by 3 possible elements so there are 3^M possible configurations) and most of them are unnecessary for the B2-NiAl compound given its specific defect character (e.g. the configurations with large concentration of aluminum vacancies are unnecessary since aluminum vacancies are very dilute in B2-NiAl alloy).

We can avoid an explicit ternary cluster expansion of the configurational energy of B2-NiAl by taking advantage of available insight about the dominant defects of this compound. As we have mentioned in the chapter 1, although Al atoms can occupy the Ni sublattice, they do so very rarely and the overwhelming majority of defects on this sublattice are vacancies, which can reach concentrations of several percent in Al-rich B2 compounds [41-43]. The Al sublattice, in contrast, only accommodates vacancies at very low concentrations while its Ni concentration can be substantial [41-43]. On each sublattice, we can therefore distinguish between *dominant components* (Ni and vacancies on the Ni-sublattice, Al and Ni on the Al-sublattice) and *minor*

defects (Al on the Ni sublattice, vacancies on the Al sublattice). The interactions among the dominant components are conveniently captured with a binary cluster expansion Eq. (2.10), in which to each Ni-sublattice site *i*, we assign the occupation variable τ_i, which is +1 if the site is occupied by Ni and -1 if it is vacant; to each Al-sublattice site *j*, we assign the occupation variable δ_j, which is +1 if it is occupied by Ni and -1. If the concentrations of the minor defects are sufficiently low that they rarely if ever interact with each other, we can account for their configuration dependent formation energies with a local cluster expansion [97,104,105].

Local cluster expansions can supplement the binary coupled-sublattice cluster expansion to describe the configurational energy of B2-NiAl in the presence of minor defects [93]. While interactions among minor defects do not need to be accounted for, interactions between a minor defect and the dominant components of both sublattices of B2-NiAl are important, as the minor defect will energetically prefer particular local arrangements and concentrations of the dominant components over others. Consider, for example, the presence of an isolated vacancy on the Al sublattice [93]. A convenient quantity to parameterize with a local cluster expansion is an effective minor-defect formation energy [93,97]:

$$\Delta E_i^{V_{Al}} = E_i^{V_{Al}}(\vec{\sigma}) - \frac{1}{2}[E_i^{Al_{Al}}(\vec{\sigma}) + E_i^{Ni_{Al}}(\vec{\sigma})] \tag{2.12}$$

where $E_i^{V_{Al}}(\vec{\sigma})$ is the energy of the crystal with configuration $\vec{\sigma}$ but with a vacancy, V_{Al}, occupying site *i* of the Al sublattice. The energies $E_i^{Al_{Al}}(\vec{\sigma})$ and $E_i^{Ni_{Al}}(\vec{\sigma})$ are of the crystal with configuration $\vec{\sigma}$ but with site *i* of the Al sublattice occupied by Al and Ni respectively. Both $E_i^{Al_{Al}}(\vec{\sigma})$ and $E_i^{Ni_{Al}}(\vec{\sigma})$ can be calculated with the binary coupled-sublattice cluster expansion, Eq. (2.10). The effective minor-defect formation energy $\Delta E_i^{V_{Al}}$ depends only on the arrangement

of Ni, Al and vacancies *around* site *i* and can therefore be parameterized with a local cluster expansion according to

$$\Delta E_i^{V_{Al}}(\vec{\sigma}) = L_o + \sum_j L_j \sigma_j + \sum_{j,k} L_{jk} \sigma_j \sigma_k + \ldots \tag{2.13}$$

where the sum over *j*, *k*, … extends over sites of clusters of B2-NiAl that do not include site *i* occupied by the minor defect. To calculate the energy of the B2-NiAl crystal with a vacancy on the Al sublattice, we can rearrange Eq. (2.12) to isolate $E_i^{V_{Al}}(\vec{\sigma})$ and evaluate $\Delta E_i^{V_{Al}}(\vec{\sigma})$ with the local cluster expansion, Eq. (2.13), and $\frac{1}{2}[E_i^{Al_{Al}}(\vec{\sigma}) + E_i^{Ni_{Al}}(\vec{\sigma})]$ with the binary coupled-sublattice cluster expansion, Eq. (2.10). A similar approach applies to the minor defect, Al, on the Ni-sublattice.

It should be noted that the cluster expansion technique is likely to fail if the magnitude of relaxation of many configurations is large, that is, the relaxed configuration is significantly deviated from the original unrelaxed structure. If this happens, the error of the fitting tends to be large and the cluster expansion loses its predictive ability.

2.4 Monte Carlo method

2.4.1 Conventional Monte Carlo simulation

The first-principles parameterized cluster expansion can be used in grand canonical Monte Carlo simulation to predict finite temperature thermodynamic properties, including the phase diagram, the equilibrium concentration of point defects as well as the concentration and nature of defect clusters. A Monte Carlo simulation samples various configurations with probability given by the Eq. (2.1). However, it is not computationally feasible to sum the $\exp(-E_s/k_BT)$ so as to determine *Z*. Fortunately, by using the Hastings-Metropolis algorithm we

can generate a sequence of successive states of a Markov chain whose sample space is the set of all possible configurations and stationary probabilities are P_s. [72,108] In such a Markov chain, the transition probability from state $\vec{\sigma}_i$ to state $\vec{\sigma}_j$ is given by

$$P_{ij} = 1, \qquad \text{if } \Omega(\vec{\sigma}_j) < \Omega(\vec{\sigma}_i) \tag{2.14}$$

$$P_{ij} = \exp\left(-\frac{\Omega(\vec{\sigma}_j) - \Omega(\vec{\sigma}_i)}{kT}\right) \qquad \text{if } \Omega(\vec{\sigma}_j) > \Omega(\vec{\sigma}_i) \tag{2.15}$$

where k is the Boltzmann's constant, T is the absolute temperature and $\Omega(\vec{\sigma}_i)$ is the grand canonical energy for configuration $\vec{\sigma}_i$, which is defined, for instance for Ni-Al system, as [93]

$$\Omega(\vec{\sigma}_i) = E(\vec{\sigma}_i) - N_{Ni}\tilde{\mu}_{Ni} - N_{Al}\tilde{\mu}_{Al} \tag{2.16}$$

where N_{Ni} and N_{Al} are the number of Ni and Al atoms in the crystal with configuration $\vec{\sigma}$ and $\tilde{\mu}_{Ni}$ and $\tilde{\mu}_{Al}$ are relative chemical potentials defined as $\tilde{\mu}_{Ni} = \mu_{Ni} - \mu_V$ and $\tilde{\mu}_{Al} = \mu_{Al} - \mu_V$, with μ_{Ni}, μ_{Al} and μ_V the chemical potentials of Ni, Al and vacancies respectively. Equation (2.14), (2.15) and (2.16) indicates that In a grand canonical Monte Carlo simulation at fixed temperature and chemical potentials, each Monte Carlo step involves the addition of one component at the expense of another if the change in the grand canonical energy $\Delta\Omega$ is negative or if $\exp(-\Delta\Omega/kT)$ is greater than a random number sampled from (0,1].

Contrary to the grand canonical Monte Carlo simulation, the canonical simulation conserves the number of atoms of different species and transfers the state by exchanging atoms at different lattice sites. The transition probability for Markov chain is similar to Eq. (2.14) and (2.15) with the exception that the grand canonical energies $\Omega(\vec{\sigma}_i)$ and $\Omega(\vec{\sigma}_j)$ should be replaced by the total energies $E(\vec{\sigma}_i)$ and $E(\vec{\sigma}_j)$.

In order to guarantee that the configurations sampled in a Monte Carlo simulation occur with probability given by the probability mass function Eq. (2.1), the Markov chain must run a

relatively long time before entering stationary state. Once it enters the stationary state, the metropolis algorithm guarantees that the configurations sampled occur with a probability given by the probability mass function (2.1), which is just the limit probability of the corresponding Markov chain. Hence thermodynamic properties such as the equilibrium point defect concentration can be obtained as simple arithmetic averages over the sampled configurations. In practice, in order to guarantee the Markov chain enters stationary state, several thousand MC steps are performed before the averaging.

The relative chemical potentials $\tilde{\mu}_i$ in Eq. (2.16) arise from the constraint in grand canonical Monte Carlo simulations that the number of crystal sites, M, remains fixed (i.e. $N_V=M-N_{Ni}-N_{Al}$). The relative chemical potentials $\tilde{\mu}_{Ni}$ and $\tilde{\mu}_{Al}$ serve as thermodynamic boundary conditions and are explicitly controlled in grand canonical Monte Carlo simulations.

When relating results from grand canonical Monte Carlo simulations to experiment, it is necessary to use thermodynamic boundary conditions that are consistent with experiment. In actual samples of B2-Ni_xAl_{1-x} alloys, with $x=N_{Ni}/(N_{Ni}+N_{Al})$, the experimentally controlled variables are usually N_{Ni} and N_{Al} as opposed to fixed number of crystal sites, M and fixed Ni and Al chemical potentials. Under experimental conditions, the number of crystal sites is not fixed and can vary through the creation or annihilation of vacancies at climbing dislocations, grain boundaries and surfaces. As a vacancy is a non-conserved species in a fully equilibrated solid, its chemical potential μ_V must be zero (provided vacuum is used as the vacancy reference state). The concentration of defects in B2-NiAl using grand canonical Monte Carlo simulations must therefore be calculated under the constraint that $\mu_V=0$. Appendix A shows how values for $\tilde{\mu}_{Ni}$ and $\tilde{\mu}_{Al}$ can be determined consistent with the constraint that $\mu_V=0$.

2.4.2 Free energy integration

A prediction of phase stability and the construction of phase diagram require a comparison of free energies of different phases at finite temperature. Free energies can be obtained from the results of Monte Carlo simulations by integrating the chemical potential. We will take the example of Ni-Al system to describe the procedure, which is contained in the Appendix A.

2.4.3 Kinetic Monte Carlo (KMC) simulation

The Monte Carlo simulation mentioned above is used to predict the equilibrium thermodynamic properties. In order to investigate the kinetic properties such as tracer diffusion coefficient for a crystal, kinetic Monte Carlo simulation is a powerful tool.

The statistical concept under the kinetic Monte Carlo is a continuous-time Markov chain, more specifically, a Poisson process. In this Poisson process the individual hop occurs instantaneously and the time between two successive hops is exponentially distributed with the mean $1/\Gamma_{tot}$, where Γ_{tot} is defined as [109]

$$\Gamma_{tot} = \sum_i \Gamma_i \tag{2.17}$$

where Γ_i is the migration frequency of hop i and Γ_{tot} is the sum of all individual probabilities Γ_i. For a specific hop, we can calculate the migration probability Γ_i within the harmonic transition state theory [110], which gives

$$\Gamma_i = \nu_{0i} \exp\left(-\frac{E_{mi}}{kT}\right) \tag{2.18}$$

where ν_{0i} is the vibration prefactor for hop i, E_{mi} is the activation energy for hop i required to move the hopping atom(s) from the initial stable state to the activated state, k is Boltzmann's

constant and T is the absolute temperature in degrees Kelvin. The attempt frequency ν_0 for a specific hop is calculated as

$$\frac{\prod_{i=1}^{3N-3} \nu_i}{\prod_{i=1}^{3N-4} \nu_i^*}, \tag{2.19}$$

where N is the number of sites involved in the hop (N=2 if the hop involves one atom and one vacancy, N=3 if the hop involves two atoms and one vacancy), ν_i is the normal vibration frequency at the stable state and ν_i^* is the normal vibration frequency at the activated state. According to the stochastic theory, each individual hop will occur with the possibility

$$P_i = \frac{\Gamma_i}{\Gamma_{tot}}, \tag{2.20}$$

A kinetic Monte Carlo simulation keeps track of atoms hop according to some diffusion mechanism specific to an interested system and the displacement of individual atom. Then the tracer diffusion coefficient of specie j is calculated as [111]

$$\frac{\left\langle \left(\sum_{\xi} [\Delta \vec{R}_{\xi}^{j}(t)]^2 \right) \right\rangle}{(2d)tN_{\xi}}, \tag{2.21}$$

where $\Delta \vec{R}_{\xi}^{j}(t)$ is the vector linking the end points of the trajectory of atom ξ of specie j after time t, N_{ξ} is the number of atoms of specie j, and d is the number of dimensions. In the simulation, the time Y between two consecutive hops can be defined as

$$Y = -\frac{\ln X}{\Gamma_{tot}} \tag{2.22}$$

where X is a uniformly distributed random variable between (0,1]. It ban be easily proved that Y, which is defined by Eq. (2.22), is an exponentially distributed random variable with the mean $1/\Gamma_{tot}$.

2.5 Vibrational free energy

As we have mentioned in section 2.1, due to the low mass of hydrogen atoms, zero-point vibrational energy can be important in Ti-H system. The simultaneous treatment of configurational and vibrational degrees of freedom is possible with a coarse graining procedure [112,113], where instead of cluster expanding the fully relaxed configurational energy $E(\vec{\sigma})$, a coarse grained free energy, $G(\vec{\sigma},T)$, is cluster expanded. $G(\vec{\sigma},T)$ accounts for vibrational and possibly electronic excitations, but is constrained to a fixed hydrogen-vacancy configuration $\vec{\sigma}$. Neglecting electronic excitations. $G(\vec{\sigma},T)$ can be calculated within the quasi-harmonic approximation using first-principles phonon densities of states for the solid having a configuration $\vec{\sigma}$ [113]. Phonon densities of states are accessible from first principles either with a linear response method [114] or a frozen phonon approach in which force constants are extracted from calculations of restoring forces on perturbed atoms within supercells [113,115]. The vibrational free energy at fixed volume, V, is related within the harmonic approximation to the vibrational density of states, $g(\nu,\vec{\sigma},V)$, according to [113]:

$$F_{vib}(\vec{\sigma},T,V) = k_B T \int \ln\left[2\sinh\left(\frac{h\nu}{2k_B T}\right)\right] g(\nu,\vec{\sigma},V)\,d\nu \qquad (2.23)$$

where ν is a vibrational frequency. Within the quasi-harmonic approximation, the coarse-grained free energy $G(\vec{\sigma},T)$ is set equal to the minimum of $F_{vib}(\vec{\sigma},T,V)$ with respect to V (i.e. the pressure is assumed to be zero). The ability to perform this coarse graining procedure, however, rests on the assumption that each arrangement of atoms is mechanically stable and exhibits minimal

anharmonicity with respect to vibrational degrees of freedom. It will emerge that fcc based TiH_{2-z} exhibits important anharmonicity with respect to homogeneous tetragonal strain, indicating that a standard coarse graining scheme may not be sufficient to capture all relevant degrees of freedom in this system. We will argue that additional thermal excitations involving local strain fluctuations are likely to also contribute to the thermodynamic properties of TiH_{2-z}.

In this thesis, the vibrational free energies were calculated with a force-constant spring model. The force constants were extracted from first-principles GGA calculations of the restoring forces due to atomic perturbations within supercells using the FITFC code of the Alloy Theoretic Automated Toolkit.

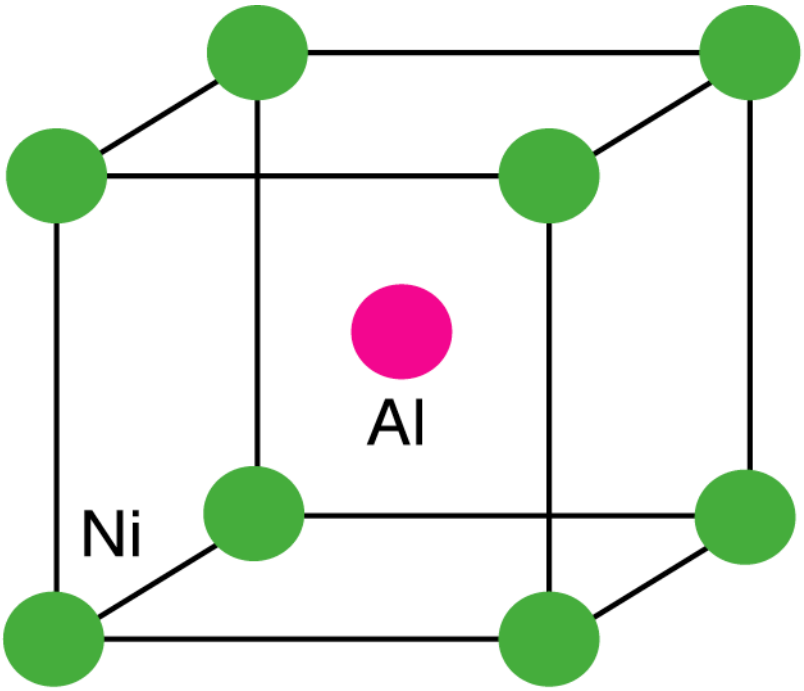

Figure 2-1 Crystal structure of B2-NiAl compound

Chapter 3

First-principles investigation of phase stability in interstitial metal-hydride: The Ti-H system

In this chapter, we will investigate various factors that affect metal-hydride phase stability from first principles. As a particular example, we consider hydride stability in the Ti-H system, exploring the role of configurational degrees of freedom, zero-point vibrational energy as well as coherency strains. We will show that the tetragonal γ-TiH phase is predicted (within GGA) to be unstable relative to hcp Ti (α phase) and the fcc based δ-TiH_2. Due to the light mass of hydrogen atom, zero point vibrational energy significantly affects the formation energies in this system and makes the γ phase even less stable relative to hcp Ti and δ-TiH_2. The effect of stress and strain on the stability of the γ phase is also investigated showing that coherency strains between hydride precipitates and the hcp Ti matrix stabilize γ-TiH relative to α-Ti and δ-TiH_2, explaining why it is observed experimentally. We also find that hydrogen prefers octahedral sites at low hydrogen concentration and tetrahedral sites at high concentration. Both harmonic vibrational as well as electronic origins for the cubic to tetragonal phase transformation of TiH_2 are investigated and we argue that anharmonic vibrational degrees of freedom are likely to play an important role in stabilizing cubic TiH_2.

A simultaneous treatment of configurational degrees of freedom and vibrational excitations is computationally very demanding, as it would require the first-principles calculation

of phonon densities of states of many different hydrogen-vacancy configurations over the interstitial sites of Ti to determine the coarse grained free energies $G(\vec{\sigma},T)$ for each configuration. Furthermore, as will be illustrated, the Ti-H system exhibits strong anharmonicity with respect to homogeneous strain indicating that long wavelength strain fluctuations may contribute to the thermodynamic properties of this system. Such excitations cannot be accounted for with the coarse graining scheme described above [112], which treats vibrational excitations within the quasi-harmonic approximation. We therefore investigate configurational and vibrational degrees of freedom independent of each other to derive qualitative insight about the importance of configurational entropy, zero-point vibrational energy and coherency strain on the stability of γ-TiH relative to hcp Ti and TiH_2.

3.1 Configurational degrees of freedom

3.1.1 Formation energies and relative stability of host structures

An investigation of phase stability in the Ti-H system must start with a consideration of the likely host structures that can accommodate hydrogen insertion. In this thesis, we focused on the hcp and fcc Ti hosts. While bcc Ti is observed at high temperature, it is predicted to be mechanically unstable from first-principles, raising fundamental questions about the true nature of this high-temperature phase [1]. Within the hcp and fcc hosts, hydrogen can reside in either octahedral or tetrahedral sites. For each Ti atom in the hcp and fcc structures, there are two four-coordinated tetrahedral sites and one six-coordinated octahedral site (see Fig. 3-1).

We calculated the energy of a variety of different hydrogen-vacancy configurations over the interstitial sites of both hcp Ti and fcc Ti using density functional theory within the generalized gradient approximation (Perdew-Burke-Ernzerhof parameterization of the exchange

correlation potential) as implemented in the VASP plane-wave pseudopotential code [90,91]. The core-electron interactions were treated with the projector augmented wave (PAW) method [89,92] and a plane-wave basis set cutoff energy of 400eV was used. The *k* point-grids were sampled with the Monkhorst and Pack method [116] and partial occupancy at the Fermi level was treated with the method of Methfessel and Paxton [117]. The ionic positions and the lattice parameters of each structure were fully relaxed. Convergence tests of the energy with respect to *k* point grids indicated that *k*-point sampling errors are less than 5 meV per TiH_{3x} formula unit.

Formation energies of the low energy configurations are illustrated in Fig. 3-2 in which fcc Ti and δ-TiH_2 (all tetrahedral sites filled with hydrogen) are used as reference states and each formation energy, $\Delta E(x)$, for a particular configuration having formula TiH_{3x} is defined as

$$\Delta E(x) = E(x) - \frac{3}{2}x \bullet E_{TiH_2}^{\delta} - \left(1 - \frac{3}{2}x\right) \bullet E_{Ti}^{fcc} \qquad (3\text{-}1)$$

where $E(x)$ is the total energy per crystal site for the same configurations of TiH_{3x} calculated from first-principles (with DFT-GGA using VASP) while $E_{TiH_2}^{\delta}$ and E_{Ti}^{fcc} are the first-principles energies per atom of δ-TiH_2 and fcc Ti crystal.

For pure Ti, we find that hcp Ti is more stable than fcc Ti by 55 meV/atom and more stable than bcc by 109 meV/per atom. This result is consistent with the experimental observation that hcp α-Ti is observed at room temperature. Hydrogen insertion, though, leads to a stabilization of fcc relative to hcp. At the stoichiometric TiH_2 composition the lowest energy configuration is one in which hydrogen fills all tetrahedral sites (a CaF_2 structure). This structure corresponds to the experimentally observed δ-TiH_2. The cubic TiH_2 structure can further lower its energy by 6 meV per Ti through a tetragonal distortion, which corresponds to the experimentally observed low temperature ε-TiH_2 phase. At intermediate concentration, an

ordered phase with composition TiH is energetically favored relative to fcc Ti and δ-TiH_2, however, not stable enough to make it a ground state relative to hcp α-Ti and δ-TiH_2 (i.e. its energy is above the dashed line in Fig. 3-2) or hcp α-Ti and ε-TiH_2 (i.e. its energy is above the solid line in Fig. 3-2). In this low energy TiH phase, the H atoms occupy half the tetrahedral sites as illustrated in Fig. 3-2. This H-ordering is the same as that reported for the γ-TiH phase observed experimentally but believed to be metastable [35]. The particular H-ordering within γ-TiH leads to a face center tetragonal (fct) unit cell with a calculated c/a ratio of 1.1. The experimental *c/a* ratio is 1.093 [35]. A summary of calculated lattice parameters for several phases is presented in Table 3-1. The consistency with experiment is satisfactory [35,37,118].

Several TiH_{3x} structures with compositions close to stoichiometric TiH_2 exhibit peculiar mechanical instabilities and a strong degree of anharmonicity with respect to homogeneous strains. The energy of TiH_2 as a function of the *c/a* ratio, for example, is illustrated in Fig. 3-3(a). The energy curve displays two local minima, one with $c/a>1$ and the other with $c/a<1$. The minimum at $c/a<1$ has the lowest energy and corresponds to the ε phase observed experimentally below room temperature [34]. The difference in energy between cubic TiH_2 and tetragonal TiH_2 is predicted within GGA to be ~6meV per Ti atom. Surprisingly, the cubic form of TiH_2 ($c/a=1$), which appears experimentally above ~300 K [34], is predicted to be mechanically unstable at zero Kelvin. Similar curves were predicted by Wolf and Herzig for TiH_2 and ZrH_2 and by Ackland for ZrH_2 [119]. The calculations of Wolf and Herzig [120], performed with FLAPW using LDA with the Hedin and Lundquist parameterization, however, predicted the tetragonal variant with $c/a>1$ to be more stable than the $c/a<1$ variant. The discrepancy between their results and those predicted here can likely be attributed to a difference in the parameterization of the exchange correlation potential. Indeed, we recalculated the energy

versus *c/a* with a variety of *k*-point meshes ranging from 8x8x8 to 24x24x24 for the non-primitive cubic TiH_2 unit cell to rule out errors due to poor k-point sampling. For all k-point meshes, the c/a <1 tetragonal variant has the lowest energy. We also found that LDA based on the Perdew-Zunger parameterization of the exchange correlation predicts the tetragonal variant with *c/a* <1 to have the lowest energy.

Similar mechanical instabilities with respect to a homogeneous tetragonal distortion were found for other H-vacancy configurations in fcc Ti with compositions close to TiH_2. Figures 3-3(b) and 3-3(c) illustrate the energy for two off-stoichiometric compounds as a function of the *c/a* ratio. The difference between the mechanically unstable cubic form and a stable tetragonal variant as hydrogen vacancies are added to TiH_2 was always found to be less than 3 meV per Ti. The mechanical instabilities of hydrogen rich cubic TiH_{2-z} configurations complicate a rigorous description of the finite temperature excitations that determine the thermodynamic properties of this system. The strong anharmonicity with respect to homogeneous strain indicates that long wavelength strain fluctuations are easily excited, thereby contributing to finite temperature free energies that determine phase stability. Such excitations were not explicitly investigated in this thesis.

3.1.2 Cluster expansion and statistical mechanics for the fcc and hcp hosts

The formation energies in Fig. 3-2 show that the hcp Ti host rapidly becomes unstable relative to the fcc Ti host as hydrogen is inserted. This indicates that the hydrogen solubility within α-Ti (hcp) will be dilute and that the relevant thermodynamic properties of this phase can be treated with an ideal solution model in which interactions between different hydrogen atoms are neglected. For fcc Ti, however, non-dilute hydrogen interactions are important and a cluster

expansion is necessary to parameterize the formation energies for the different hydrogen-vacancy configurations in this host.

A cluster expansion for the fcc host structure was constructed by fitting Eq. 2.10 to formation energies of 65 different H-vacancy configurations within the fcc host with the largest supercell containing four TiH_{3x}. By minimizing the MCCV using a genetic algorithm, an optimal set of clusters was selected from a total of 79 candidates. The set includes 1 empty cluster, 2 points (for the tetrahedral and octahedral sites), 6 pairs, 4 triplets and 5 quadruplets and the values of their ECI are illustrated in Fig. 3-4. The root-mean-square (rms) error with respect to the structures used in the fit is 8 meV per TiH_{3x} formula unit and the Leave-One-Out CV (LOO-CV) is 16 meV per TiH_{3x} formula unit. The cluster expansion correctly predicts γ–TiH and δ-TiH_2 to be ground states when considering only hydrogen-vacancy configurations over the interstitial sites of fcc Ti.

It should be noted that the use of a cluster expansion for the cubic fcc based TiH_{3x} is not strictly rigorous, as this phase is mechanically unstable with respect to a tetragonal distortion for hydrogen compositions close TiH_2 (see Fig. 3-3 and section 3.1.1). However, as noted above, the difference in energy between the cubic phase and the mechanically stable tetragonal variants in TiH_{2-z} was found to be less than 3 meV per Ti, except for TiH_2, for which the difference is 6 meV per Ti. As these differences in energy are very small and are of the order of typical numerical errors due to *k*-point sampling, we believe that the cluster expansion of Fig. 3-4 should provide a sufficiently accurate description of the configurational energy of cubic TiH_{2-z} observed experimentally above 300 K [34].

In the parameterization of the cluster expansion for fcc TiH_{3x}, we used fully relaxed energies for each of the 65 H-vacancy configurations. The relaxed energies were determined

with an automated relaxation procedure (i.e. conjugate gradient method within VASP). We point out, though, that this approach is not always guaranteed to find the lowest energy (mechanically stable) distortion due to symmetry constraints of the prerelaxed structure. In this work, for example, we relaxed each configuration starting with a cubic Ti-fcc host. If the H-vacancy arrangement preserves this symmetry, the relaxed structure will also be cubic and will not spontaneously relax to a mechanically stable tetragonal variant. The H-vacancy configurations that do not preserve cubic symmetry will spontaneously distort, however, the relaxed distortion may not correspond to the lowest energy tetragonal variant for that configuration. An analysis of the vibrational degrees of freedom (section 3.2) of a subset of the 65 relaxed H-vacancy configurations used in the fit of the cluster expansion showed that several of these configurations are mechanically unstable with respect to a tetragonal distortion. The use of relaxed input energies that do not always correspond to the lowest energy distortion can contaminate the fit of a cluster expansion, leading to a reduction in its ability to predict the energies of configurations not included in the fit. However, since the difference between stable tetragonal distortions and cubic TiH_{2-z} ranges between 3-6 meV per Ti, we expect only a marginal increase in accuracy if a more consistent set of input energies were used in the fit of the cluster expansion (obtained e.g. by manual relaxation of each of the 65 configurations to find the lowest energy distortion).

The cluster expansion of the H-vacancy configurational energy in fcc Ti was implemented in Monte Carlo simulations in the grand canonical ensemble. A Monte Carlo cell containing 512 unit cells (1536 interstitial sites as there are two tetrahedral sites and one octahedral site per unit cell) was used. At each temperature and chemical potential, 1000 Monte Carlo passes per site were performed after which averaging occurred over 2000 Monte Carlo passes. The relative stability between fcc and hcp hosts as a function of hydrogen concentration

can be determined by a comparison of their free energies. For the fcc host, the free energies were calculated by integrating the chemical potential obtained from Monte Carlo simulations, starting from reference states where the free energy is known (e.g., at x=0 in TiH_{3x} for which the configurational entropy is zero [4] or in ordered phases at low temperature where the free energy can be calculated with a low-temperature expansion [10].)

Due to the low hydrogen solubility in hcp Ti, we can accurately describe the free energy of α-TiH_{3x} with an ideal solution model (in which interactions among hydrogen atoms are neglected). The details can be found in Appendix B of this thesis. The change in energy upon adding an isolated hydrogen to either a tetrahedral or octahedral site in hcp Ti was calculated in a 36 atom supercell (comparisons with similar calculations in a 96 atom supercell showed that the 36 atom supercell is sufficiently large to approximate the dilute limit). The ideal solution free energy for interstitial occupancy in hcp Ti has one internal degree of freedom at fixed hydrogen concentration with respect to octahedral versus tetrahedral site occupancy. The relative hydrogen occupancy between octahedral and tetrahedral sites as a function of *T* and hydrogen concentration was determined by minimizing the ideal solution free energy with respect to this internal degree of freedom.

3.1.3 Phase diagram

Two calculated phase diagrams are illustrated in Fig. 3-5. Fig. 3-5(a) shows a metastable phase diagram of TiH_{3x} over the fcc host only. Figure 3-5(b) shows the phase diagram of TiH_{3x} calculated by comparing free energies over both the fcc and hcp hosts, with the vertical dash line representing the stoicheometric TiH_2. Considering only the fcc host structure, Fig. 3-5(a) shows that two hydrides are stable: the γ hydride (TiH) and the δ hydride (TiH_2). The γ hydride is

predicted to be stable only at low temperature, decomposing through a peritectoid reaction at around 450K. This γ hydride corresponds to the face centered tetragonal TiH phase observed experimentally [35]. The δ-TiH_2 hydride, in which H occupies the tetrahedral interstitial sites of the fcc Ti host, can tolerate a large degree of off-stoichiometry, accommodated by H-vacancies.

When considering relative stability over both the fcc and hcp host structures (below ~700K), as illustrated in Fig. 3-5(b), only the δ-TiH_2 hydride remains stable. A large two-phase coexistence region exists between δ-TiH_2 and α hcp Ti, the latter characterized by a very dilute H solubility limit. Not included in the calculated phase diagrams is the cubic to tetragonal transition that occurs upon cooling TiH_2 to low temperatures. This transition will be discussed in section 3.3.

Experiments by Numakura and Koiwa [35] demonstrated the existence of γ-TiH precipitates within the α phase matrix in a Ti-3 at. % H specimen. The calculated phase diagram, however, predicts that γ-TiH is metastable with respect to α-Ti and δ-TiH_2. Figure 3-2 shows that the formation energy of γ-TiH lies above the common tangent to the formation energies of α hcp Ti and δ-TiH_2. The Monte Carlo simulations show that the degree with which γ-TiH is unstable relative to α hcp Ti and δ TiH_2 increases substantially with temperature. As the temperature is raised, the free energy of δ-TiH_2 decreases more rapidly than that of γ-TiH as a result of the additional configurational entropy arising from vacancy disorder in off-stoichiometric δ-TiH_{2-z}. This is clearly illustrated by the calculated free energy curves of the α, δ, and γ phases as a function of H concentration at various temperatures (Fig. 3-6). While the free energy of γ at low temperature lies below the common tangent to *fcc* Ti and δ-TiH_2, it is well above the common tangent to the free energies of α hcp Ti and δ-TiH_2. Above 450K (the

peritectoid temperature in Fig. 3-5(a)), the γ-TiH phase disappears altogether. These results show that when considering only configurational degrees of freedom, the γ-TiH hydride is predicted (within the first-principles GGA approach) to be unstable at finite temperature. Other factors, including vibrational degrees of freedom or coherency strain may alter the stability of γ-TiH relative to α hcp Ti and δ-TiH_2 and thus show that the observations of γ-TiH by Numakura and Koiwa [35] is thermodynamically driven and not due to kinetic factors. This will be explored in subsequent sections.

3.1.4 Site occupancy

Both the fcc and hcp hosts offer tetrahedral and octahedral interstitial sites for H-occupancy. The first-principles GGA calculations of formation energies of the different H-vacancy arrangements over the interstitial sites of fcc and hcp show that the preference for tetrahedral and octahedral sites depends on the overall hydrogen concentration. At low H concentration, H prefers octahedral interstitial sites in both hcp Ti and fcc Ti, while at high concentration, H prefers the tetrahedral interstitial sites in the fcc host. This result persists at finite temperature as predicted both by the dilute solution model for the hcp host and the Monte Carlo simulations for the fcc host. For the hcp host with dilute H, the octahedral site is more stable than the tetrahedral site by 76 meV. For the fcc Ti host, the site occupancy, which is defined as the number of H in a particular type of interstitial site divided by the total number of that type of interstitial site, can be extracted from the Monte Carlo simulations. Figure 3-7 illustrates the site occupancy as a function of H concentration at 300K and 600K for the fcc Ti host. As is evident from Fig. 3-7, H prefers the octahedral sites at low concentration, while it prefers the tetrahedral sites at high H concentration, although at 600K some octahedral

occupancy also exists in the H-rich δ-TiH_2 phase at hydrogen compositions near the two-phase coexistence boundary.

3.2 Vibrational degrees of freedom

The analysis of phase stability in the Ti-H system has so far only taken account of configurational degrees of freedom. However, due to the low mass of hydrogen, vibrational degrees of freedom can be important, especially zero-point vibrational energies. To investigate this, we calculated the phonon densities of states of 30 different H-vacancy configurations within the fcc Ti host along with the phonon density of states for hcp Ti. These were calculated with a force constant spring model [113]. The force constants were extracted from first-principles GGA calculations (with the VASP code) of the restoring forces due to atomic perturbations within supercells using the *fitfc* code of the Alloy-Theoretic Automated Toolkit (ATAT) [113,121]. For each fcc based configuration, we used a supercell with maximal length between periodic images of 9 Å and extracted spring constants up to an inter-atomic distance of 4.5 Å. Convergence tests for several hydrogen-vacancy arrangements indicated that these supercell sizes and spring cutoff lengths lead to a numerical error in the zero-point vibrational energies of about 1 meV per formula unit of TiH_{3x}.

Among the 30 configurations for which phonon densities of states were calculated, 8 exhibited unstable phonon modes. The formation energies with and without zero-point vibrational energy of the remaining 22 stable H-vacancy configurations are illustrated in Fig. 3-8. The formation energies are relative to the fcc Ti and δ-TiH_2 reference states (also with and without zero-point vibrational energies respectively). Figure 3-8 clearly shows that zero-point vibrational energy can have a significant effect on the formation energies of some configurations

in a hydrogen containing system. In fact, inclusion of zero-point vibrational energy raises the formation energy of γ-TiH by 19 meV, thus making this phase even less stable relative to α-Ti and δ-TiH_2 already at zero Kelvin.

The effect of zero-point vibrational energy on formation energies also differs qualitatively depending on whether hydrogen atoms occupy tetrahedral sites or octahedral sites. Among the 22 configurations of Fig. 3-8, 15 configurations have exclusive tetrahedral occupancy by hydrogen, 3 configurations with a hydrogen concentration *x* less than 1/6 have octahedral-hydrogen occupancy only while the remaining 3 configurations, which have relatively high formation energies, have both tetrahedral- and octahedral-hydrogen (the last configuration is pure fcc Ti without H atoms). We found that zero-point vibrational energy raises the formation energies of most low energy configurations containing tetrahedral sites while it lowers the formation energy for configurations with octahedral hydrogen. This is presumably due to the larger interatomic distance between H and Ti in the octahedral sites as compared to tetrahedral sites. Larger interatomic distances tend to lead to softer bonds (smaller force constants) and therefore vibrational densities of states corresponding to lower frequencies [113].

Similar trends were found in hcp Ti. Inclusion of zero point vibrational energy raised the difference in energy between tetrahedral versus octahedral occupancy by hydrogen (in the dilute limit) from 76 meV to 146 meV, further destabilizing the tetrahedral site in this dilute regime. These energy differences were calculated in a 36-atom hcp Ti supercell containing one hydrogen atom. The phonon densities of states of an isolated hydrogen atom in hcp Ti were calculated with a force-constant spring model, fit to first-principles GGA calculations of atomic perturbations in the 36-atom unit cell.

We point out that a harmonic spring model for a particular crystal can fail to predict

mechanical instabilities if the force constants are too short-ranged. Extending force constants to larger distances than used in this work, or using a linear response method to calculate the phonon density of states, may indicate that even more than 8 of the 30 H-vacancy configurations considered here are mechanically unstable. In fact, the short-ranged spring model failed to predict the mechanical instability of cubic TiH_2 with respect to a homogeneous tetragonal distortion (see Fig. 3-3(a)).

3.3 The cubic to tetragonal phase transformation of TiH_2

We have so far focused on hydrides in the Ti-H system that form as the result of hydrogen ordering over the interstitial sites of fcc Ti. However, in addition to the γ-TiH and δ-TiH_2 hydrides, a third hydride can form, denoted ε-TiH_2, as a result of a structural cubic to tetragonal transformation from cubic δ–TiH_2 around 300 K [34]. We can distinguish between structural transformations that involve an internal shuffle, in which atoms within a unit cell rearrange at a transition temperature and thereby change the symmetry of the crystal, and structural transformations involving a homogeneous strain of the unit cell. The cubic δ–TiH_2 to tetragonal ε-TiH_2 phase transformation falls into the second category. The first category has been studied extensively in the context of ferro-electric phase transformations using first-principles effective Hamiltonians [9,122-124]. The second category of structural phase transformations is less well understood from a statistical mechanical point of view.

While the cubic form of TiH_2 is observed experimentally above ~300K [34], calculations within density functional theory predict that this phase is mechanically unstable with respect to a tetragonal distortion at zero Kelvin [see Fig. 3-3(a) and ref 120]. Conventional intuition about structural phase transformations is typically based on a Landau interpretation in which

temperature dependent free energies are assumed to exist as a function of some order parameter, which in the case of TiH_2 would be the *c/a* ratio. As the temperature increases, the shape of the free energy should change in a way that renders the high temperature phase both mechanically stable and as having the lowest free energy. For TiH_2, this picture implies that vibrational and electronic excitations should make the cubic form of TiH_2 mechanically stable at a finite temperature, as reflected by a free energy curve exhibiting a local minimum around c/a=1. Here we explore the extent with which electronic and harmonic-vibrational excitations at finite temperature affect the free energy of TiH_2 as a function of the *c/a* ratio.

The cubic to tetragonal phase transformation of TiH_2 has been suggested to originate from a Jahn-Teller instability [125,126]. Experiment as well as density functional theory calculations [120,125,126] have demonstrated that the Fermi level of cubic TiH_2 (and ZrH_2 [120,127,128]) coincides with a peak in the electronic density of states. A tetragonal distortion of TiH_2 splits this peak [126], resulting in a minimum in the density of states at the Fermi level and a lowering of the total energy of the crystal. At elevated temperature, however, thermally excited electrons will start occupying the split off empty states above the Fermi-level of the tetragonal phase, thereby undoing the energy gain of the Jahn-Teller distortion. We can therefore expect a critical temperature above which the cubic form of TiH_2 should become mechanically stable and have a free energy that is lower than tetragonal TiH_2.

In order to qualitatively investigate the role of electronic excitations on the cubic to tetragonal phase transformation, we calculated the free energy of TiH_2 as a function of the *c/a* ratio due to electronic excitations by varying the degree of thermal broadening of the electron distribution around the Fermi level, using the Fermi smearing feature in VASP calculations with a smearing factor given by $\sigma = k_B T$. Figure 3-9 illustrates the calculated free energies at various

temperatures T. In these calculations, we used a sufficiently dense k-point grid (24x24x24 mesh for the non-primitive fcc form of TiH_2) to ensure k-point convergence for each value of σ. Figure 3-9 clearly shows that the difference in free energy between tetragonal and cubic TiH_2 decreases with increased broadening (due to increased temperature) of the electron distribution around the Fermi level. Furthermore, the *c/a* ratio corresponding to the minimum free energy gradually approaches 1 as the temperature increases. Nevertheless, the cubic phase remains mechanically unstable with respect to tetragonal distortion up to temperatures in excess of 800K, which is well above the experimentally measured cubic to tetragonal transition temperature of 300K. This result suggests that electronic excitations alone cannot account for the experimentally observed cubic to tetragonal phase transformation of TiH_2 at 300K [34]. Other factors related to vibrational degrees of freedom must therefore also play an important role in this transformation.

The fact that a short-ranged spring model fails to predict mechanical instabilities due to homogeneous strains of cubic TiH_2, as described in Section 3.2, provides us with an opportunity to calculate a constrained free energy as a function of the *c/a* ratio due to harmonic vibrational degrees of freedom, even for the portions that are mechanically unstable with respect to a homogeneous tetragonal distortion. This is illustrated in Fig. 3-10 where Eq. (2-45) is evaluated as a function of the *c/a* ratio using phonon-dispersion curves calculated within the harmonic approximation with force constants derived from perturbations in supercells having a distance of 11.5 Å between periodic images and spring constants extending to 5.7Å. Figure 3-10 shows that the mechanical instability of cubic TiH_2 with respect to a homogeneous (acoustic) strain persists to temperatures above the experimental cubic to tetragonal transition temperature of 300 K. Although the free energies of Fig. 3-10 are calculated with a first-principles parameterized spring model, they should be viewed as phenomenological free energy curves not unlike Landau free

energies expressed as a function of a strain order parameter. Presumably, the free energy curves of Fig. 3-10, while based on a harmonic spring model that fails to capture the instability of long-wavelength tetragonal distortions of the crystal, accurately account for optical and short wavelength phonon excitations, which are more easily described with short-range spring constants.

The calculated free energies of Figs. 3-9 and 3-10 suggest that a conventional Landau interpretation of the cubic to tetragonal phase transformation, involving free energies that are assumed to have local minima for both the tetragonal and cubic phases as a function of *c/a*, does not apply to TiH_2. Our results indicate that neither electronic excitations nor short-wavelength harmonic vibrations alone can explain the existence of cubic TiH_2 above 300 K, implying that anharmonic vibrational degrees of freedom must also play an important role in stabilizing the cubic phase at high temperature. A more accurate treatment of the relevant finite temperature excitations that stabilize cubic TiH_2 at finite temperature will require an explicit description of the anharmonic vibrational degrees of freedom with for example Monte Carlo simulations applied to an anharmonic strain Hamiltonian that describes the large degree of anharmonicity with respect to long-wave-length tetragonal distortions.

As was noted in section 3.1.1, the mechanical instability of cubic TiH_2 persists as the hydrogen concentration is reduced (see Fig. 3-3(b) and Fig. 3-3(c)), although the difference in energy between the stable tetragonal variant and the cubic form of TiH_{2-z} reduces to around 3 meV per TiH_{2-z} formula unit. A rigorous characterization of the thermodynamic properties of the cubic form of TiH_{2-z}, therefore, requires not only the inclusion of configurational degrees of freedom, but also anharmonic vibrational degrees of freedom. This could be achieved with an effective Hamiltonian that couples both configurational degrees of freedom with anharmonic

strain degrees of freedom. Due to the extra degrees of freedom that are readily excited at low temperature, in addition to configurational degrees of freedom, we can expect an explicit inclusion of strain fluctuations to lead to a further stabilization of the δ-TiH_{2-z} phase and an increase in the off-stoichiometry that can be tolerated by δ-TiH_{2-z}. An explicit inclusion of the anharmonic strain fluctuations, while more rigorous, is unlikely to qualitatively alter the results of section 3.1 with respect the off-stoichiometry predicted for δ-TiH_2 or the stability of γ-TiH relative to α-Ti and δ-TiH_2. Nevertheless, such a treatment would enable the prediction of the composition dependence of the δ to ε cubic to tetragonal transformation temperature and would shed new light on the thermodynamic properties of high temperature phases that are predicted to be mechanically unstable at zero Kelvin.

3.4 The role of stress and coherency strains

Crack growth in Ti within a hydrogen rich environment is often accompanied by hydride formation ahead of the crack tip under slow loading conditions [15]. This experimental observation suggests that the Ti-hydrides become thermodynamically more favored under a state of tensile stress. Even in the absence of external loads, internal stresses that could alter the relative stability of the various phases competing for stability can arise during solid-state phase transformations due to coherency strains and volumetric changes. In fact, Numakura and Koiwa [35] observed that thin plate-like γ-TiH precipitates form coherently within the α-Ti matrix during the early stages of hydride formation. Their TEM analysis elucidated the crystallographic relationship between γ-TiH and the α-Ti matrix, showing that the coherent interface consists of a prismatic $\{0\bar{1}10\}$ plane of the hcp Ti matrix on one side and the $\{1\bar{1}0\}$ plane of γ-TiH precipitate on the other. Figure 3-11(a) schematically illustrates this coherent interface between

α-Ti and γ-TiH, reproduced from Numakura and Koiwa [35].

When a thin, extended γ-TiH plate forms coherently within the α-Ti matrix, its lattice parameters parallel to the coherent interface will be constrained by those of the matrix phase, thereby leading to a state of internal stress within the precipitate. To ensure coherency between α-Ti and γ-TiH along the interface illustrated in Fig. 3-11(a), d_{220} must equal $d_{2\bar{1}\bar{1}0}$ and d_{002} must equal d_{0002}, where d_{hkl} and d_{hklm} are interplanar spacings of atomic planes in the precipitate and matrix, respectively. The lattice parameter of γ-TiH perpendicular to the coherent interface, i.e. the $[1\,\bar{1}\,0]$ direction, can potentially relax. The degree to which this lattice parameter relaxes depends on the overall geometry of the specimen as well as the elastic stiffness of the matrix phase. Due to a volumetric increase upon hydride formation, it is likely that the precipitate will experience some degree of compressive stress perpendicular to the interface.

A phase diagram can be constructed displaying the relative stability between α-Ti, γ-TiH and δ-TiH_2 as a function of stress. While equilibrium at constant temperature, pressure and concentration is determined by a minimum of the Gibbs free energy, a different characteristic thermodynamic potential must be minimized to determine phase equilibrium if the system is subjected to an anisotropic state of stress resulting from an external load or from internal coherency strains. In its most general form, a particular state of stress can be represented with a stress tensor. For simplicity and for the purpose of revealing general trends, we consider only uniaxial stress states, represented by the scalar σ. Other external thermodynamic boundary conditions that are often imposed on a stressed metal susceptible to hydride formation is a constant temperature, T, and a constant hydrogen chemical potential, μ_H, which can be controlled experimentally by fixing the hydrogen partial pressure of the environment. At fixed T, μ_H and σ,

the characteristic thermodynamic potential to be minimized to determine phase equilibrium takes the form

$$\Phi = E - TS - \mu_H N_H - V_o \sigma \varepsilon \tag{3-2}$$

where E is the internal energy, S the entropy, N_H the number of hydrogen atoms, ε the strain and V_o a reference volume of the solid with respect to which the strain is measured (here we set it to the initial cell volume). When the above quantities are normalized per Ti atom, then N_H becomes 0 for pure Ti, 1 for TiH and 2 for TiH_2. The thermodynamically stable phase at a particular T, μ_H and σ will have the lowest value for Φ among all the phases competing for stability.

For a fixed hydrogen chemical potential μ_H, we can obtain from Eq. (3-2) (at 0 Kelvin) a free energy curve of Φ as a function of stress level σ, where the stress level as well as the stress-strain curve (e.g. Fig. 3-12 (b) is for hcp-Ti) can be obtained from the derivative of first-principle energy per unit cross section area with respect to the excess elongation (difference between the final length and initial length) (e.g. Fig. 3-12 (a) is for hcp-Ti). Hence, under a fixed hydrogen chemical potential μ_H, we can calculate such free energy curves for α-Ti, γ-TiH and δ-TiH_2 respectively, put these three Φ-σ curves in a single plot (e.g. Fig. 3-12(c) shows free energy curves as a function of stress for μ_H = -5meV without coherency strains) and determine the stress region that favors a specific phase, that is find the stress region where a specific phase has the lowest free energy Φ. In this way we can determine the phase boundary for a fixed hydrogen chemical potential μ_H and furthermore obtain the phase boundary for the whole hydrogen chemical potential region we are interested in.

Figure 3-13 illustrates two such phase diagrams showing relative stability as a function of μ_H and a uniaxial stress σ calculated by minimizing the grand force potential Φ. These phase diagrams were calculated at zero Kelvin, where the entropy is zero and only stoichiometric

compounds exist. Hence the internal energy E appearing in Eq. (3-2) is then simply equal to the first-principles energy (GGA) of either α-Ti, γ-TiH or δ-TiH_2 as a function of the stress σ. In Eq. (3-2), the strain ε is also a function of the stress σ and this dependence is particular to each phase. Practically determining the grand force potential Φ at zero Kelvin can proceed by calculating E versus the strain ε and then extracting the stress σ by taking the derivative of E with respect to ε and dividing by V_o.

The phase diagrams in Fig. 3-13 correspond to two particular states of lateral strain perpendicular to the axis of tension. The axis of tension is along the $[0\bar{1}10]$ direction of the hcp crystal and the $[1\bar{1}0]$ direction of the Ti fcc sublattice of γ-TiH or δ-TiH_2 (Fig. 3-11(b)). If hydrides form coherently within the α-Ti matrix according to the crystallographic orientations reported by Numakura and Kaiwa [35], the tension along the $[0\bar{1}10]$ axis of hcp Ti would coincide with tension along the $[1\bar{1}0]$ direction of the fcc sublattice of γ and δ-hydrides and would be perpendicular to the coherent interface. The phase diagram of Fig. 3-13(a) was calculated for crystals in the absence of coherency strains. The phase diagram of Fig. 3-13(b) was calculated by fixing the hydride lattice parameters perpendicular to the axis of tension to coincide with those of hcp Ti in the $\{0\bar{1}10\}$ plane. Figure 3-13(b) is therefore a phase diagram describing coherent hydride phase stability. The phase diagrams neglect zero-point energies and therefore only provide general trends as to how hydride phase stability evolves with increasing stress.

Figure 3-13(a) shows that at low hydrogen chemical potential α-Ti is stable, while at high chemical potential δ-TiH_2 is stable. The reference state of the hydrogen chemical potential is arbitrarily set to the value corresponding to the transition between α-Ti and δ-TiH_2 at zero stress. As already mentioned in section 3.1.3, bulk γ-TiH is not stable at zero pressure and therefore

does not appear in the phase diagram of Fig. 3-13(a) at σ=0. As stress is imposed, however, γ-TiH becomes stable within a limited range of hydrogen chemical potential and stress. The phase diagram of Fig. 3-13(a) also illustrates that stress along the $[0\bar{1}10]$ direction of α-Ti and the $[1\bar{1}0]$ of the δ-TiH_2 favors hydride formation as manifested by the negative slope of the phase boundary between α-Ti and δ-TiH_2: As the tensile stress, σ, is increased, the transition from α-Ti to δ-TiH_2 occurs at a lower hydrogen chemical potential. This result is consistent with experimental observations of hydride formation ahead of a crack tip [15].

The stability of the γ-TiH phase relative to α-Ti and δ-TiH_2 is significantly enhanced when a strain perpendicular to the axis of tension is imposed on the hydrides to enable the formation of coherent interfaces with the α-Ti matrix along the $(0\bar{1}10)$ habit plane, as illustrated in Fig. 3-11(b). When coherency strains are imposed, γ-TiH even becomes stable for compressive stresses σ within a limited chemical potential range. For a coherent γ-TiH hydride, the chemical potential interval, where γ-TiH is stable, increases with increasing tensile stress perpendicular to the $(0\bar{1}10)$ habit plane.

3.5 Summary

In this chapter we investigated the thermodynamic properties of the Ti-H system from first-principle and it has revealed the importance of configurational and vibrational degrees of freedom in determining hydride phase stability. Configurational excitations are important in δ-TiH_{2-x} as this phase can tolerate large vacancy concentrations, while they do not contribute significantly to the free energy of the γ-TiH phase, which remains a stoichiometric compound at finite temperature. The inclusion of zero-point vibrational energy penalizes tetrahedral site occupancy more than octahedral site occupancy and increases the degree with which γ-TiH is

unstable relative to α-Ti and δ-TiH_{2-z}. This is presumably due to the larger interatomic distance between H and Ti in the octahedral sites as compared to tetrahedral sites. Larger interatomic distances tend to lead to softer bonds (smaller force constants) and therefore vibrational densities of states corresponding to lower frequencies.[38] This favoring of octahedral sites over tetrahedral sites by vibrational degrees of freedom is likely a general trend in all metallic hydrides. An analysis of relative stability under anisotropic stress states shows that hydrides of the Ti-H system are thermodynamically favored under tensile stress. Furthermore, when the hydrides are subjected to coherency strains, γ-TiH is predicted to be stable at zero stress as well as under compressive stresses. The predicted mechanical instability of cubic δ-TiH_2 with respect to a homogeneous tetragonal distortion to ε-TiH_2 raises fundamental questions about the relevant excitations that stabilize cubic TiH_2 above 300 K and suggests the importance of anharmonic strain fluctuations in determining the thermodynamic properties of this phase.

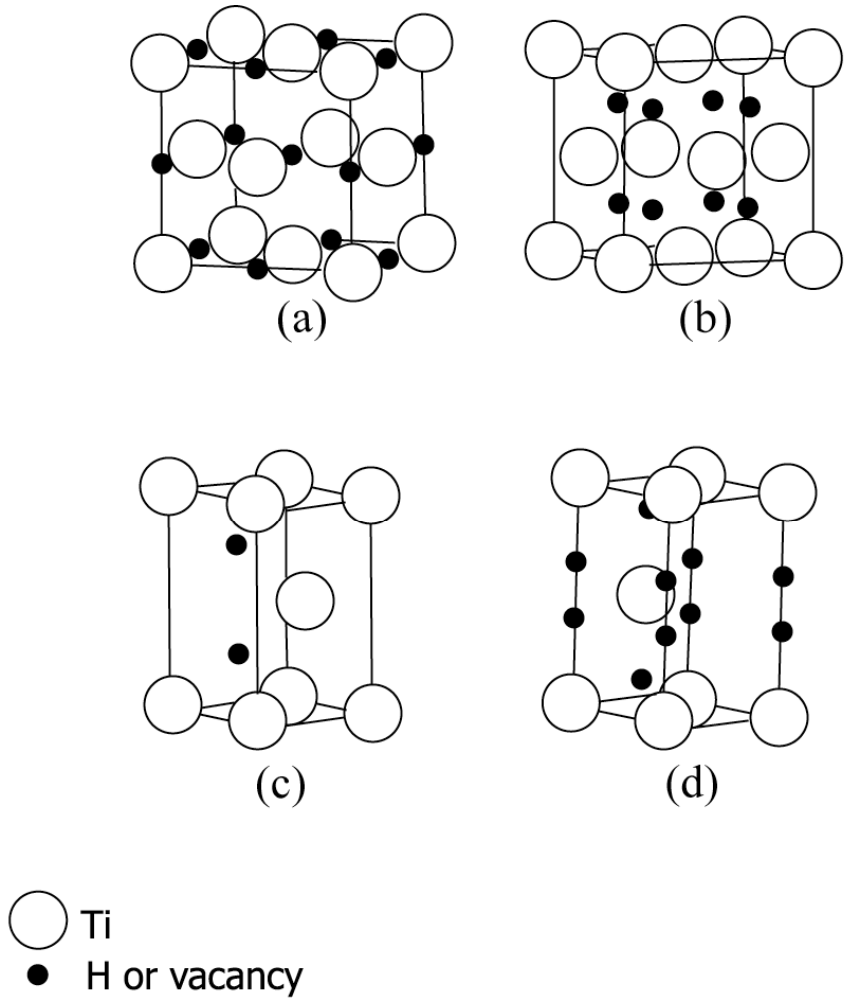

Figure 3-1 Interstitial sites in Ti host: (a) octahedral sites in fcc Ti host, (b) tetrahedral sites in fcc Ti host, (c) octahedral sites in hcp Ti host, and (d) tetrahedral sites in hcp Ti host.

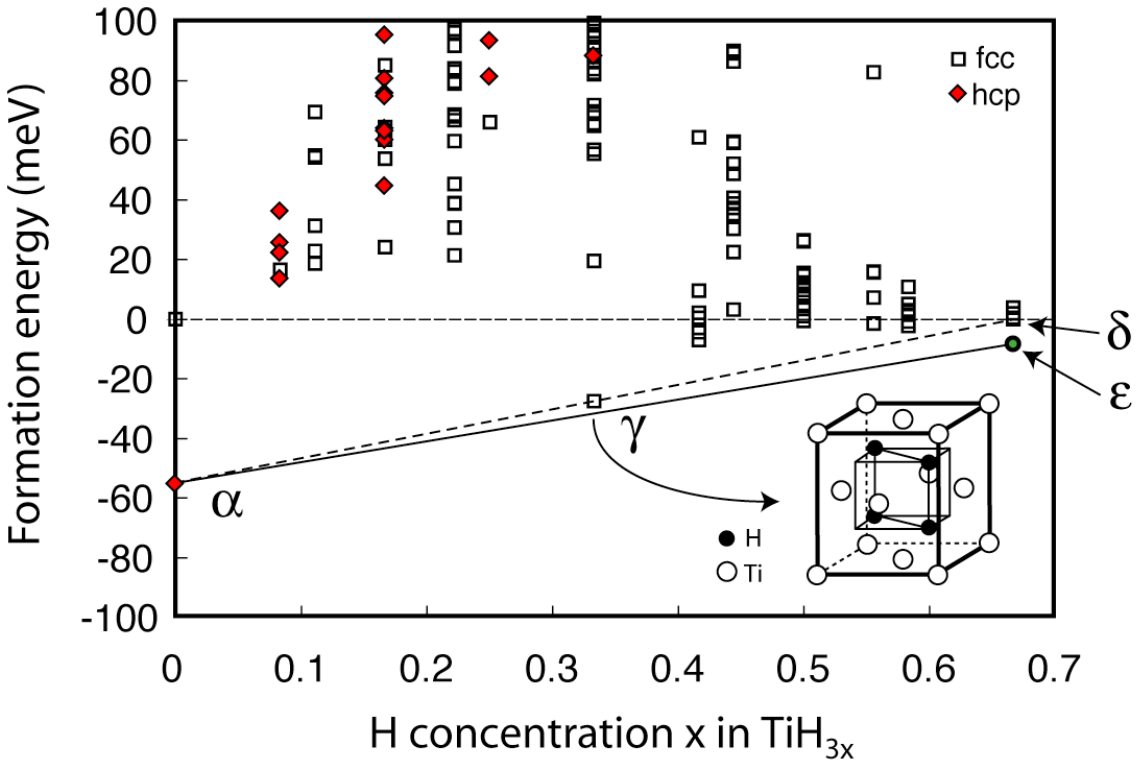

Figure 3-2 Calculated formation energies of TiH_{3x} for fcc and hcp based hydrogen-vacancy configurations with respect to fcc Ti and δ-TiH_2.

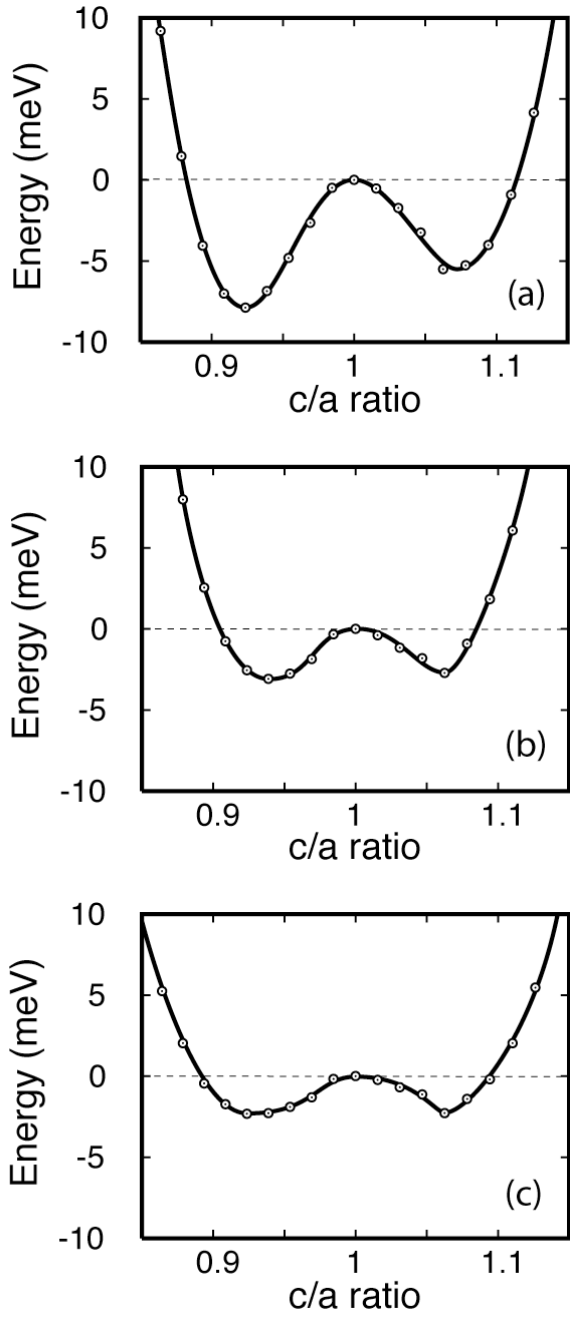

Figure 3-3 Calculated variation of the energy of TiH_{2-z} with c/a ratio (at constant volume) for (a) TiH_2, (b) $TiH_{1.75}$, and (c) $TiH_{1.5}$. A c/a = 1 corresponds to the cubic phase.

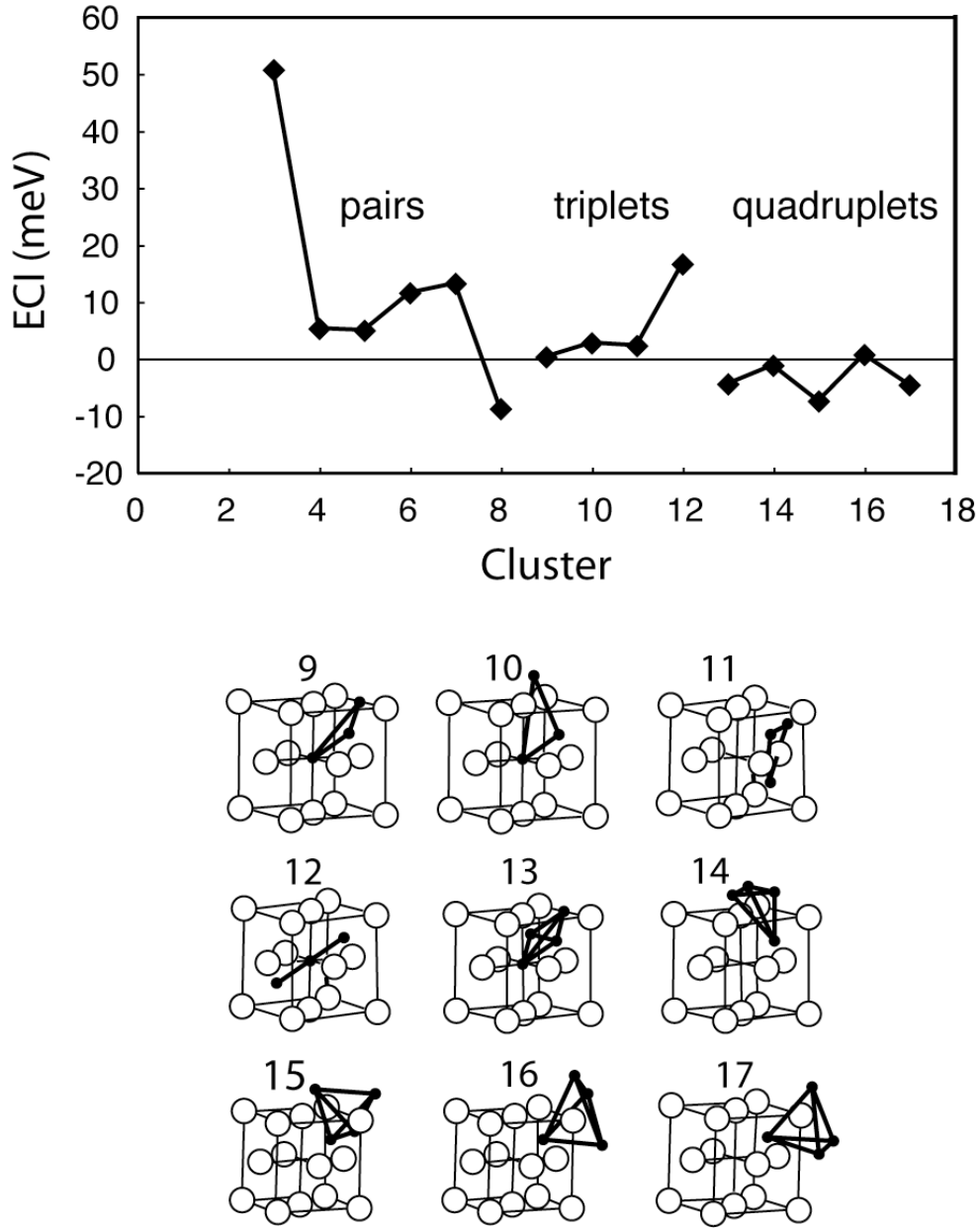

Figure 3-4 Effective cluster interactions for the cluster expansion of the hydrogen-vacancy configurational energies over the interstitial sites of fcc Ti. The clusters include an empty and two point clusters (not shown), six pairs, four triplets, and five quadruplets.

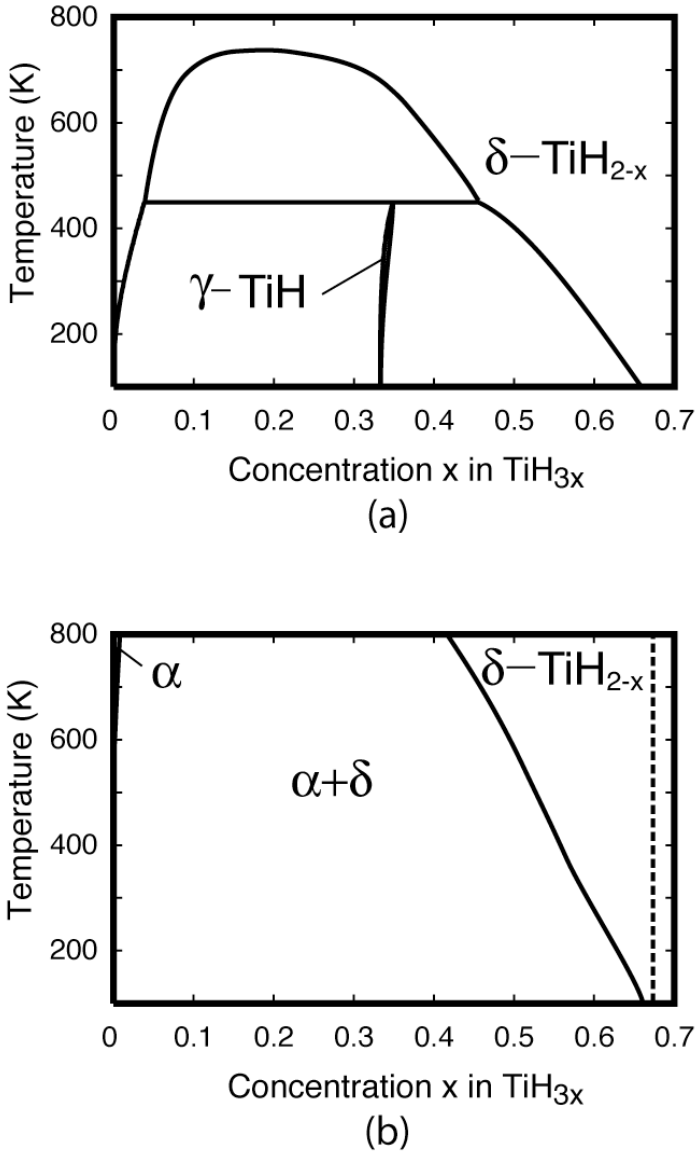

Figure 3-5 Calculated phase diagram of TiH_{3x}: (a) considering relative stability over the fcc-Ti host only and (b) considering relative stability over both the hcp and fcc hosts.

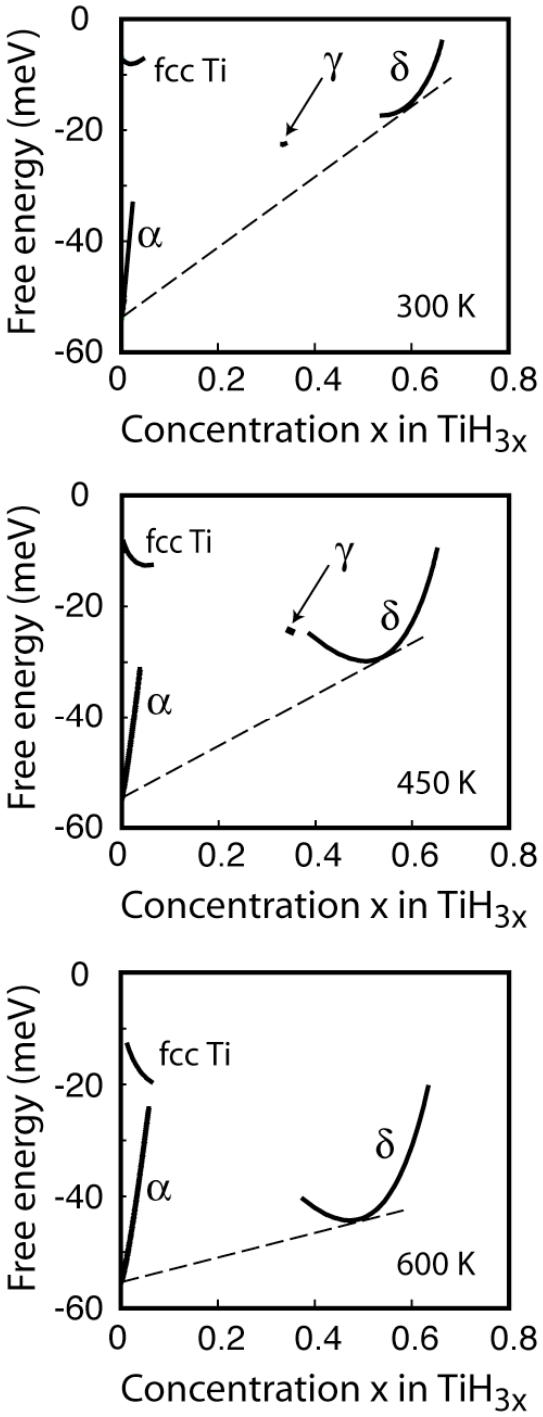

Figure 3-6 Calculated free energy of fcc Ti, α-Ti (hcp), γ-TiH, and δ-TiH_2 at (a) 300K, (b) 450K, and (c) 600K.

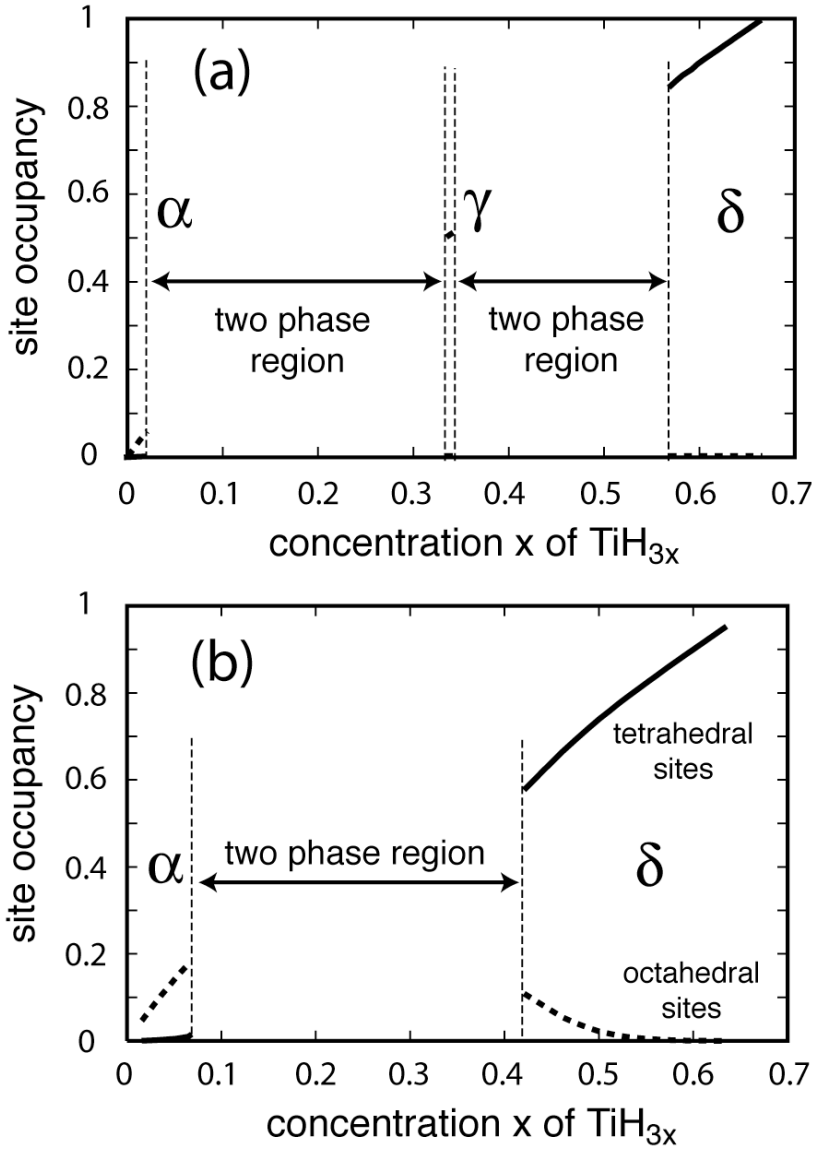

Figure 3-7 Calculated hydrogen concentrations within tetrahedral (solid line) and octahedral (dashed line) sites of the fcc-Ti host at (a) 300K and (b) 600K.

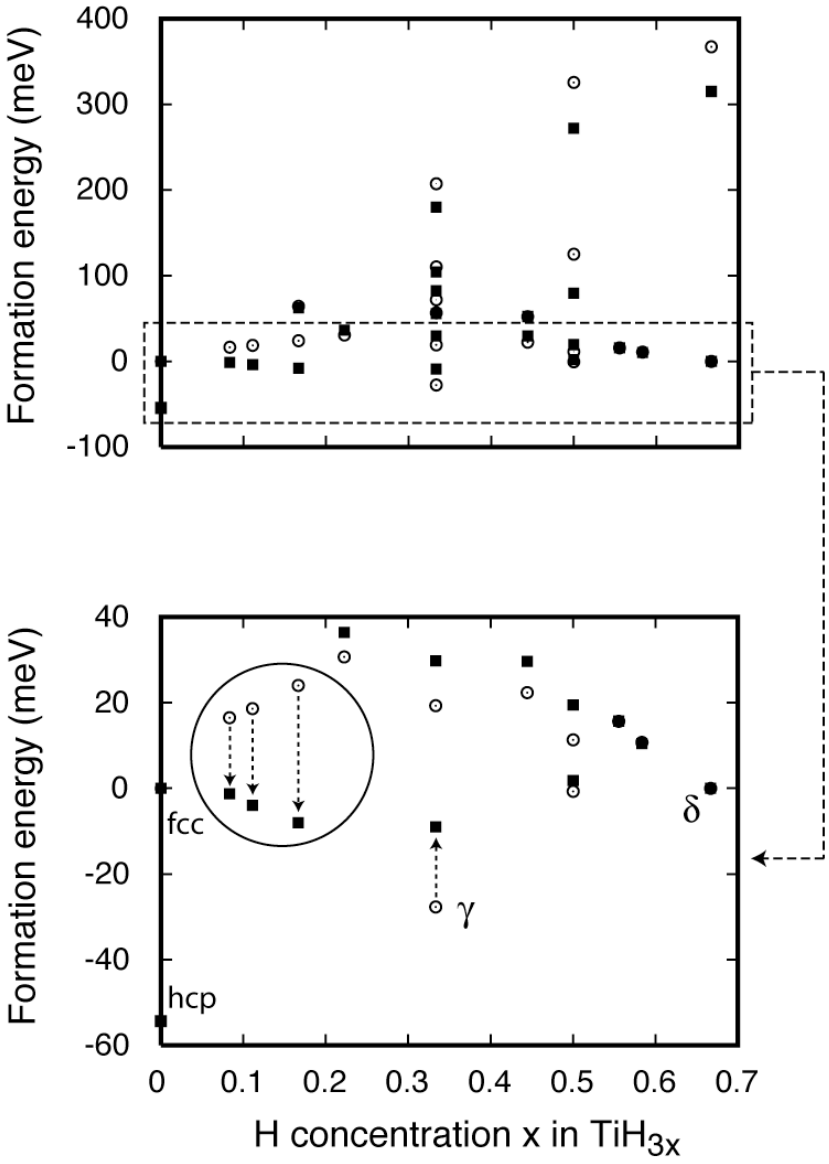

Figure 3-8 Calculated formation energies of various configurations of TiH_{3x} with (squares) and without (circles) zero-point vibrational energies. Reference states are fcc Ti and δ-TiH_2. The circled energies correspond to configurations with exclusively octahedral occupancy. All other energies in the enlarged plot (bottom) correspond to configurations with exclusively tetrahedral occupancy.

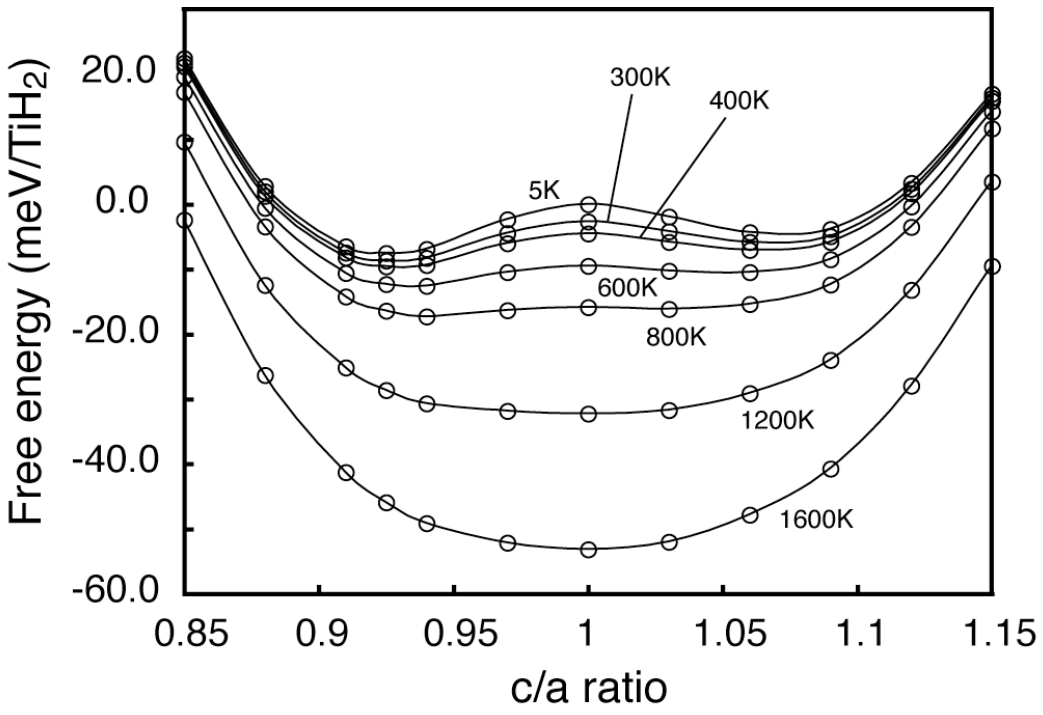

Figure 3-9 Free energies of TiH_2 as a function of c/a ratio, calculated with Fermi broadening of the electron distribution at various temperatures.

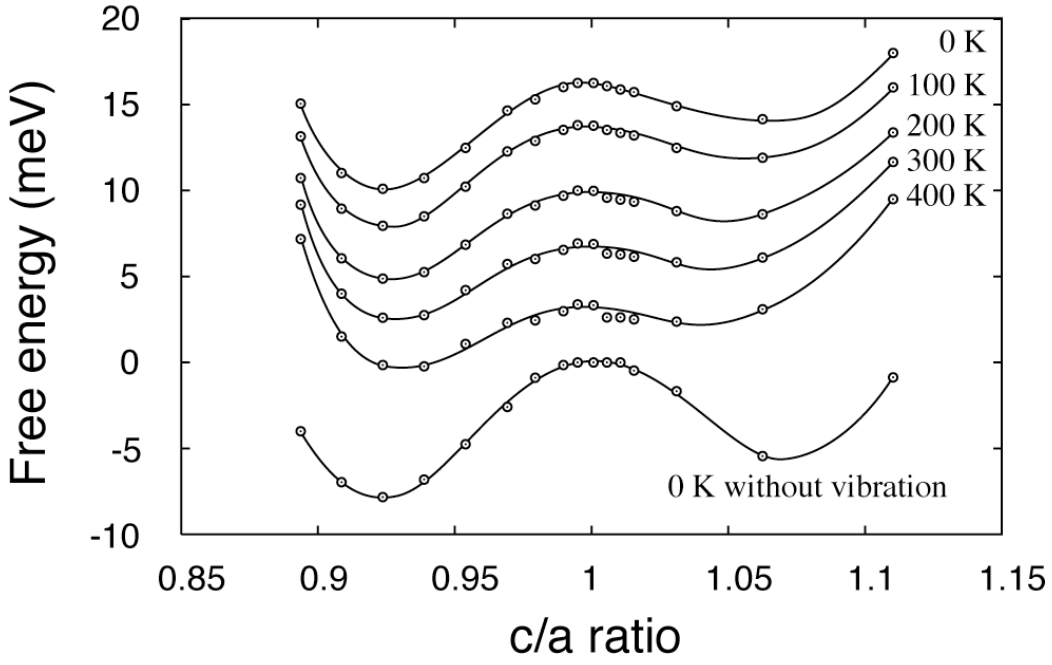

Figure 3-10 Constrained free energies of TiH_2 as a function of c/a ratio, calculated within the harmonic approximation using a first-principles parameterized spring model. The free energies at finite temperature are shifted to fit in one plot.

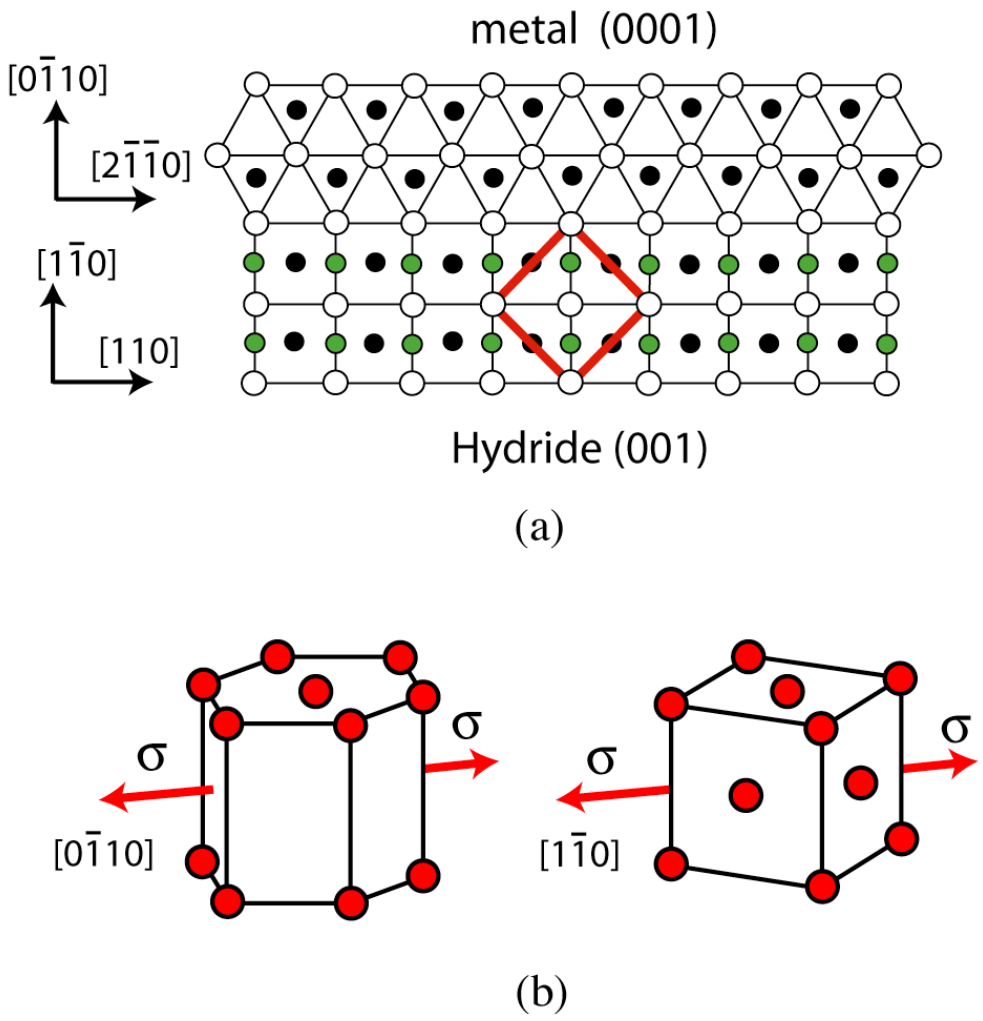

Figure 3-11 (a) The experimentally observed (Ref. 35) habit plane between α-Ti (hcp) and coherent γ-TiH precipitates. Empty and black circles are Ti atoms of successive (0001) and (001) planes of hcp and fcc hosts and green circles are tetrahedrally coordinated hydrogen atoms. (b) Schematic illustration of the orientation of the axis of tension relative to the hcp and fcc hosts used to investigate the role of stress on hydride phase stability.

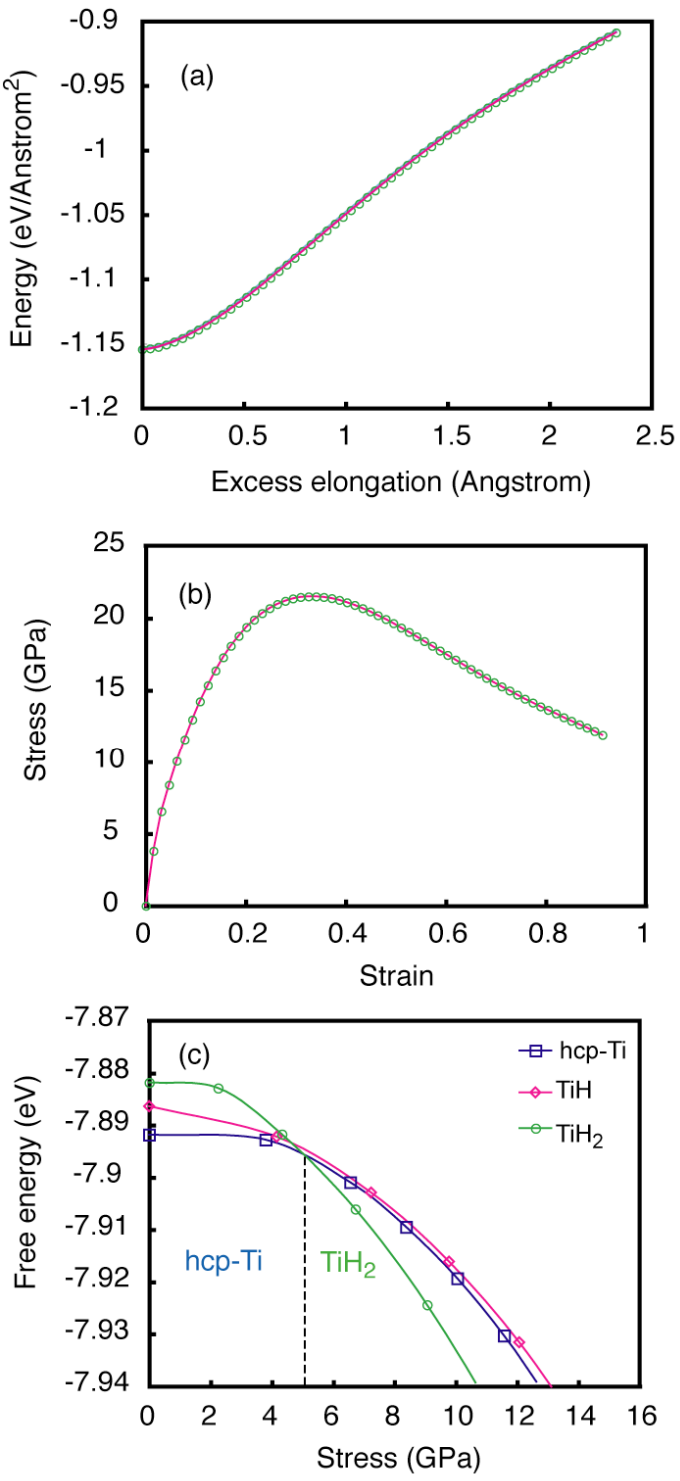

Figure 3-12. (a) The energy as a function of excess elongation along $[0\bar{1}10]$ direction for hcp-Ti. (b) The traction curve for hcp-Ti obtained as the derivative of the plot in (a). (c) Free energies for hcp-Ti, TiH and TiH_2 as a function of stress for μ_H = -5meV without coherency strains.

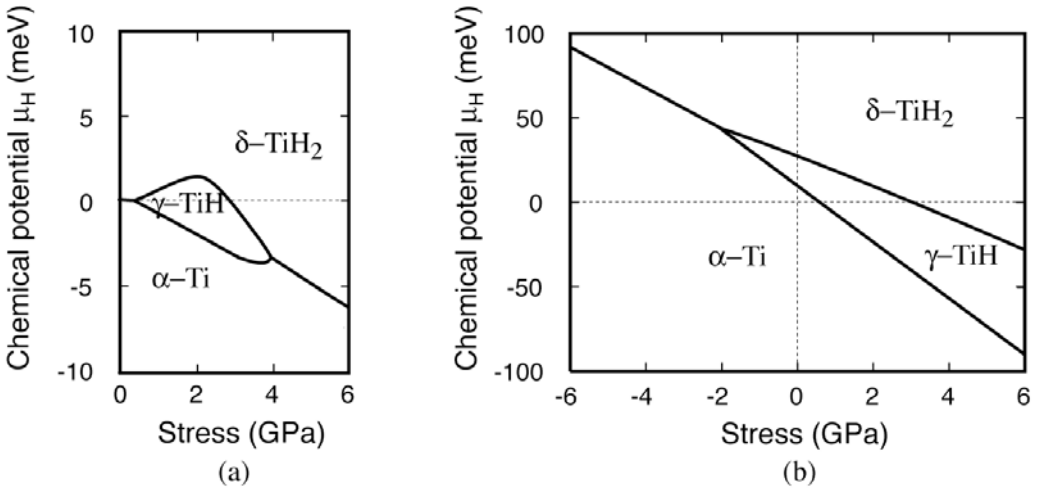

Figure 3-13 Calculated 0 K phase diagrams as a function of hydrogen chemical potential and stress (see Fig. 3-11 for the orientation of the applied stress relative to the various crystals). (a) Phase diagram in the absence of coherency strains (i.e. equilibrium lattice parameters perpendicular to the axis of tension). (b) Phase diagram accounting for coherency strains that exist across the habit plane of Fig. 3-11(b).

	a(A)	c(A)
hcp Ti	2.944	4.644
	2.95	4.68[a]
γ–TiH	4.1681	4.584
	4.21	4.6[b]
δ–TiH_2	4.414	
	4.404[c]	

Table 3-1 Comparison of calculated lattice parameters with experimental results (see Ref. 35, 37, and 118).

a. Reference 118.
b. Reference 35.
c. Reference 37.

Chapter 4

First-principles investigation of migration barriers and point defect complexes in a substitution solid: B2-NiAl

In chapter 3, we investigated the thermodynamics in an interstitial solid: Ti hydride. In this and the following chapters, we will apply the similar first-principle approaches to a substitution solid: B2-NiAl compound; the emphasis will be put on the kinetic properties in this compound.

4.1 Important hop mechanisms in B2-NiAl

In this chapter, we survey important hop mechanisms that have been proposed for B2-NiAl and calculate their migration barriers from first principles. We also explore new hop mechanisms and further show that the migration barriers for a variety of hop mechanisms are sensitive to the local environment. As any nearest neighbor hop in B2-NiAl leads to a disruption of long-range order, several migration sequences involving a succession of hops have been proposed, including the various six jump cycle mechanisms (6JC) [47,63,66], the migration of triple defect complexes [49,67] and the anti-structural bridge mechanism (ASB) [52]. These hop sequences involve a combination of nearest neighbor and second nearest neighbor atom-vacancy exchanges as well as two atom-vacancy exchanges [58]. As the concentration and nature of point defects changes with alloy composition, we pay special attention to the effect of local short-range order on migration barriers for various hop mechanisms.

We used first-principles electronic structure methods based on density functional theory (DFT) within the generalized gradient approximation (Perdew-Wang 91 parameterization of the exchange correlation potential) to estimate migration barriers and to calculate defect formation energies in B2-NiAl. To this end, we used the VASP plane-wave pseudopotential code [90,91] and treated the core-electron interactions with the projector augmented wave (PAW) method [89,92]. For the Ni atoms, the 3*p* semi-core states were treated as valence states. The *k* point-grids were sampled with the Monkhorst and Pack method [116] and partial occupancy at the Fermi level was treated with the method of Methfessel and Paxton [117]. A plane-wave basis set cutoff energy of 500eV was used. The ionic positions and the lattice parameters of each structure were fully relaxed. Convergence tests of the energy with respect to *k* point grids indicated that *k*-point sampling errors are less than 5 meV per Ni x_{Ni}Al $x_{Al}\varnothing\, x_V$ formula unit, where $\varnothing$ stands for a vacancy.

As magnetism can play a role in affecting total energies of alloys containing Ni, we compared energies of the experimentally observed compounds in the Ni-Al system calculated with and without spin-polarization (ferromagnetic ordering). While spin-polarization affects the energies of pure Ni and $L1_2$ Ni_3Al, the maximum difference between the spin-polarized and non-spin-polarized total energies was found to be less than 0.5 meV/site for fcc Al, $D0_{11}$ $NiAl_3$, $D5_{19}$ Ni_2Al_3 and "Pt_5Ga_3" type Ni_5Al_3. No difference was found between spin polarized and non-spin polarized energies for B2 NiAl. We therefore neglected spin polarization in the calculation of migration barriers and the energies of different point defect configurations in B2-NiAl.

We used the nudged elastic band method to calculate migration barriers. For some atomic hop mechanisms, though, the activated state is at a high symmetry point and there is no need to use the nudged elastic band method to calculate the barrier height. In these cases, we directly

calculated the energy of the activated state and the initial state. All calculations of migration barriers were performed in a 54-site supercell of B2 NiAl using a $3 \times 3 \times 3$ *k*-point mesh, which ensured a *k*-point sampling error of less than 1.2 meV per Ni x_{Ni}Al $x_{Al}\varnothing\, x_V$ formula unit.

4.1.1 Nearest-neighbor hops

The most common hop mechanism in metallic alloys is a nearest neighbor hop of an atom into an adjacent vacant site. If the Al-sublattice contains a vacancy, then a nearest neighbor Ni atom can hop into that vacant site to create a Ni-antisite defect, leaving behind a vacancy on the Ni sublattice. In B2-NiAl, the concentration of defects can be very high, and the migrating Ni atom could also be surrounded by additional defects. We calculated the migration barriers of Ni nearest-neighbor hops with the nudged elastic band method for three local environments. These are illustrated in Fig. 4-1 together with the calculated energy along the migration path. In Fig. 4-1(a), Ni migrates into an isolated Al-vacancy, while in Fig. 4-1(b), Ni performs a nearest neighbor hop in the presence of an adjacent Ni vacancy and in Fig. 4-1(c), Ni performs a nearest neighbor hop in the presence of a second Al vacancy. Figure 4-1 shows that nearest neighbor Ni hops have relatively low barriers, ranging between 0.31 eV and 1.1 eV (depending on the direction of the hop). Furthermore, Fig. 4-1 shows that the local environment can have a significant influence on nearest neighbor migration barriers. The presence of a Ni vacancy will increase the Ni nearest neighbor migration barrier from 0.35 eV to 0.65 eV, while the presence of second Al vacancy has little influence on the migration barrier.

Nearest neighbor Al-hops into an adjacent vacancy on the Ni sublattice is in principle also possible. However, in B2-NiAl, Mishin et al [58], while investigating the 6JC mechanism, showed that the endpoint of such a hop is mechanically unstable, and the Al atom will relax back

to its original position on the Al-sublattice. Our first-principles calculations confirm this prediction suggesting that Al-nearest neighbor hops to the Ni-sublattice do not occur.

4.1.2 Second nearest neighbor hops

B2-NiAl has a relatively open crystal structure (as it is a super structure ordering of bcc) and can therefore also accommodate second nearest neighbor hops. Second nearest neighbor hops do not disrupt long-range order in B2-NiAl as the migrating atoms remain on their own sublattice. The activated state of a second nearest neighbor hop resides on a mirror plane between the endpoints, enabling us to calculate the migration barrier by placing the migrating atom at the midpoint of the hop. Figure 4-2 illustrates the migration barriers for several possible second nearest neighbor hops. In the absence of any additional defects, the second nearest neighbor hop of an Al atom into an Al-vacancy has a migration barrier of 1.49 eV, which is close to half of the predicted migration barrier for a second nearest neighbor hop of a Ni atom into a Ni-vacancy of 2.76 eV. Hence, an Al atom exchanges more frequently with a second nearest neighbor vacancy (on the Al sublattice) than does a Ni atom with a second nearest neighbor (on the Ni sublattice). However, the overall frequency of second nearest neighbor hops is also very sensitive to the availability of vacancies on the Al sublattice and on the Ni sublattice.

As with the first-nearest neighbor hops, the second nearest neighbor migration barriers are significantly affected by the close proximity of additional defects. If a second nearest neighbor Al hop occurs in the vicinity of a Ni vacancy as illustrated in Fig. 4-2 (c), the predicted migration barrier drops by almost half, from 1.49 eV to 0.75 eV. Hence, the presence of Ni vacancies will enhance Al second nearest neighbor hops (holding the number of Al-vacancies constant). In the opposite configuration, where a Ni second nearest neighbor hop is attempted in

the vicinity of an Al vacancy as illustrated in Fig. 4-2 (d), our DFT-GGA calculations show that the Ni placed at the activated state, simply relaxes to the vacant Al-site. Hence Ni second-nearest neighbor hops adjacent to an Al-vacancy do not occur as one hop, but decompose into two nearest neighbor hops (see Fig. 4-1 (b)) for the migration barriers for these nearest neighbor hops).

Figure 4-2 (e)-(h) shows the possible next nearest neighbor hops for anti-site Al atoms (Al_{Ni}) and anti-site Ni atoms (Ni_{Al}). It can be seen from Fig. 4-2 (e)-(h) that the second nearest neighbor migration barriers for these defects are also significantly affected by the close proximity of additional defects. The second nearest neighbor hop of an anti-site Al atom into a Ni-vacancy has a migration barrier of 2.42 eV (Fig. 4-2 (e)), however, if there is a vacancy at the nearest neighbor Al-sublattice site, our DFT-GGA calculations show that the anti-site Al atom is placed at the activated state and simply relaxes to the vacant Al-site (Fig. 4-2 (g)). As for the second nearest neighbor hop of anti-site Ni atom, we can see from Fig. 4-2(f) that the migration barrier is 2.05eV if there is no additional vacancy around. On the other hand, if an anti-site Ni second nearest neighbor hop is attempted in the vicinity of a Ni vacancy as illustrated in Fig. 4-2 (h), our DFT-GGA calculations show that the Ni placed at the activated state, simply relaxes to the vacant Ni-site. Hence anti-site Ni second-nearest neighbor hops adjacent to an Ni-vacancy do not occur as one hop, but decompose into two nearest neighbor hops (see Fig. 4-1 (c)) for the migration barriers for these nearest neighbor hops).

4.1.3 Migration barriers for six-jump-cycles (6JC) migration sequence

While nearest neighbor Al hops into vacancies on the Ni-sublattice are mechanically unstable, B2-NiAl alloys in thermodynamic equilibrium do contain small concentrations of Al-

antisite defects on the Ni-sublattice. Mishin [58] et al in studying the 6JC hop sequence, suggested that Al can hop into vacancies on the Ni-sublattice through a collective hop mechanism involving the simultaneous migration of two atoms. In this thesis, we systematically investigated six-jump-cycles migration sequence and the simultaneous two-atom hops involved in it.

There are three types of six-jump-cycle sequences, which are [110], straight [100] and bent [100] types. The original version of six-jump-cycle sequences involves six nearest neighbor hops [47,66], however, in recent years several researchers using either embedded atom model or DFT calculations have shown that some of these nearest neighbor hops are combined into one two-atom hop [58,129]. Thus the original six-jump-cycle sequence should be three- or four-jump-cycle sequences. Using DFT-GGA calculations, we systematically investigated the six-jump-cycles and Fig. 4-3, 4-4 and 4-5 shows the migration path and corresponding migration barriers for [110], straight [100] and bent [100] types respectively.

From Fig. 4-3 we can see that the [110] six-jump-cycle sequence involves three [110] collective hops instead of six nearest neighbor hops. In the first [110] collective hop, an Al atom migrates to a nearest neighbor vacant site on the Ni sublattice, while a Ni atom along the [110] direction from the Ni vacancy simultaneously migrates to fill the Al site (see Fig. 4-3(a1)). The migration barrier for this collective hop mechanism calculated with the nudged elastic band method is around 2.36eV. Instead of involving one Ni atom and one Al atom, the second [110] collective hop involves two Al atoms. An Al atom migrates to a nearest neighbor vacant site on the Ni sublattice, while an anti-site Al atom along the [110] direction from the Ni vacancy simultaneously migrates to fill the Al site (see Fig. 4-3(a2)). The calculated migration barrier for the second collective hop is around 0.53eV. The third [110] collective hop follows the second

and is simply the reverse of the first [110] collective hop. In the third [110] collective hop, an anti-site Ni atom migrates to a nearest neighbor vacant site on the Ni sublattice, while an anti-site Al atom along the [110] direction from the Ni vacancy simultaneously migrates to fill the Al site (see Fig. 4-3(a3)). After these three [110] collective hops, the order of the compound has restored. The net result is that one Ni atom exchanges position with one vacancy on Ni sublattice along [110] direction, and two Al atoms exchanges positions with each other.

The collective hop can also occur in the [100] six-jump-cycle sequence, both straight and bent configuration. From Fig. 4-4(a1) we can see that the first hop in the straight [100] six-jump-cycle is a collective hop involving one Ni atom and one Al atom. The Al atom moves to a nearest neighbor Ni vacancy while a Ni atom along the [100] direction from the Ni vacancy simultaneously moves to the site originally occupied by the Al atom. The calculated migration barrier for this collective hop is around 2.88eV, much higher than that of the first collective hop in [110] six-jump-cycle sequence. The final hop in straight [100] six-jump-cycle sequence is simply the reverse of the first collective [100] hop (see Fig. 4-4(a4)) and we will not describe it in details. Also, the first and the final hops in the bent [100] six-jump-cycle sequence are the same as those in the straight [100] six-jump-cycle sequence and they are also collective hops (see Fig. 4-5(a1)(a4)).

An interesting phenomenon occurs in the intermediate hops in both the straight [100] six-jump-cycle and the bent [100] six-jump-cycle sequences. For instance, for the straight [100] six-jump-cycle sequence, the calculation of previous researchers shows that the intermediate hops are either two consecutive nearest-neighbor hops (see Fig. 4-4(a2) and (a3)), where the middle configuration (see Fig. 4-4(a3)) is a stable configuration [Mishin using EAM, ref. 58], or a collective hop obtained by combining these two consecutive nearest-neighbor hops, where the

middle configuration (see Fig. 4-4(a3)) is an activated state [Emily using DFT, ref. 129]. For the bent six-jump-cycle sequence, these researchers make the same arguments. Our DFT-GGA calculations show, however, that the intermediate hop in both the straight [100] six-jump-cycle and the bent [100] six-jump-cycle sequences involves an anti-site Al atom exchanging with a next-nearest-neighbor Ni vacancy (see Fig. 4-4(a2), Fig. 4-5(a2)) instead of two consecutive nearest-neighbor hops of two Al atoms or a collective hop involving these two Al atoms. This can be seen clearly from the migration barrier plots, i.e. Fig. 4-4(b) and Fig. 4-5(b). From Fig. 4-4(b) we can see that the overall migration barrier for the straight [100] six-jump-cycle sequence is at least 3.76eV if the intermediate hop consists of two consecutive nearest-neighbor hops or a collective hop combined by these two consecutive nearest-neighbor hops; while the overall barrier drops to 3.47eV if the intermediate hop involves an anti-site Al atom exchanging with a next-nearest-neighbor Ni vacancy. In the bent [100] six-jump-cycle sequence, the overall migration barrier drops from at least 3.61eV in the case of nearest-neighbor intermediate hop to 3.47eV in the case of next-nearest-neighbor intermediated hop (see Fig. 4-5(b)).

In summary, our DFT-GGA calculations show that the six-jump-cycle sequence is actually a three-jump-cycle sequence. For [110] six-jump-cycle sequence, it involves three consecutive collective hops, for both straight and bent [100] six-jump-cycle sequence, the first and the final hops are collective hops and the middle hop is a next-nearest-neighbor hop. The calculated migration barriers for [110] six-jump-cycle sequence, straight [100] and bent [100] six-jump-cycle sequences are 2.59eV, 3.47eV and 3.47eV respectively.

4.1.4 Migration barriers for the triple defect migration sequence

Frank et al [49] proposed a diffusion mechanism involving the net migration of a triple-defect complex, which consists of a pair of vacancies on the Ni sublattice next to a Ni-antisite defect on the Al sublattice. They suggested a migration sequence involving four nearest neighbor hops separated by three intermediate stable configurations. The net result of a triple defect migration sequence is the direct exchange of an Al atom with a Ni antisite atom. Simultaneously, a vacancy pair shifts by one lattice spacing.

Using DFT-GGA and the nudged elastic band method to calculate the minimum energy path, we find that the triple defect migration mechanism in fact consists of two nearest neighbor hops separated by an intermediate second nearest neighbor hop of an Al atom (see Fig. 4-6(a)). The intermediate Al second nearest neighbor hop occurs with an adjacent vacancy on the Ni-sublattice, resulting in a low migration barrier of 0.75eV. The calculated migration barriers for this triple defect hop sequence are relatively low (ranging between 1.1eV and 0.75eV). However, the importance of this hop mechanism will depend on the equilibrium concentration of triple defects.

In addition to the previous triple-defect sequence, which we called [100] triple-defect sequence since the initial configuration includes a [100] type tripled defect cluster, where two Ni vacancies are arranged along [100] direction in the Ni sublattice and one anti-site Ni atom occupies the nearest-neighbor Al sublattice site, we proposed two other possible triple-defect sequences – [110] and [111] where two Ni vacancies lie along [110] direction and [111] direction respectively. The consecutive hops in [110] and [111] triple-defect sequences are demonstrated in the Fig. 4-7(a) and 4-8(a) and the corresponding migration barriers calculated are shown in the Fig. 4-7(b) and 4-8(b) respectively. Contrary to the relatively low migration barrier of [100] triple-defect sequence, the calculated migration barriers for [110] and [111]

triple-defect sequences are at least 2.68eV and 2.92eV, which is much higher than the migration barrier of [100] triple-defect sequence.

4.1.5 Migration barriers for the anti-structural bridge (ASB) migration sequence

The two atom collective hop does not necessarily need to occur in the six-jump-cycle sequence, it can also occur in other hop sequences such as anti-structural bridge hop sequence for Al atoms. The anti-structural-bridge hop sequence for Al atoms are illustrated in Fig.4-9 (a) and Fig. 4-10(a) and there are two types of them – [100] and [110] types where anti-site Al atom and Ni vacancy lie along [100] and [110] directions respectively. For these two paths, our computation has shown that instead of doing two consecutive nearest neighbor hops proposed by previous researchers [52], the Al atoms actually do a two-atom collective hop. That is when an Al atom on the Al sublattice is surrounded by a vacancy and an Al antisite, both on the Ni sublattice, then a pair of Al atoms could perform a collective cyclic hop with as net effect that an Al antisite atom has migrated by a second or third nearest neighbor distance. For this collective hop, the calculated migration barriers are 1.65eV and 1.01eV for [100] and [110] types respectively. This low barrier suggests that the collective two atom hops involving Al atoms is a viable transport mechanism, especially in Al-rich B2-NiAl alloys where the concentration of Ni vacancies and Al antisites are both at their highest value.

The anti-structural bridge hop can also occur for Ni atoms. Just like the anti-structural-bridge hop sequence for Al atoms, there are two types of them – [100] and [110] types where anti-site Ni atom and Al vacancy lie along [100] and [110] directions respectively (see Fig. 4-11(a) and Fig. 4-12(a)). Unlike the ASB for Al, the anti-structural-bridge sequence for Ni involves two consecutive nearest neighbor hops of Ni atom instead of collective hop. The

calculated corresponding migration barriers are 0.71eV and 1.01eV (see Fig. 4-11(b) and Fig. 4-12(b)) for [100] and [110] type respectively. This low barrier suggests that the anti-structural bridge hop involving Ni atoms is a viable transport mechanism for Ni atoms, especially in Ni-rich B2-NiAl alloys where the concentration of Ni antisites is relatively high.

4.2 Defect concentration at finite temperature

B2-NiAl offers a variety of viable atomic transport mechanisms that include nearest neighbor hops, second nearest neighbor hops, collective two atom hops as well as complex hop sequences. However, the importance of these hop mechanisms is not only determined by low migration barriers but also by the availability of particular defects or defect complexes. In this section, we investigate the concentration of relevant defects and defect complexes in B2-NiAl at finite temperature as a function of alloy concentration using grand canonical Monte Carlo simulations applied to a cluster expansion. The parameters of the cluster expansion are fit to the first-principles energies of different defect arrangements in B2-NiAl.

4.2.1 First-principles configurational energies

Ni-Al system is a complicated system and it has many order phases, which can be seen from its experiment phase diagram (Fig. 4-13) [131]. From the phase diagram we can see that as the concentration of Ni atom is increasing, many ordered phases are present. Also, many of the ordered phases cannot accommodate large off-stoichiometry and some of them are even line compounds. However, B2-NiAl, which we are interested in, can accommodate large off-stoichiometry. The reason for this phenomenon will be clear after we calculate the formation energies of various configurations in Ni-Al system.

With DFT-GGA as implemented in the VASP planewave pseudopotential code (section 4.1) we calculated the energy of a variety of different defect configurations over the sites of the B2 crystal. The technical details have been described in section 4.1. We calculated the energy of 175 configurations corresponding to different arrangements of dominant components over the two sublattices of B2-NiAl (dominant components are vacancies on the Ni sublattice and Ni antisite atoms on the Al sublattice). One configuration was in a supercell containing 128 sites, 87 configurations had supercell sizes with 54 sites and 9 configurations had supercell sizes with 16 sites while the remaining configurations were in supercells with 12 or less sites. All configurations containing a minor point defect were placed in a 54-atom supercell. For the minor defects, we considered 32 different defect configurations around an isolated (within a 54 atom supercell) Al atom on the Ni sublattice and 11 different defect configurations around an isolated vacancy on the Al sublattice.

Figure 4-14 illustrates first-principles formation energies for different configurations in the Ni-Al system. Each formation energy, $\Delta E(x_{Ni}, x_{Al})$, for a particular configuration having concentration x_{Ni}, x_{Al} and x_V=(1- x_{Ni} - x_{Al}) is defined as

$$\Delta E(x_{Ni}, x_{Al}) = E(x_{Ni}, x_{Al}) - x_{Ni} \bullet E_{Ni}^{fcc} - x_{Al} \bullet E_{Ni}^{fcc} - (1 - x_{Ni} - x_{Al}) \bullet E^{vacuum} \qquad (4\text{-}1)$$

where $E(x_{Ni}, x_{Al})$ is the total energy per crystal site for the same configuration calculated from first principles (with DFT-GGA using VASP) while E_{Ni}^{fcc} and E_{Al}^{fcc} are the first-principles energies per atom of pure Ni and Al in the fcc crystal structure. The quantity E^{vacuum} serves as the vacancy reference state and is taken as vacuum, having zero energy. Since the B2-NiAl compound can accommodate high concentrations of vacancies, these formation energies should be plotted in a three dimensional diagram with two independent concentration axes (e.g. x_{Ni} and x_{Al}). However, for clarity, we project the formation energies on a binary plot with composition

axis $x = x_{Ni}/(x_{Al} + x_{Ni})$. Also plotted in Fig. 4-14 are formation energies for other compounds observed experimentally in the Ni-Al system (see Fig. 4-13) [130,131]. These include $D0_{11}$ $NiAl_3$, $D5_{19}$ Ni_2Al_3, "Pt_5Ga_3" type Ni_5Al_3 and $L1_2$ Ni_3Al. The formation energies of these experimentally observed compounds together with that of B2-NiAl form a convex hull, illustrating that DFT within the generalized gradient approximation correctly predicts the relative stability of the intermetallic compounds in the Ni-Al system at zero Kelvin. In addition, we found that the "Ni_3Ga_4" type Ni_3Al_4 (this is also a B2 based configuration with ordered Ni vacancies in a 128 site supercell with stoichiometric formula $Ni_{48}Al_{64}\varnothing_{16}$) also resides on the ternary convex hull in x_{Ni}, x_{Al} and x_V=(1- x_{Ni} - x_{Al}) composition space, consistent with the experimental observations of this structure [130]. As is clear in Fig. 4-14, many of the B2-NiAl based configurations are close to the convex hull, suggesting that configurational disorder within this compound can be easily excited at finite temperature.

4.2.2 Cluster expansions

A cluster expansion for the dominant components of B2-NiAl (Ni and vacancies on the Ni sublattice and Ni and Al on the Al sublattice) was constructed by fitting to the first principles formation energies of 175 fully relaxed Ni-Al-vacancy configurations. By minimizing a leave-many-out cross-validation score using a genetic algorithm [94,102], an optimal set of clusters was selected from a total of 47 candidates. The cluster expansion includes 1 empty cluster, 2 points (for the Al and Ni sublattice sites), 14 pairs, 8 triplets and 1 quadruplet (see Fig. 4-15). As a measure of the accuracy of the cluster expansion, the root-mean-square (rms) error between first-principles energies and the cluster-expanded energies for all the structures used in the fit is 3

meV per site. Furthermore, as a measure of its ability to predict energies of configurations not included in the fit, the leave-one-out cross validation score is 4 meV per site.

We determined the local ECI (LECI) of the local cluster expansions for minor point defects in B2-NiAl (Al on the Ni sublattice and V on the Al sublattice) by fitting to the effective minor point defect formation energies ($\Delta E_i^{V_{Al}}$ for V_{Al} and $\Delta E_j^{Al_{Ni}}$ for Al_{Ni}, see section 2.3.3) for different configurations around an isolated minor point defect within B2 (32 configurations for Al_{Ni} and 11 configurations for V_{Al}, all calculated in 54 atom supercells). Due to the small number of configurations, a leave-one-out cross validation score was minimized using a genetic algorithm to select an optimal set of clusters from 42 candidates. For Al_{Ni} the optimal set includes the empty cluster along with 5 point and 3 pair clusters (Fig. 4-16(a)) and for V_{Al} the optimal set includes the empty cluster and one point cluster (Fig. 4-16(b)).

By combining the local cluster expansions for $\Delta E_i^{V_{Al}}$ and $\Delta E_j^{Al_{Ni}}$ with the binary coupled-sublattice cluster expansion as described in section 2.3, it is possible to calculate the energy of any configuration of Ni, Al and vacancies within the B2 compound, provided the minor defects are separated far enough not to interact with each other (as measured by the largest pair cluster of the binary coupled-sublattice cluster expansion). The accuracy of the combined cluster expansions is reflected by a 2 meV per site root mean square error between the cluster expanded and first-principles energies of 43 configurations with one minor defect.

4.2.3 Monte Carlo simulations

The coupled-sublattice cluster expansion and local cluster expansions were implemented in grand canonical Monte Carlo simulations. A Monte Carlo supercell containing 12x12x12 B2-NiAl unit cells (M=3456 sites) was used with as thermodynamic boundary conditions the

temperature, T, and chemical potentials, $\tilde{\mu}_{Ni}$ and $\tilde{\mu}_{Al}$. For each combination of (T, $\tilde{\mu}_{Ni}, \tilde{\mu}_{Al}$), we calculated the average number of Ni and Al atoms, $\overline{N}_{Ni}$ and $\overline{N}_{Al}$ as well as the concentration of point defects and defect complexes. The values of $\tilde{\mu}_{Ni}$ and $\tilde{\mu}_{Al}$ used to calculate the equilibrium concentration of point defects and defect complexes were determined by solving Eq. (A3) under the constraint that μ_V=0. All calculations presented here were performed at 1300 K.

Figure 4-17 illustrates the calculated equilibrium concentration of point defects in B2 NiAl at 1300K as a function of the alloy concentration $x = x_{Ni}/(x_{Al} + x_{Ni})$. To ensure accurate averages in the defect concentrations, 200,000 Monte Carlo passes were performed for each combination of (T, $\tilde{\mu}_{Ni}, \tilde{\mu}_{Al}$). The concentrations of point defects are defined with respect to the sublattice on which they reside. For example, the concentration of V_{Ni} is defined as the fraction of Ni sublattice sites that are vacant. Figure 4-17 clearly shows that Ni vacancies are the dominant defect for Al-rich alloy compositions and that Ni anti-site defects on the Al sublattice dominate in Ni-rich alloys, consistent with experimental observations [41] and previous mean field studies [42-44].

We also kept track of the concentrations of various defect complexes that are necessary to mediate atomic diffusion in B2-NiAl. Among the important defect complexes are different geometries of triple defects involving a Ni atom on the Al-sublattice next to a pair of vacancies on the Ni sublattice oriented along the [100], [110] or [111] directions (see Fig. 4-6(a1), 4-7(a1) and 4-8(a1) respectively). The probability that a cluster with two Ni-sublattice sites and an adjacent Al-sublattice site is occupied by a triple defect can be numerically calculated with Monte Carlo simulations using the following expressions

$$p_{triple[100]} = \frac{\overline{N}_{triple[100]}}{12N_{cell}} \qquad p_{triple[110]} = \frac{\overline{N}_{triple[110]}}{12N_{cell}} \qquad p_{triple[111]} = \frac{\overline{N}_{triple[111]}}{4N_{cell}} \tag{4-2}$$

where $\overline{N}_{triple[100]}$, $\overline{N}_{triple[110]}$ and $\overline{N}_{triple[111]}$ are the ensemble averages of the total number of [100], [110] and [111] triple defects respectively within the Monte Carlo cell and N_{cell} is the number of B2 unit cells equal to $M/2$. Each cubic unit cell can potentially accommodate 12 [100] triple defects, 12 [110] triple defects and 4 [111] triple defects. In the absence of any interactions among vacancies and Ni anti-site atoms, this probability reduces to the product of site concentrations $p_{meanfield} = x_{Ni_{Al}} \cdot x_{V_{Ni}}^2$, where $x_{Ni_{Al}}$ and $x_{V_{Ni}}$ are the equilibrium concentrations of Ni_{Al} and V_{Ni} respectively. Calculated triple defect probabilities $p_{triple[100]}$, $p_{triple[110]}$ and $p_{triple[111]}$ as well as the mean field triple defect concentration $p_{meanfield}$ are illustrated in Fig. 4-18. As is evident from Fig. 4-18, the more compact [100] triple defect (where vacancies are at a second nearest neighbor distance from each other) has a lower concentration than the more extended triple defect.

As described in section 4.1.4, the migration of a triple defect involves two symmetrically equivalent intermediate states consisting of a vacancy on the Al sublattice next to a vacancy on the Ni sublattice. We can gain insight about the importance of the [100] triple defect migration sequence in mediating diffusion by a calculation of the frequency of its intermediate states as reflected by the probability of V_{Al}-V_{Ni}-Al_{Al} triplets. Calculated probabilities of V_{Al}-V_{Ni}-Al_{Al} occupancies on three-point clusters consisting of neighboring Al sites and an adjacent Ni site are illustrated in Fig. 4-19(a). The probability of V_{Al}-V_{Ni}-Al_{Al} triplets varies negligibly with alloy concentration suggesting that the contribution of the triple defect migration mechanism to atomic transport is similar for both Al rich and Ni rich B2-NiAl alloys.

A final set of defect complexes that we tracked in the grand canonical Monte Carlo simulations are pairs consisting of an anti-site atom and a vacancy at second and third nearest neighbor distances from each other (i.e. the pair of defects reside on the same sublattice). The

existence of these pairs is of importance in mediating the anti-structural bridge mechanisms of diffusion in off-stoichiometric alloys in which vacancies diffuse along percolating networks of anti-site atoms. Figure 4-19(b) illustrates probabilities that second nearest and third nearest neighbor clusters are occupied by a Ni-vacancy and an Al anti site, while Fig. 4-19(c) illustrates the probabilities that such clusters are occupied by an Al vacancy and a Ni anti-site atom. The higher these probabilities, the more likely an anti-structural bridge diffusion mechanism can contribute to atomic transport. As is clear from Fig. 4-19(c), the probability that a pair connecting Al-sublattice sites is occupied by a Ni anti-site atom and an Al vacancy increases as B2-NiAl becomes more Ni rich. The probability that a pair connecting Ni-sublattice sites is occupied by an Al anti-site atom and a Ni-vacancy has a more complex dependence on alloy concentration, Fig. 4-19(b), showing a minimum at the stoichiometric composition and increase both for Al-rich and Ni-rich alloys.

4.3 Discussion

Measured interdiffusion coefficients in B2-NiAl show a strong dependence on alloy concentration, exhibiting a minimum around the NiAl stoichiometry [49,50,59,62,132]. This dependence on concentration is undoubtedly due to a variation in the equilibrium concentration of the different point defects and defect clusters that mediate atomic diffusion. Recent measurements of Paul et al [59] showed that the mobility of Al and Ni, as reflected by self-diffusion coefficients, are similar around the stoichiometric composition but differ substantially away from stoichiometry. In Al-rich alloys of B2-NiAl, the Al self-diffusion coefficient is significantly larger than the Ni self-diffusion coefficient, while in Ni-rich alloys the trend is reversed, albeit that the Ni self-diffusion coefficient is only slightly larger than that of Al [59].

Our first-principles analysis of atomic hop mechanisms in B2-NiAl of section 4.1 sheds light on those mechanisms that are likely to contribute significantly to macroscopic transport. We find for example that nearest neighbor Ni-vacancy exchanges have relatively low migration barriers (ranging from 0.31-1.1 eV, see Fig. 4-1) and confirm that nearest neighbor Al-vacancy exchanges cannot occur in B2-NiAl as was first discovered by Mishin et al [58]. We also predict that the migration barrier for Al second nearest neighbor hops (1.49 eV) is about half that for Ni second nearest neighbor hops (2.76 eV, see Fig. 4-2). As Al cannot perform nearest neighbor hops in B2-NiAl, Mishin et al [58] proposed a collective two-atom hop mechanism to enable Al atoms to migrate from the Al-sublattice to the Ni-sublattice. This mechanism, involving an Al and a Ni atom, has a relatively high migration barrier (~2.5eV, see Fig. 4-3). In the present work, however, we found that if the collective two-atom hop involves a pair of Al atoms, one from the Al sublattice and the other an Al anti-site atom on the Ni sublattice, the migration barrier is significantly lower, having a value of approximately 1eV (see Fig. 4-10). This result suggests that the anti-structural bridge mechanism is likely to be very important in mediating diffusion in Al-rich alloys.

We also showed in section 4-1 that the presence of additional defects in the vicinity of the hopping atom can have a significant influence on migration barriers. For example, the Ni nearest neighbor hop barrier is almost doubled in the presence of an adjacent Ni-vacancy (compare Fig. 4-1(a) with Fig. 4-1(b)). The Al second nearest neighbor hop barrier, on the other hand, is reduced from 1.49 eV to 0.75 eV when it occurs next to a Ni-vacancy (Fig. 4-2). The low nearest neighbor Ni migration barriers coupled with the low Al second nearest neighbor barrier in the presence of Ni vacancies renders the triple defect migration sequence of Fig. 4-6 quite favorable from an energetic point of view. The triple defect migration mechanism predicted in section 4-1

(Fig. 4-6) differs from that proposed by Frank et al in that it occurs with only two intermediate states instead of three and proceeds with a combination of nearest and second nearest neighbor hops instead of only nearest neighbor hops.

The predicted migration barriers show that there are a variety of migration mechanisms with relatively low barriers (ranging around 1 eV) and a subset characterized by high migration barriers (exceeding 2 eV). The migration mechanisms with low barriers, such as the Ni nearest neighbor hop, the Al second nearest neighbor hop in the presence of a Ni vacancy and the collective hop involving a pair of Al atoms are likely to dominate in mediating transport, provided the concentration of defects necessary for these mechanisms are sufficiently high. We point out that the use of a finite sized supercell for the calculation of migration barriers from first principles introduces numerical uncertainty on predicted barriers. To estimate the accuracy of our calculated migration barriers, we calculated the barrier for the Ni-vacancy next-nearest neighbor hop in both a 3 x 3 x 3 supercell (containing 54 sites) and a 4 x 4 x 4 supercell containing (128 sites). The predicted barriers are 2.76 eV and 2.53 eV respectively, suggesting a numerical error of approximately 0.25 eV. While this error is not negligible, it is sufficiently small to allow us to distinguish between low barrier hop mechanisms (~1 eV) and high barrier hop mechanisms (~2.5 eV).

Whether or not any of the low barrier migration mechanisms dominate in mediating atomic diffusion in B2–NiAl depends on the concentration of defects and defect complexes needed to facilitate those migration mechanisms. To this end, we also investigated the equilibrium defect concentrations in B2–NiAl by applying Monte Carlo simulations to first-principles parameterized cluster expansions, thereby rigorously accounting for important interactions among the various defects in B2–NiAl. Previous investigations of defect

concentrations in B2–NiAl relied on a mean field approximation in which interactions among different defects were neglected [42-44].

A comparison of the defect concentrations calculated in this work (Fig. 4-17) with mean field predictions [42,43] shows that while the concentrations of Ni_{Al}, V_{Ni} and V_{Al} are qualitatively similar in both approaches, they differ for the predicted concentration of Al_{Ni} defects in Ni rich B2-Ni_xAl_{1-x} compounds. For the Al_{Ni} defects, our results show an increase in the Al_{Ni} concentration with alloy concentration *x* above 0.5, while previous mean field analyses predicted a decrease in the Al_{Ni} concentration [42,43]. The increase in the Al_{Ni} concentration in Fig. 4-17 arises from a local attraction between Al_{Ni} and Ni_{Al} defect pairs. Figure 4-20 shows the change in energy of a B2-NiAl crystal containing a Ni_{Al} – Al_{Ni} pair at increasing distance from each other. The configuration with a first nearest neighbor Ni_{Al} – Al_{Ni} pair is used as reference (its energy is arbitrarily set to zero). The solid line shows the energies calculated with GGA in a 3x3x3 B2 NiAl supercell (54 sites) using an energy cutoff of 500 eV and fully relaxing all atoms, while the dashed line shows the energy of a Ni_{Al} – Al_{Ni} pair as a function of increasing distance as calculated with the cluster expansions. Figure 4-20 shows an energetic attraction between Ni_{Al} and Al_{Ni} point defects. To ensure that the predicted attraction is not an artifact of the supercell size, we also calculated the energy dependence on the Ni_{Al} – Al_{Ni} pair distance in a 4x4x4 B2 NiAl supercell (128 sites) using an energy cutoff of 375 eV and allowing only internal relaxations (dotted line in Fig. 4-20). The larger supercell calculations predict the same attraction between a Ni_{Al} – Al_{Ni} pair. While the formation energy of an Al anti-site defect on the Ni sublattice is energetically very costly, the results of Fig. 4-20 clearly show that it is reduced in the immediate vicinity of a Ni_{Al} defect. Hence, any increase in the fraction of Ni_{Al} defects will lead to an increase in the fraction of Al_{Ni} defects due to short-range attractive interactions, as is

predicted with Monte Carlo simulations applied to cluster expansions that accurately capture these short-range interactions.

The inclusion of interactions among defects in B2-NiAl is also essential to accurately predict the concentration of defect complexes. Important defect complexes include various triple defects as illustrated in Fig. 4-18, which clearly illustrates a large difference between the probability of occurrence of [100] triple defects and [110] and [111] triple defects, with the former much less probable than the two triple defects having the vacancy pair aligned along [110] and [111] directions. While vacancies on the Ni sublattice are attracted to a Ni anti-site defect on the Al-sublattice, the vacancies themselves repel each other. Hence the more extended [110] and [111] triple defects are energetically favored over the [100] triple defect in which vacancies occupy nearest neighbor sites on the cubic Ni-sublattice. The probabilities of occurrence of the various triple defects also differ significantly from the mean field estimate $p_{meanfield} = x_{Ni_{Al}} \cdot x_{V_{Ni}}^2$, which neglects interactions. Figure 4-18 shows that the more compact [100] triple defect has a lower probability of occurrence than $p_{meanfield}$ while the more extended [110] and [111] triple defects have a higher probability of occurrence than $p_{meanfield}$.

The net migration of a triple defect results in the direct exchange between a Ni and an Al atom. Hence diffusion mediated exclusively by the triple defect mechanism will lead to identical mobilities for both Al and Ni atoms. Although the [110] and [111] triple defects are predicted to be more numerous than the [100] triple defects (Fig. 4-18), we found that their migration requires significantly higher energy intermediate states. In fact, DFT-GGA calculations predict the intermediate states of the [110] and [111] triple defect migration mechanism to have an energy that is more than 2.5 eV above that of the initial triple defect arrangement, while the maximum barrier along the [100] triple defect migration mechanism is not more than 1.2 eV (see

Fig. 4-6). This suggests that the [100] triple defect is more important than the [110] and [111] triple defects in mediating diffusion. While the number of triple defects diminishes slightly as B2-NiAl becomes Al-rich (Fig. 4-18), the concentration of the intermediate states of the triple defect migration mechanism remains essentially constant with alloy concentration (Fig. 4-19(a)), suggesting that the contribution of triple defects to atomic diffusion should be more or less independent of alloy concentration, diminishing somewhat in Al-rich B2-NiAl.

The anti-structural bridge diffusion mechanism becomes viable for alloy concentrations that are sufficiently off-stoichiometric to enable percolating networks of antisite atoms to form. This allows vacancies to migrate along the percolating networks without introducing additional disorder within the compound. In Ni-rich alloys, vacancies can migrate through the crystal by performing nearest-neighbor hops along chains consisting of Ni atoms on the Ni sublattice and Ni antisite atoms on the Al sublattice. As found in Section 4.1.1, these nearest neighbor Ni-vacancy exchanges have relatively low migration barriers. Furthermore, the Monte Carlo simulations indicate a high concentration of Ni antisite atoms (see Fig. 4-17) in Ni-rich alloys. A prerequisite for the anti-structural bridge mechanism for Ni-diffusion is the existence of sufficient second and third nearest neighbor pairs occupied by a Ni antisite atom and an Al-vacancy. Figure 4-19(c) shows that the concentration of Ni_{Al}–V_{Al} increases rapidly as B2–NiAl becomes Ni rich, suggesting that the anti-structural bridge mechanism should be important in mediating Ni diffusion in Ni-rich alloys.

In Al rich alloys, interconnected networks of Al-anti-site atoms are also possible, however, the concentration of Al anti-sites is significantly lower than that of Ni anti-site atoms in Ni rich alloys (see Fig. 4-17). Nevertheless, the concentration of vacancies on the Ni sublattice achieves very large values and percolating networks of Al atoms and Ni vacancies are possible.

As shown in section 4.1, the migration of Al along these percolating networks cannot occur through nearest neighbor Al-vacancy exchanges, but rather through collective two atom hops involving an Al antisite atom as illustrated in Fig. 4-10. These collective two atom hops also have relatively low migration barriers ranging between 1 and 1.6 eV. For the anti-structural bridge mechanism to be important in mediating Al diffusion, second nearest and third nearest neighbor pairs must be occupied by an Al_{Ni} and a V_{Ni}. As is clear from Fig. 4-19(b), the probability that second and third nearest neighbor pairs are occupied by Al_{Ni} and V_{Ni} increases dramatically as B2-NiAl becomes Al-rich, suggesting that the anti-structural bridge mechanism is very likely an important mechanism for Al-diffusion in Al-rich B2-NiAl. Contrary to expectation, the probability Al_{Ni} and V_{Ni} pairs also increases as B2-NiAl becomes Ni-rich, indicating that Al transport may also be mediated by the anti-structural bridge mechanism in Ni-rich alloys. The increase in Al_{Ni} and V_{Ni} pairs with $x>0.5$ in Ni_xAl_{1-x} can be attributed to the increase in Al_{Ni} defects with x due to its short-range attraction with Ni_{Al} defects.

4.4 Summary

B2-NiAl compounds exhibit a variety of complex atomic hop mechanisms and can accommodate high concentrations of diffusion mediating defects. In this paper, we systematically investigated important hop mechanism in B2-NiAl from first principles and discovered a low barrier collective hop involving a pair of Al atoms that can mediate the anti-structural bridge mechanism for Al diffusion. We also investigated the defect structure in B2-NiAl with Monte Carlo simulations, accounting for interactions among defects with a first-principles parameterized cluster expansion. An energetic attraction between Ni anti-site atoms and Al anti-site atoms leads to an increase in the Al anti-site concentration for Ni-rich B2-NiAl

compounds, which is opposite to that predicted by mean field treatments. The inclusion of interactions among defects is also essential to predict the concentration of triple defects. We also predict a dramatic increase in the number of second and third nearest neighbor pairs occupied by an Al anti-site and a Ni-vacancy as the B2-NiAl alloy becomes Al rich and Ni rich. These pairs are essential for the anti-structural bridge mechanism for Al-diffusion.

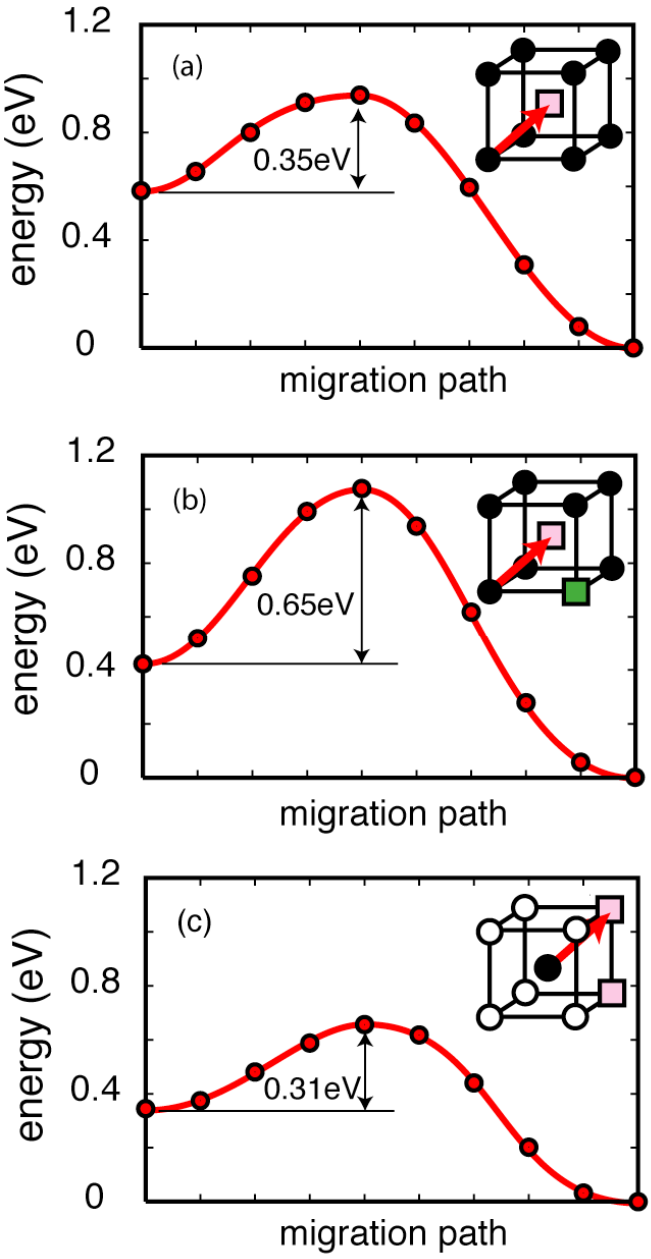

Figure 4-1 Energy along the diffusion path for Ni nearest neighbor hops (Ni_{Ni}-V_{Al} exchange) under various local environments in the B2-NiAl based compound. (a) without any additional defects. (b) with a neighboring Ni vacancy and (c) with a neighboring Al vacancy.

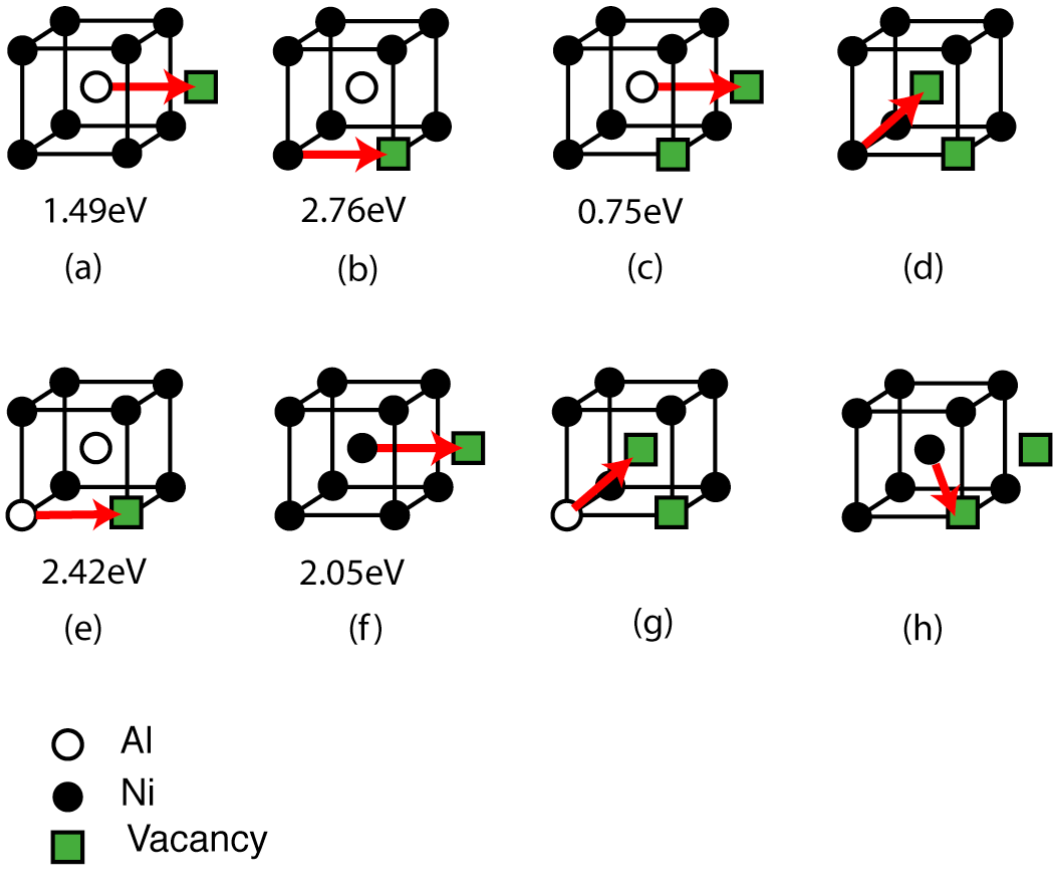

Figure 4-2 Calculated migration barriers for the next nearest neighbor hops of Ni and Al atoms under various local environments in B2-NiAl. (a) An Al atom hops to an Al vacancy without any additional defects, (b) a Ni atom hops to a Ni vacancy without any additional defects, (c) an Al atom hops to an Al vacancy with an adjacent Ni vacancy and (d) failure of a Ni second nearest neighbor hop to a Ni vacancy due to the presence of an adjacent Al vacancy, (e) an antisite Al atom hops to a Ni vacancy without any additional defects, (f) an antisite Ni atom hops to an Al vacancy without any additional defects, (g) failure of an antisite Al second nearest neighbor hop to a Ni vacancy due to the presence of an adjacent Al vacancy, (h) failure of an antisite Ni second nearest neighbor hop to an Al vacancy due to the presence of an adjacent Ni vacancy.

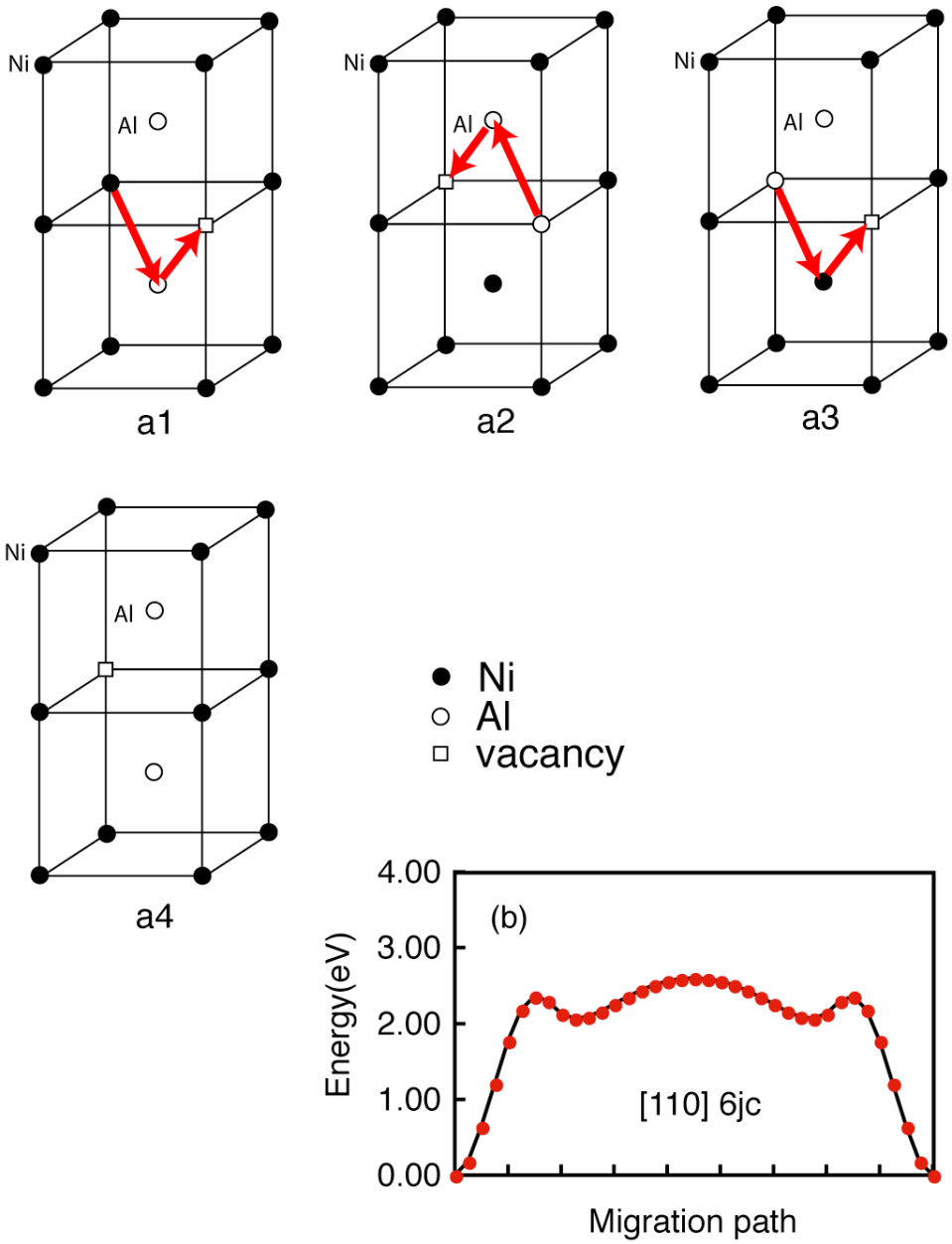

Figure 4-3 (a) The [110] six-jump-cycle sequences (a1)-(a4) in B2-NiAl, (b) variation of the energy along the [110] six-jump-cycle migration paths. The energy is relative to the initial configuration a1. The migration barriers were calculated with the nudged elastic band method.

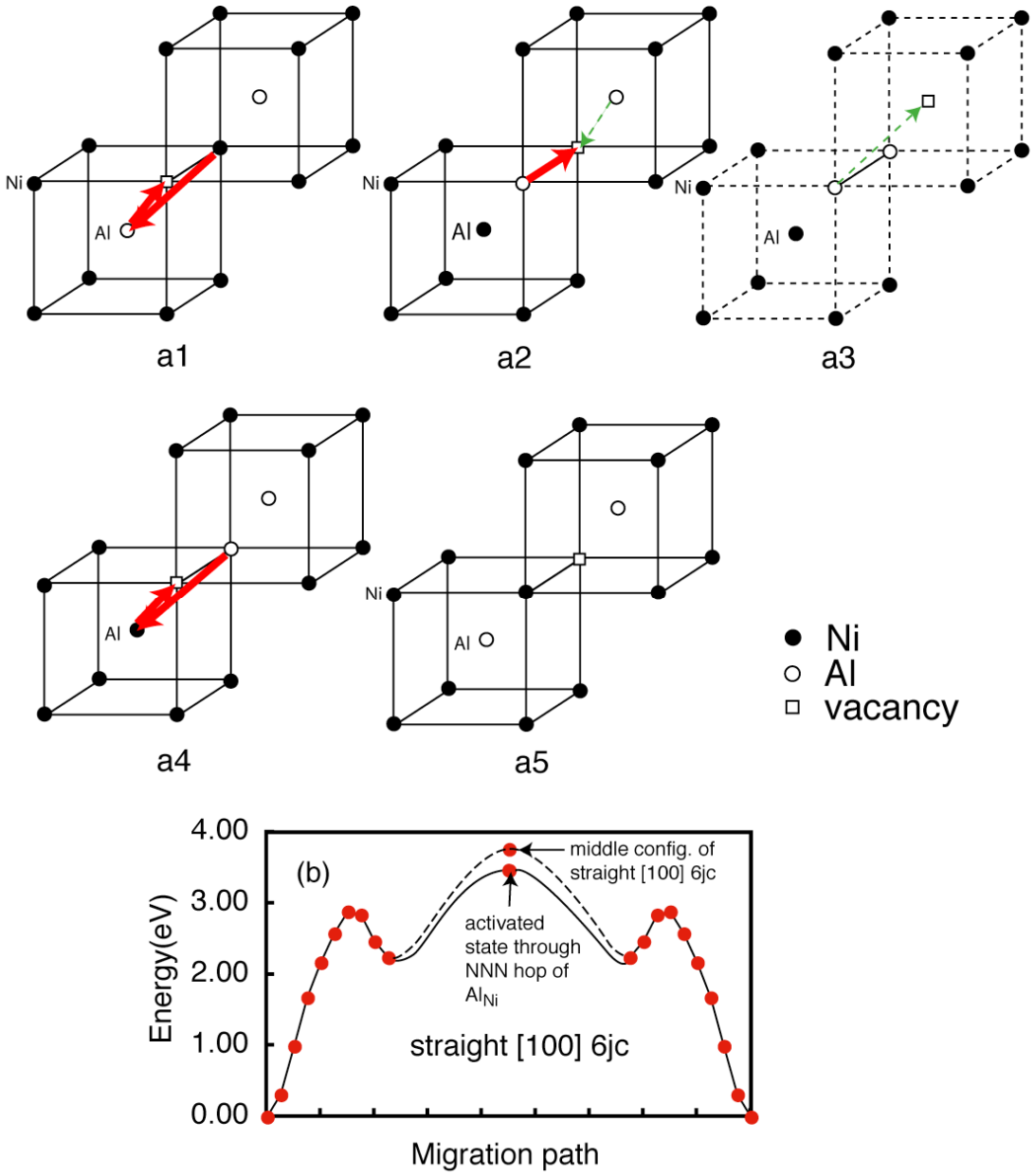

Figure 4-4 (a) The straight [100] six-jump-cycle sequences (a1)-(a5) in B2-NiAl In (a2), the antisite Al atom does second nearest neighbor hop (red line) instead of doing 2 nearest neighbor hops (green lines), so (a3) does not exist. (b) Calculated variation of the energy along the straight [100] six-jump-cycle migration paths. The energy is relative to the initial configuration (a1).

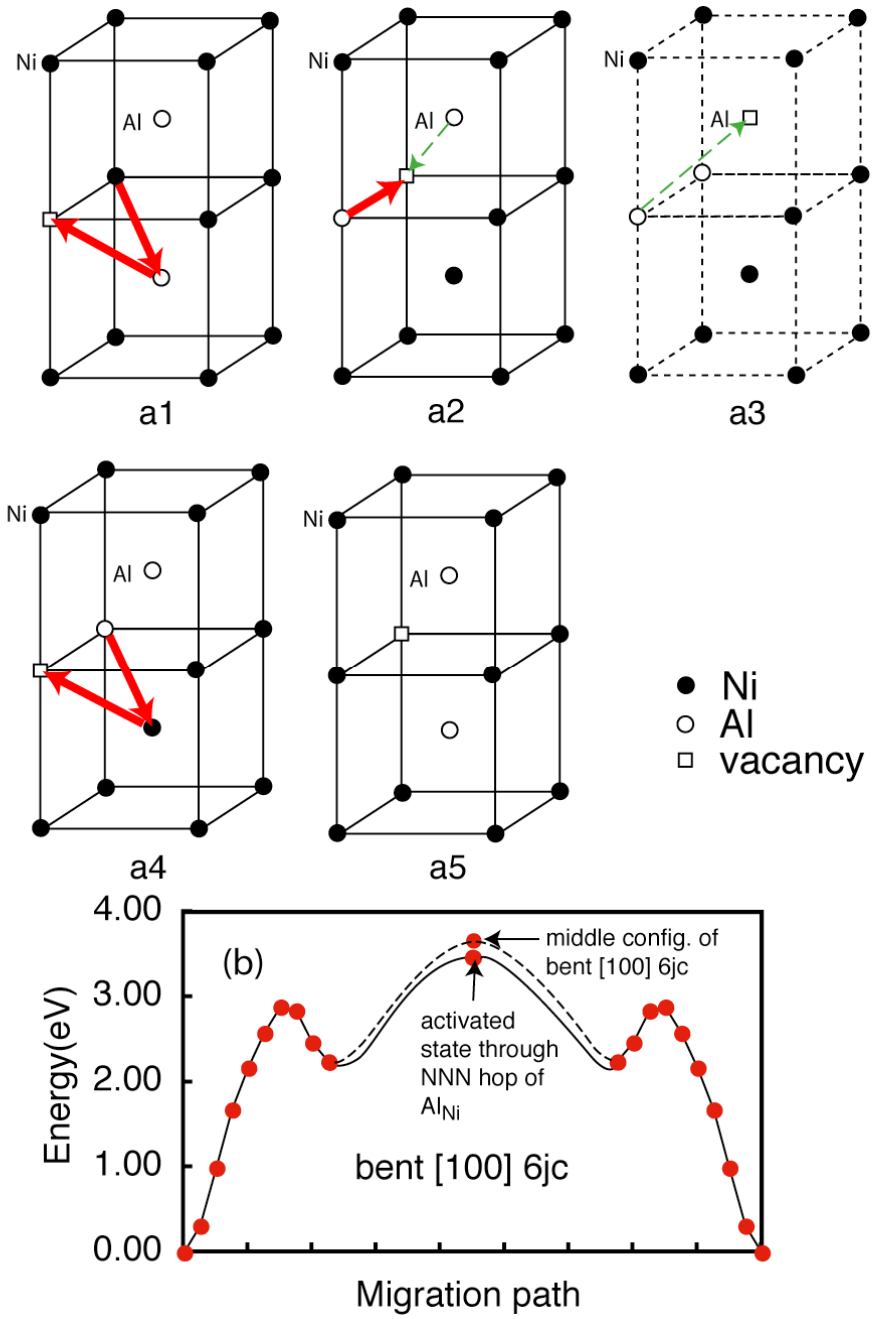

Figure 4-5 (a) The bent [100] six-jump-cycle sequences (a1)-(a5) in B2-NiAl In (a2), the antisite Al atom does second nearest neighbor hop (red line) instead of doing 2 nearest neighbor hops (green lines), so (a3) does not exist. (b) Calculated variation of the energy along the bent [110] six-jump-cycle migration paths. The energy is relative to the initial configuration (a1).

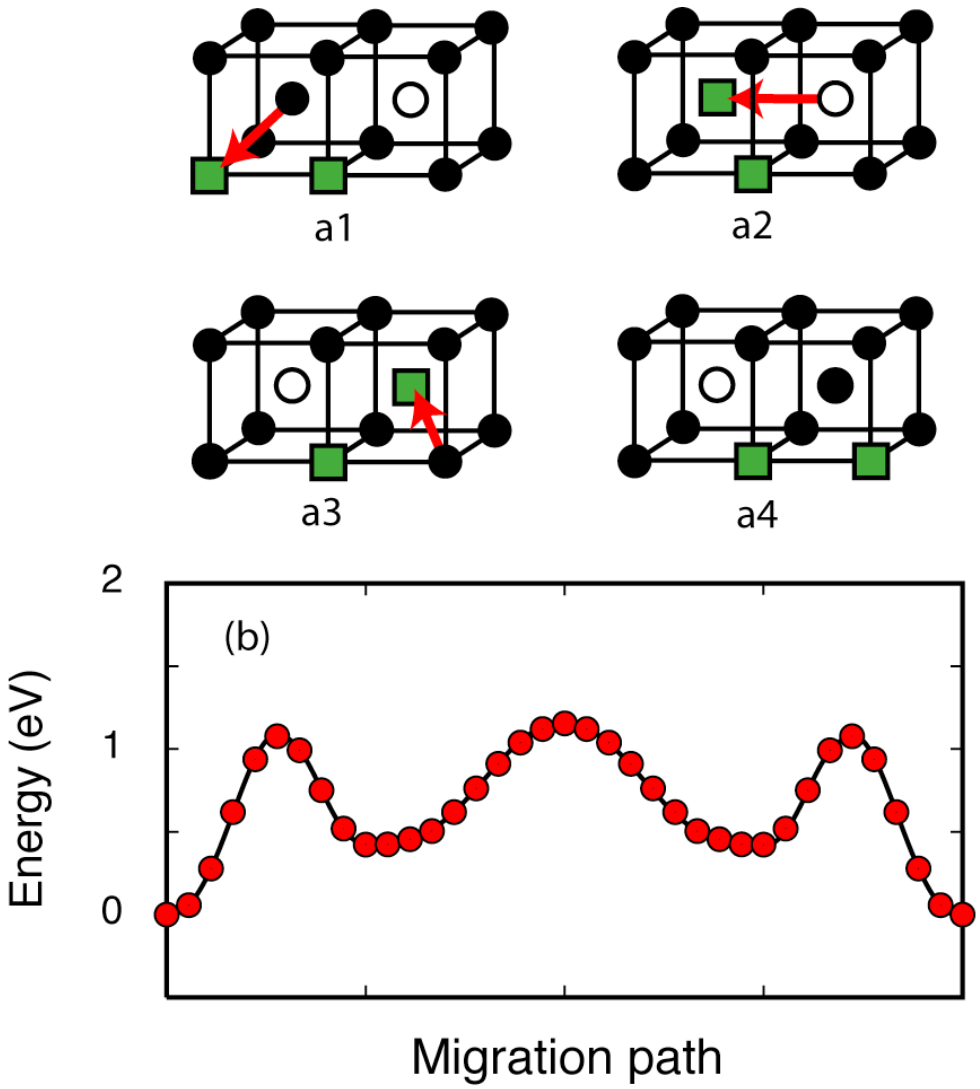

Figure 4-6 (a) The [100] triple-defect migration sequence (a1)-(a4) in B2-NiAl, and (b) The calculated variation of the energy along the [100] triple defect migration paths. The energy is relative to the initial configuration of a [100] triple defect (a1).

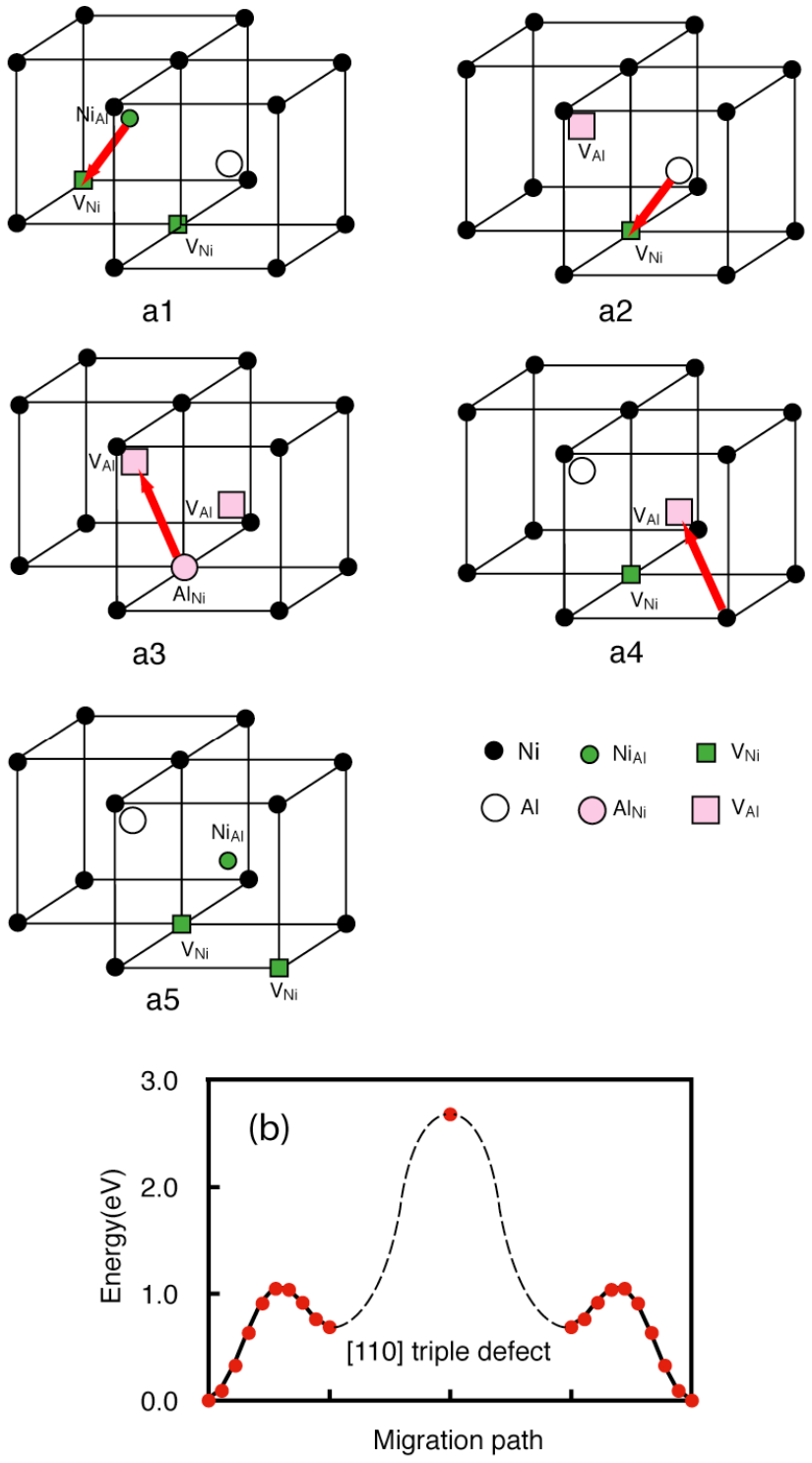

Figure 4-7 (a) The [110] triple-defect migration sequence (a1)-(a5) in B2-NiAl, and (b) The calculated variation of the energy along the [110] triple defect migration paths. The energy is relative to the initial configuration of a [110] triple defect (a1).

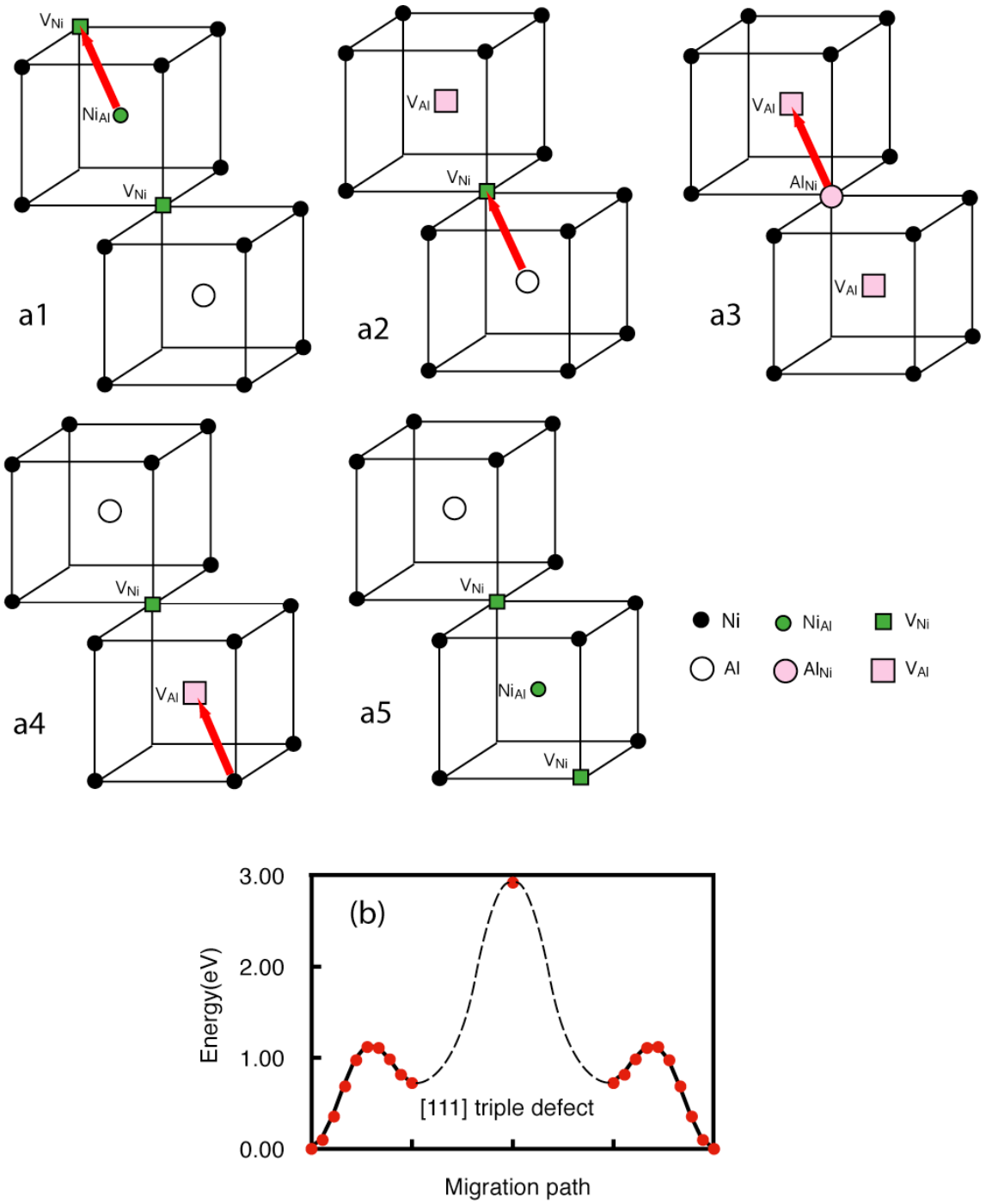

Figure 4-8 (a) The [111] triple-defect migration sequence (a1)-(a5) in B2-NiAl, and (b) The calculated variation of the energy along the [111] triple defect migration paths. The energy is relative to the initial configuration of a [111] triple defect (a1).

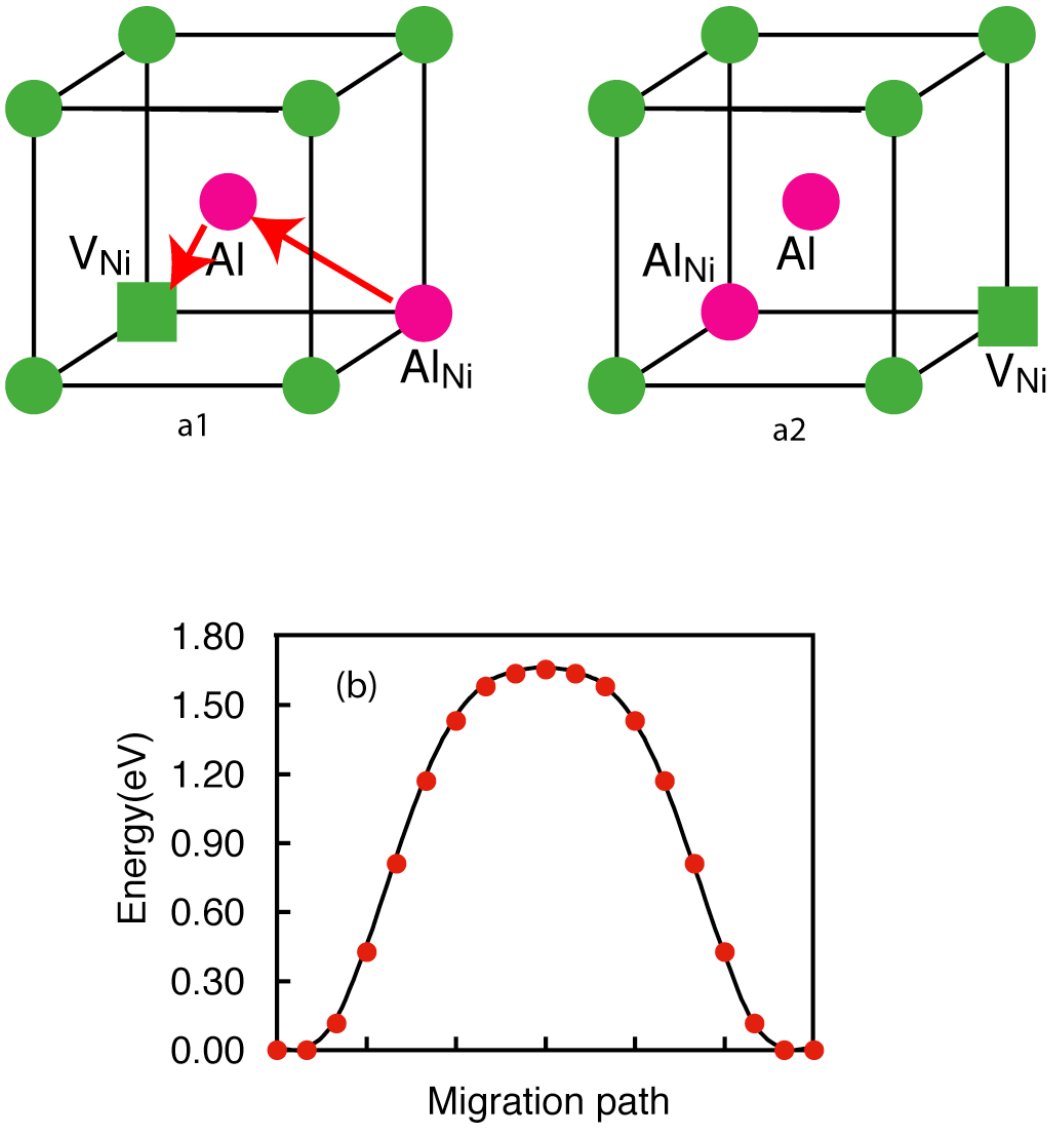

Figure 4-9 (a) The [100] anti-structural-bridge migration sequence for Al atoms in B2-NiAl, and (b) The calculated variation of the energy along the [100] anti-structural-bridge migration paths for Al atoms in B2-NiAl. The energy is relative to the initial configuration (a1).

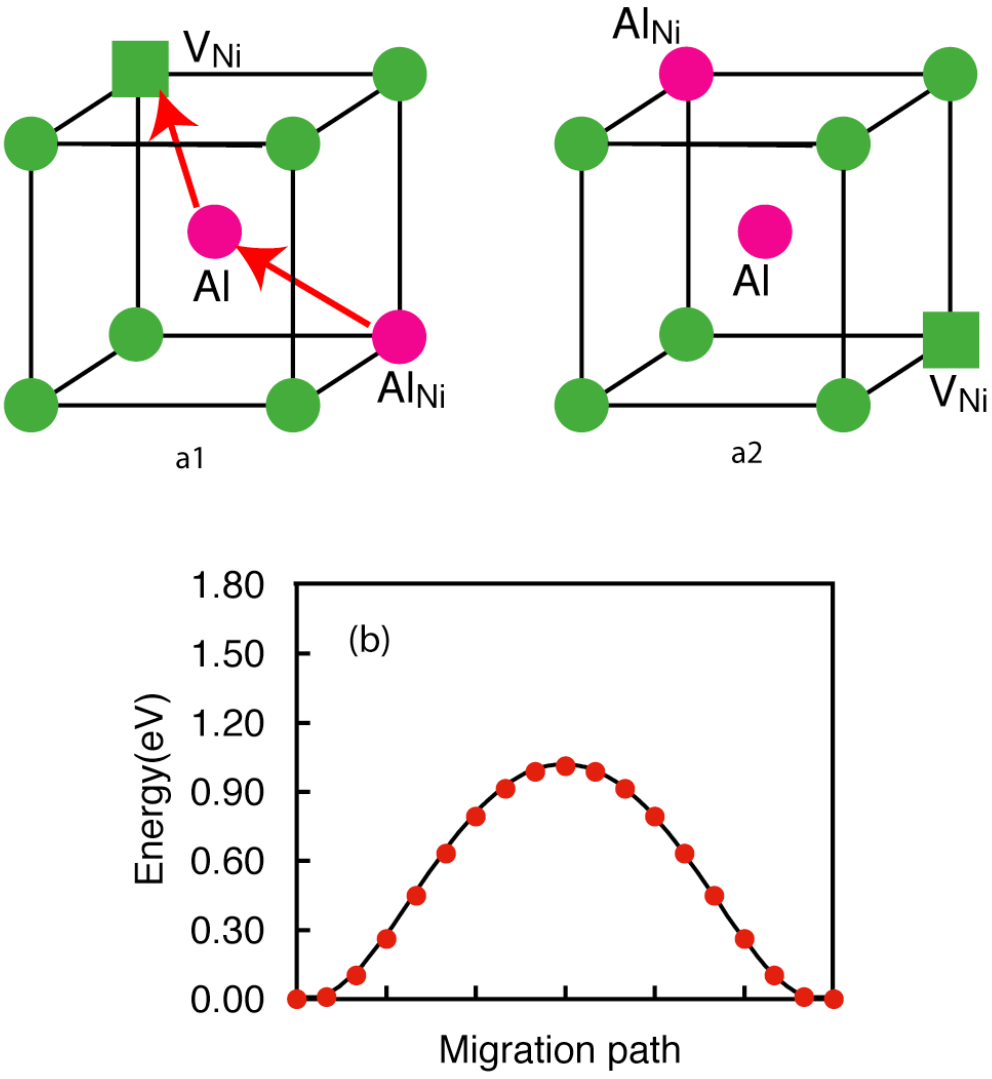

Figure 4-10 (a) The [110] anti-structural-bridge migration sequence for Al atoms in B2-NiAl, and (b) The calculated variation of the energy along the [110] anti-structural-bridge migration paths for Al atoms in B2-NiAl. The energy is relative to the initial configuration (a1).

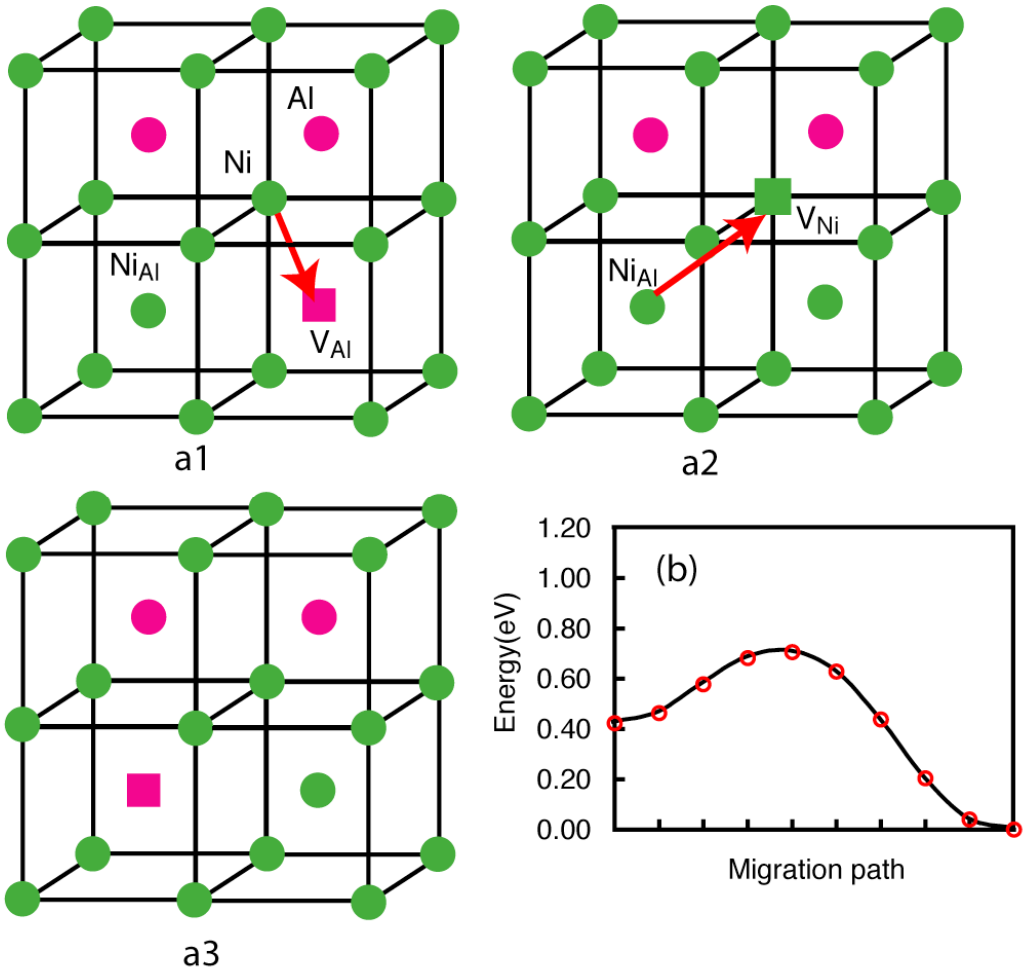

Figure 4-11 (a) The [100] anti-structural-bridge migration sequence for Ni atoms in B2-NiAl, and (b) The calculated variation of the energy along the [100] anti-structural-bridge migration paths for Ni atoms in B2-NiAl. The energy is relative to the configuration (a2).

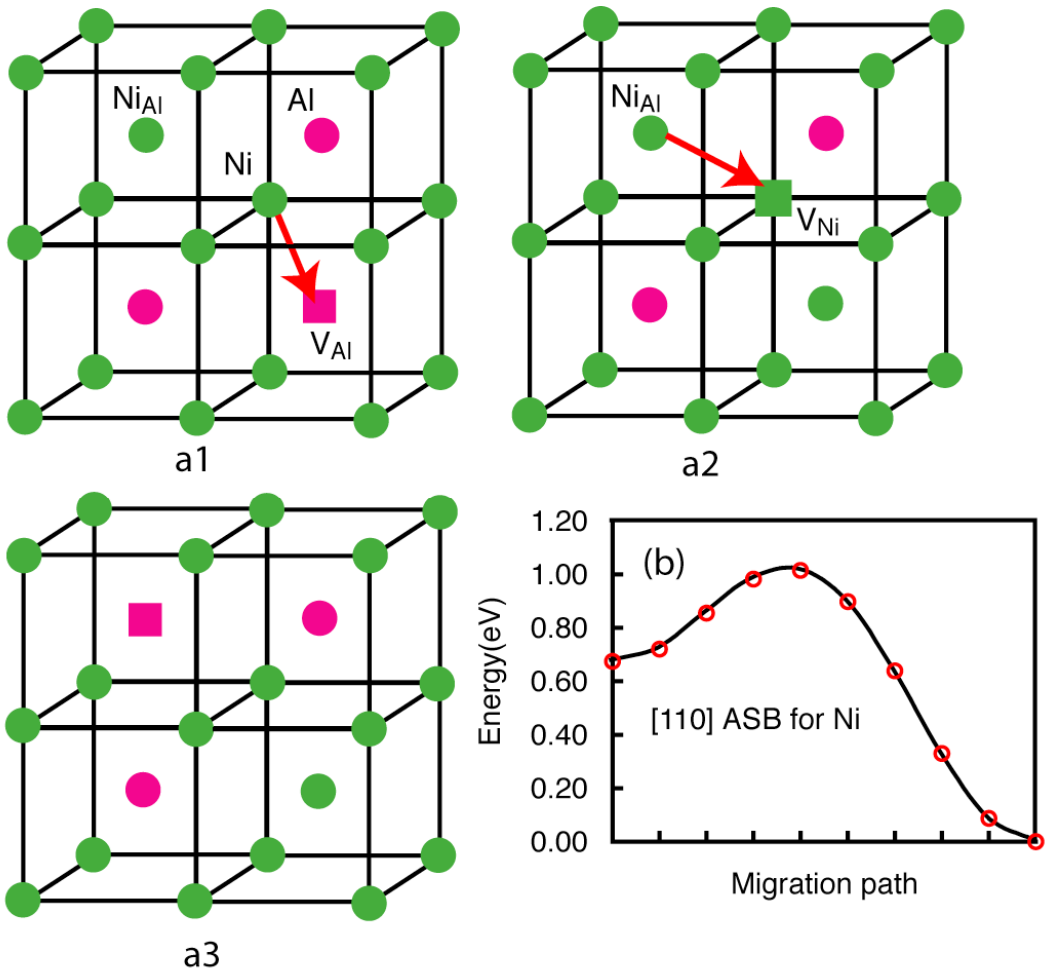

Figure 4-12 (a) The [110] anti-structural-bridge migration sequence for Ni atoms in B2-NiAl, and (b) The calculated variation of the energy along the [110] anti-structural-bridge migration paths for Ni atoms in B2-NiAl. The energy is relative to the configuration (a2).

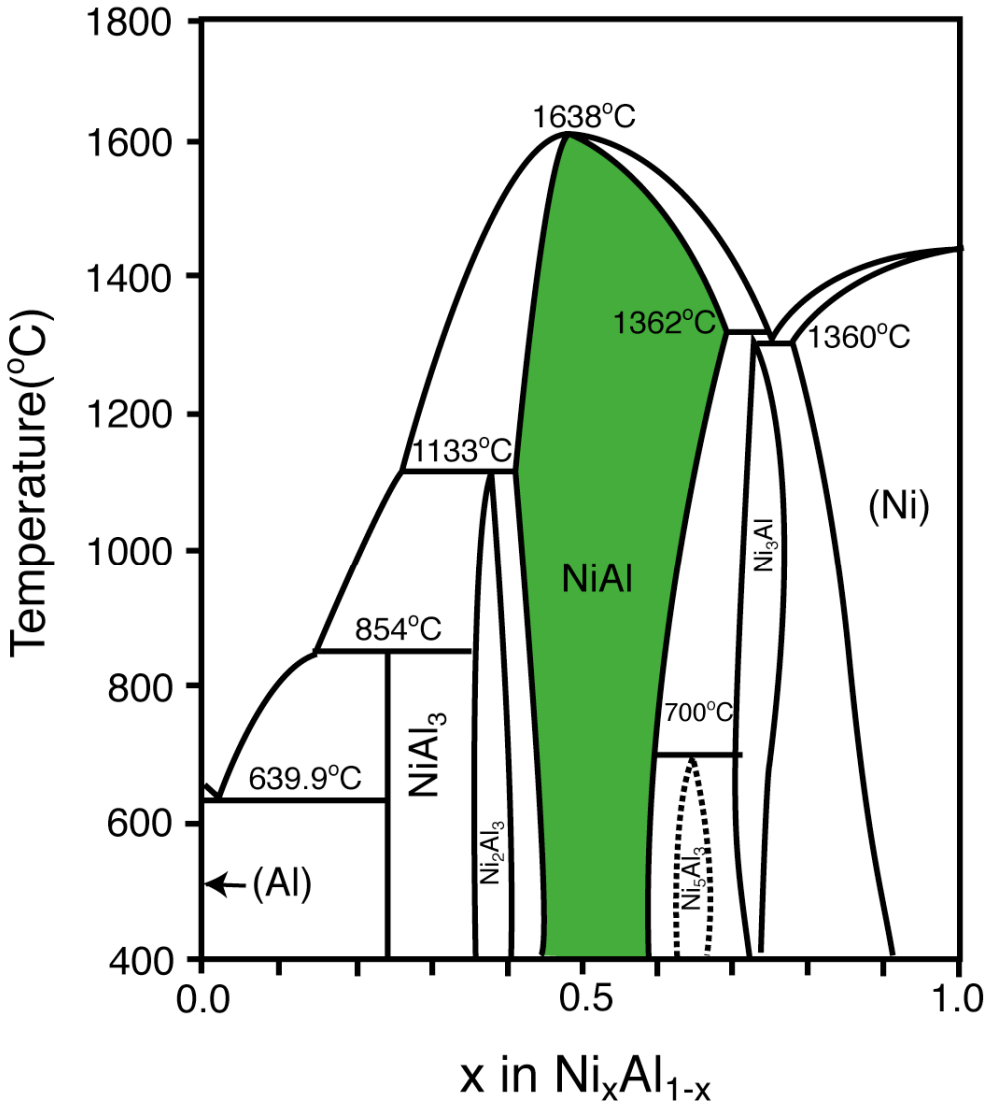

Figure 4-13 The experimental phase diagram of Ni-Al system (see Ref. 131).

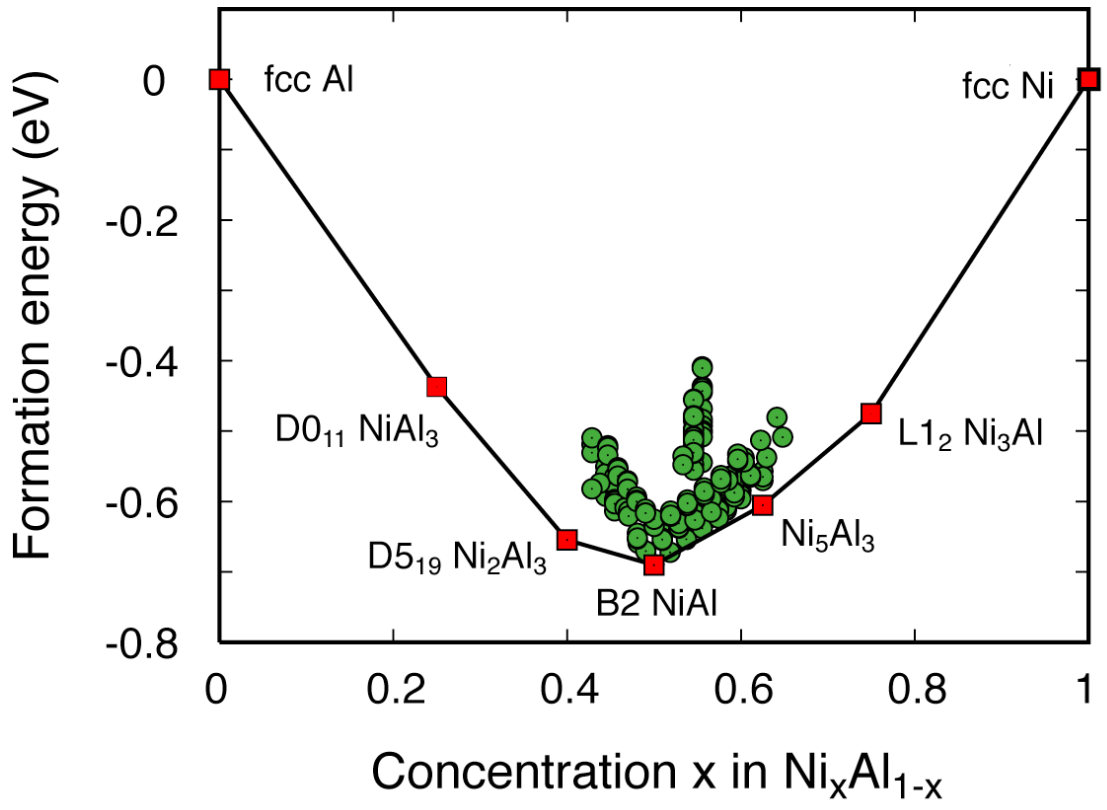

Figure 4-14 Formaiton energies (relative to fcc Ni and fcc Al) of various Ni-Al-vacancy arrangements in B2-NiAl based compound (green circles). Also shown are formation energies of experimentally observed compounds in the Ni-Al system.

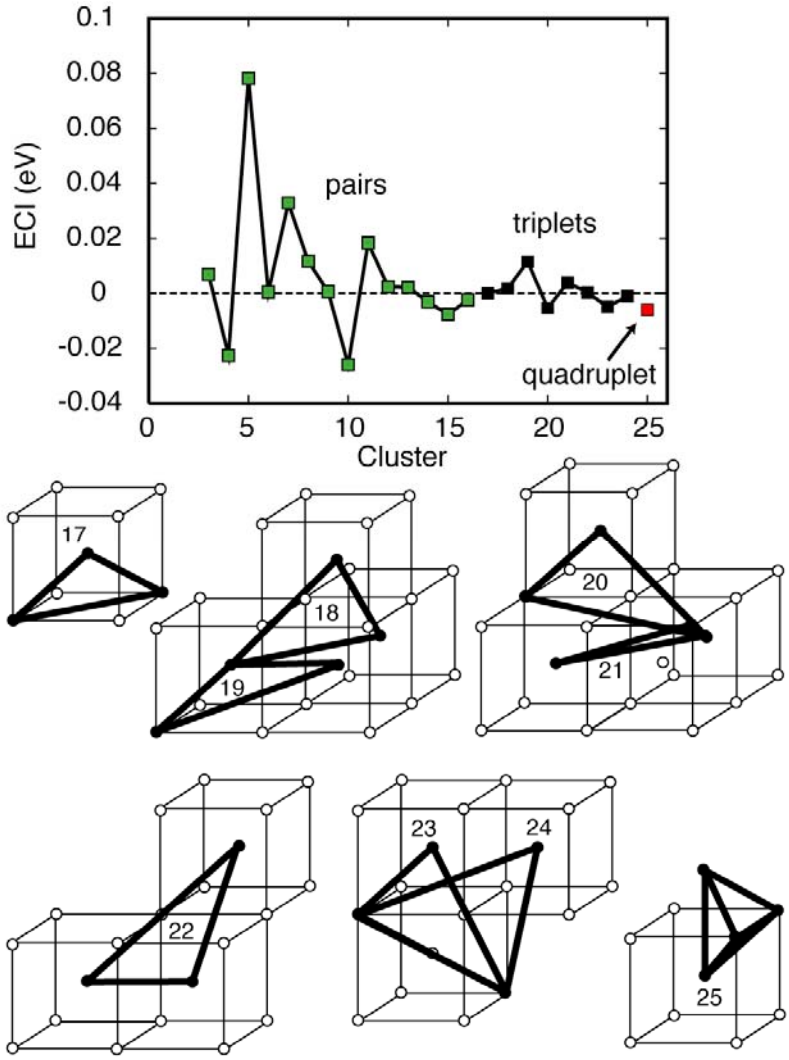

Figure 4-15 Effective cluster interactions of the coupled-sublattice cluster expansion describing the configurational energy of the dominant components on the two sublattices of B2-NiAl. The cluster expansion includes 1 empty cluster, 2 points (for the Al and Ni sublattice sites), [not shown in the figure], 14 pairs, 8 triplets and 1 quadruplet.

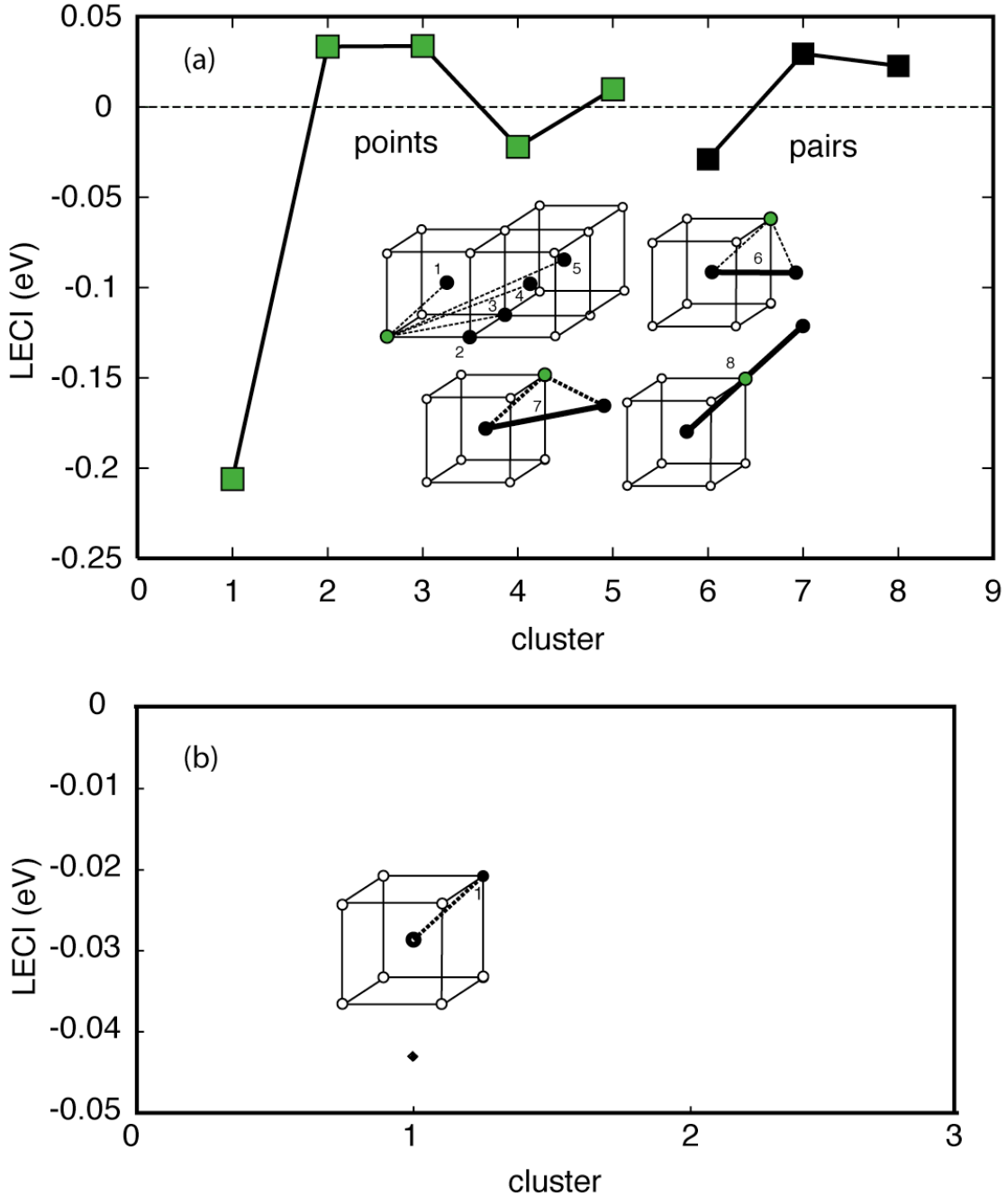

Figure 4-16 Effective cluster interactions for local cluster expansion for (a) anti-site Al, including the empty cluster (not shown in the figure) along with 5 point and 3 pair clusters, and (b) Al vacancy, including the empty cluster (not shown in the figure) and one point cluster.

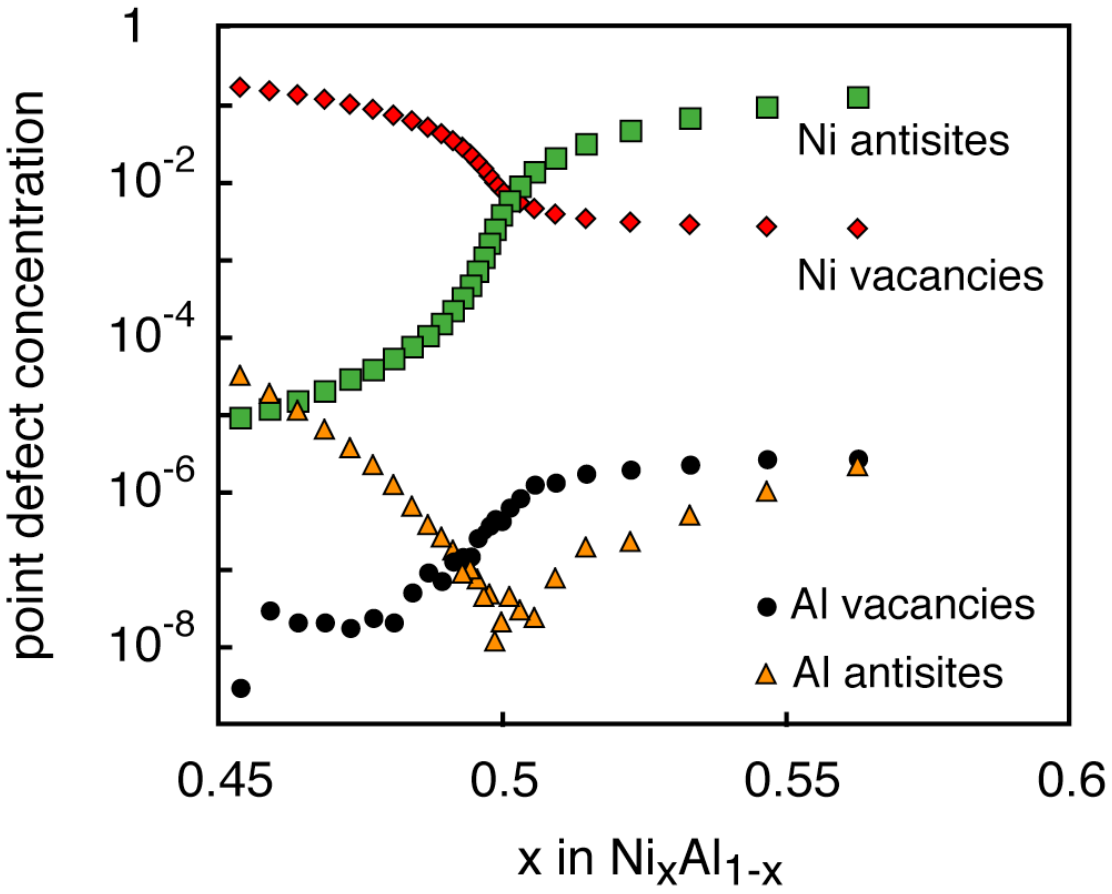

Figure 4-17 Calculated equilibrium point defect concentrations (per sublattice site) in B2-NiAl as a function of composition at 1300K. Green squares are the Ni antisite concentrations, red diamonds are Ni-vacancy concentrations, filled circles are Al vacancies and yellow triangles are Al antisite concentrations.

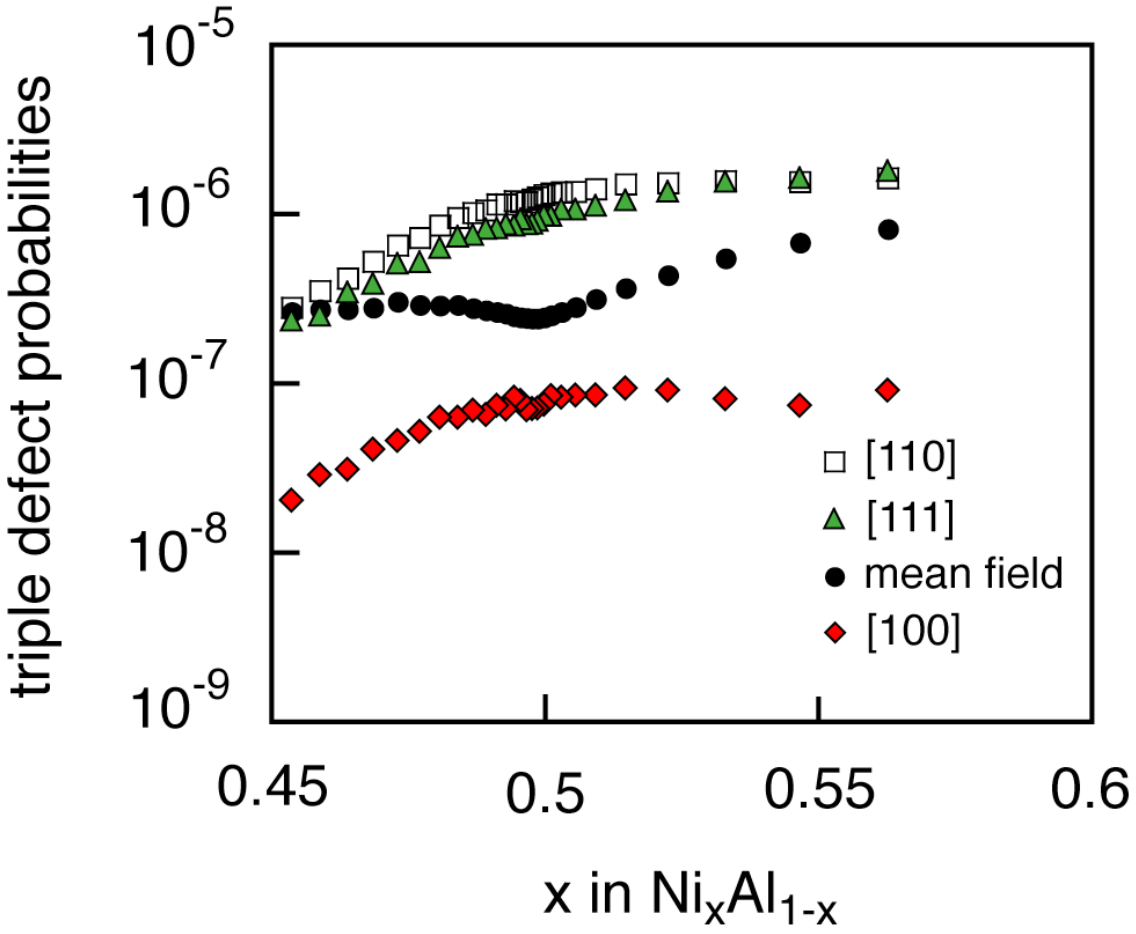

Figure 4-18 Calculated equilibrium triple-defect probabilities as a function of composition in B2-NiAl compound at 1300K.

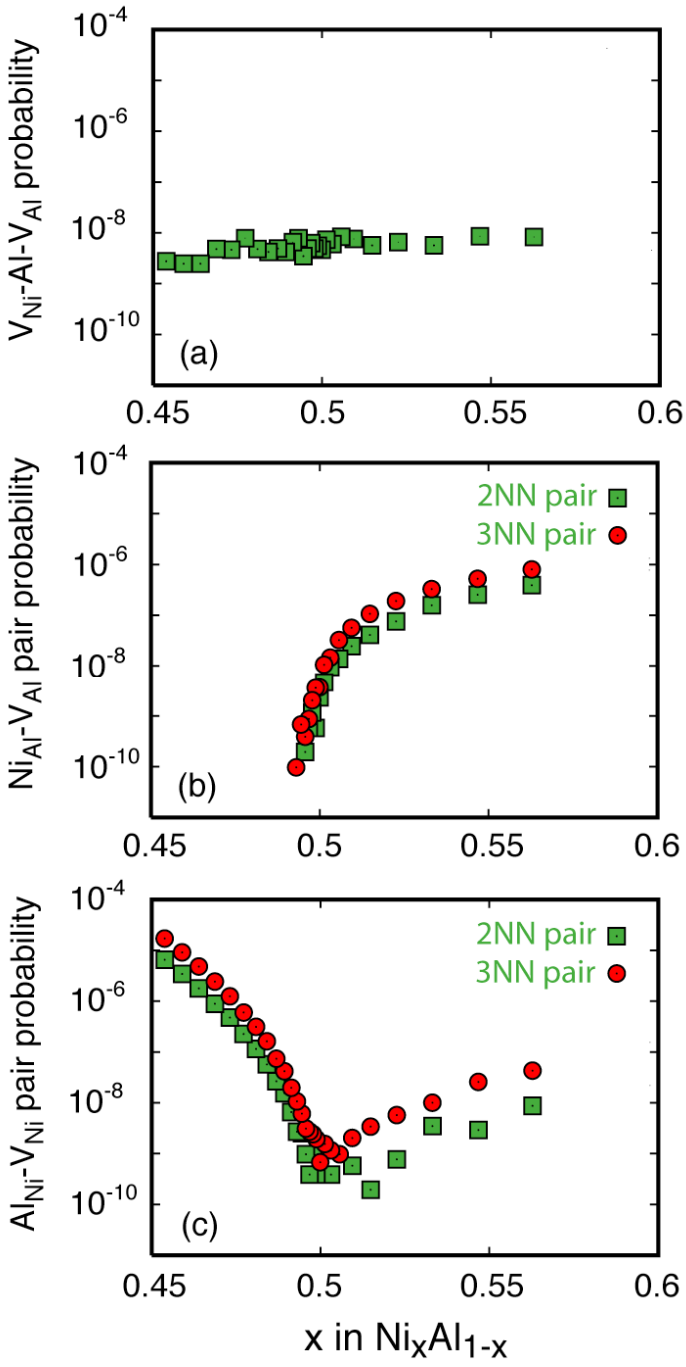

Figure 4-19 Calculated equilibrium defect complex probabilities as a function of composition in B2-NiAl compound at 1300K. (a) Intermediate state of the triple defect migration mechanism consisting of a V_{Ni}-Al_{Al}-V_{Al} cluster, (b) Al_{Ni}-V_{Ni} second nearest neighbor pair and third nearest neighbor pair, (c) Ni_{Al}-V_{Al} second nearest neighbor pair and third nearest neighbor pair.

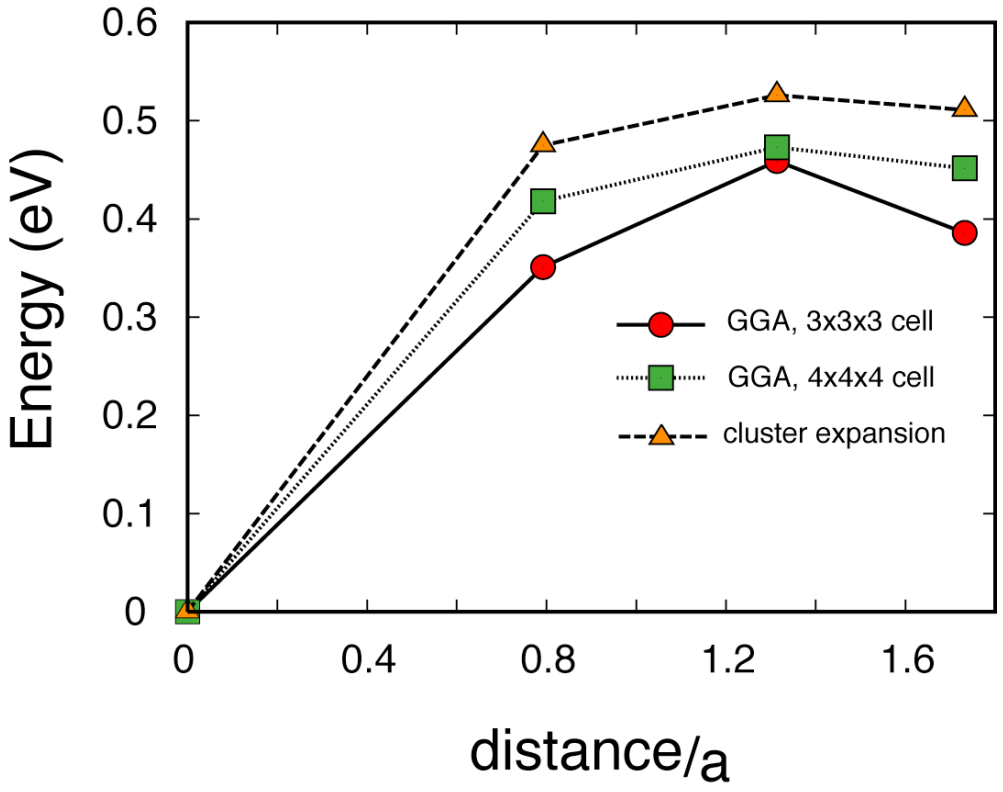

Figure 4-20 Calculated energy as a function of distance between an antisite Ni and an antisite Al. The energy is relative to that of the configuration with a nearest $Ni_{Al} - Al_{Ni}$ pair and the distance is relative to the nearest pair distance, a is the lattice parameter.

Chapter 5

Tracer diffusion and diffusion mechanisms in B2-NiAl compound

In chapter 4, we investigated the migration barriers for various diffusion paths and the point defect complexes that are important to mediate these hops in B2-NiAl compound. Based on these information we will further investigate the tracer diffusion and relative importance of various diffusion mechanism for B2-NiAl compound from first-principles in this chapter.

Diffusion in alloys can be a complex kinetic process that depends on the nature of intrinsic point defects, the energy barriers of different hop mechanisms and the degree of short and long-range order among the constituents of the alloy. B2-NiAl, in spite of its simple CsCl crystal structure, epitomizes this complexity. While many hop mechanisms and intricate hop cycles have been proposed, no comprehensive picture of the dominant atomic transport mechanisms in B2-NiAl has been established. Here we perform a first-principles study of diffusion in B2-NiAl, simultaneously considering all relevant hop mechanisms. The approach couples a first-principles cluster expansion description of the configurational energy with kinetic Monte Carlo simulations to predict tracer diffusion coefficients in B2-NiAl and rigorously accounts for the equilibrium degree of short-range order among point defects as a function of alloy concentration. We find that the dominant transport mechanisms are very sensitive to the bulk alloy concentration.

5.1 Simple structure and complicated diffusion mechanisms

Diffusion in typical metallic alloys is mediated by a dilute concentration of vacancies that stochastically wander through the crystal, in the process rearranging the various components of the alloy. B2-NiAl, however, is an ordered compound, deviating far from thermodynamic ideality and exhibiting an unusually high concentration of vacancies. In fact, the high vacancy concentration on the Ni-sublattice of Al-rich B2-NiAl is reminiscent of intercalation compounds used as electrodes in Li-ion batteries, whereby Li can fill interstitial sites of a crystalline host during discharge of the battery. Li diffusion in these compounds occurs in the non-dilute regime by exchanging with neighboring vacant interstitial sites and is restricted to exchanges on the same sublattice. Although Ni second nearest neighbor hops restrict Ni diffusion to the Ni-sublattice, several viable hop-cycles proposed in past decades involve exchanges between Al and Ni of the two sublattices. Furthermore, experiment indicates that Al mobility is also sizable in B2 NiAl in spite of the fact that the concentration of vacancies on the Al sublattice is very low. Diffusion in B2-NiAl, is therefore quite distinct from what is known to occur in metallic solid solutions and in more complex systems such as intercalation compounds.

The NiAl intermetallic compound has B2 structure shown in the Fig. 2-1. This is a very simple structure with Al atom at the center and Ni atom at the corner of a cubic cell. Even in a system with such a simple structure, the diffusion process could be very complicated due to the complex defects. As we have mentioned in chapter 4 compared to other compounds in Ni-Al system, which cannot sustain large off-stoichiometry, the B2 NiAl compound can accommodate large off-stoichiometry at finite temperature because it can contain high concentration of point defects. The well-known point defects in this compound are Ni vacancies (vacancy at Ni sublattice, denoted by V_{Ni}), anti-site Ni (Ni atom at Al sublattice, denoted by Ni_{Al}), Al vacancies (vacancy at Al sublattice, denoted by V_{Al}) and anti-site Al (Al atom at Ni sublattice, denoted by

Al_{Ni}). The calculated equilibrium concentrations of these point defects at 1300K are shown in Fig. 4-17. Consistent with experiment results [41,134] Figure 4-17 shows that antisite Ni and Ni vacancies are dominant point defects in Ni-rich side and Al-rich side respectively, while antisite Al and Al vacancy are minor point defects. From Figure 4-17 we can see how complicated point defects could be in a multi-component compound with nevertheless simple structure such as B2 NiAl. First, several types of point defects could be present simultaneously. Second, the defect concentrations could depend on the bulk composition of the compound instead of being constant. Finally, the concentration of vacancies could be non-dilute. For example, the Ni vacancy concentration in B2 NiAl could be as high as around 15% in Al-rich side. The complex point defects in real material systems make the diffusion process complicated and make the classic assumptions such as dilute and uniform vacancy concentration invalid. These point defects can also form various defect clusters such as triple-defects, Al anti-site clusters and Ni anti-site clusters shown in the Fig. 4-6 to Fig. 4-10, which makes the situation more complicated.

Over the past several decades, many diffusion mechanisms have been proposed through experimental and theoretical researches, however, no consensus has been reached as to the dominant hop mechanisms responsible for atomic transport in B2 NiAl. One impediment to achieving a fundamental understanding of diffusion in this compound is the fact that no Al isotopes are readily available, preventing a direct measurement of Al tracer diffusion coefficients in B2-NiAl. In chapter 4, we have investigated the migration barriers for the nearest neighbor (NN) hop, the next nearest neighbor hop (NNN), the six-jump-cycle (6JC) sequence [47,63,66], the triple-defect (TD) sequence [49,67], and the anti-structural bridge (ASB) sequence [52].

Our DFT calculations have shown that Al atom cannot perform nearest-neighbor hops because it will disrupt the order of the configuration and the resulting structure is mechanically

unstable; instead, they do two-atom collective hops. For example, for the anti-structural-bridge hop for Al demonstrated in Fig. 4-10, instead of doing two consecutive nearest neighbor hops proposed by previous researchers [52], the Al atoms actually perform a two-atom simultaneous hop. For the triple-defect sequence, DFT computation by us and other researchers shows that it is a three-step sequence [129] instead of four-step sequence proposed by S. Frank et al [49]. The first and third sub-hops of triple-defect hops involve Ni atom hopping into the nearest neighbor vacancy, while the second sub-hop involves Al atom hopping into the second nearest neighbor vacancy (Fig. 4-6) instead of two consecutive nearest-neighbor hops. For the six-jump-cycle sequence, the DFT computations by us and previous researchers shows that instead of involving six consecutive nearest neighbor hops, it does three two-atom simultaneous hops (Fig. 4-3)[58,129].

While the classic treatment in diffusion simulation makes assumption that only single atom nearest neighbor hops and second nearest neighbor hops are allowed, B2-NiAl compound exhibits more diffusion paths other than nearest neighbor and next nearest neighbor hops. It is not surprising that many other real materials, which have more complex structures than B2 structure, could have much more complicated diffusion paths than sequence of single atom nearest neighbor and second nearest neighbor hops. Due to the complexity of the diffusion paths in B2 NiAl compound, no one has ever systematically investigated and incorporated all these diffusion paths mentioned above in a kinetic Monte Carlo simulation. In this thesis, we will simultaneously incorporate the most important hop mechanisms of B2-NiAl within a kinetic Monte Carlo framework and predict tracer diffusion coefficients from first principles.

5.2 Tracer diffusion in B2-NiAl compound

To thoroughly investigate the diffusion in multi-component solids with significant configurational disorder as exhibited by B2-NiAl from first-principle, we use cluster expansion techniques described in section 2.3 combined with grand canonical Monte Carlo and kinetic Monte Carlo simulations described in section 2.4. Compared to the mean field techniques that neglect the interactions among various defects and atoms [42-44], the cluster expansion of the configurational energy can rigorously account for interactions among defects through an accurate description of the energy of the compound as a function of the arrangement of Ni, Al and vacancies over the two cubic sublattices. As common prerequisite steps for both grand canonical or kinetic Monte Carlo simulations, the energies of a number of various Ni-Al-vacancy configurations were firstly calculated from first-principle, then, these energies were used to fit a cluster expansion (see chapter 4). Finally, the first-principles parameterized cluster expansions can be used in grand canonical Monte Carlo and kinetic Monte Carlo simulations to predict finite temperature thermodynamic properties and kinetic properties, such as tracer diffusion coefficients.

In section 2.4 we have described the kinetic Monte Carlo framework and here we will recall some key points of our kinetic Monte Carlo simulation procedure. The KMC algorithm is based on the n-fold way method in which each hop is picked with the possibility Γ_i / Γ_{tot}, where Γ_i is the migration frequency of hop i and Γ_{tot} is the sum of all individual probabilities Γ_i. [109] The time is updated after each hop by $-\ln\rho/\Gamma_{tot}$, where ρ is a random number between (0,1] [109]. For each Ni vacancy, there are 86 possible hops and for each Al vacancy there are 38 possible hops. For a specific hop, we calculated the migration probability Γ within the harmonic transition state theory with local harmonic approximation [110], which gives $\Gamma = \nu_0 \exp(-E_m / kT)$, where ν_0 is a vibration prefactor, E_m is the activation energy required to move the hopping

atom(s) from the initial stable state to the activated state, k is Boltzmann's constant and T is the absolute temperature in degrees Kelvin. The attempt frequency ν_0 for a specific hop is calculated as $\prod_{i=1}^{3N} \nu_i \;/\; \prod_{i=1}^{3N-1} \nu_i^*$, where N is the total number of atoms, the ν_i's are normal mode vibrational frequencies at the stable state and the ν_i^*'s are normal mode vibrational frequencies at the activated state. The numerator in the above expression for ν_0 has one frequency more than the denominator. Instead of calculating normal vibration frequencies for all atoms, we calculate the prefactor within the local harmonic approximation to get an order of magnitude estimate of the prefactor. That is we calculate the normal vibration frequencies for atoms involved in the hop assuming that all other frequencies cancel out. For example, if the hop involves two atoms then the numerator (corresponding to stable state) has 6 real frequencies while the denominator (corresponding to saddle point) has 5 real frequencies and 1 imaginary frequency; if the hop involves one atom then the numerator has 3 real frequencies while the denominator has 2 real frequencies and 1 imaginary frequency. All the calculations for vibrational frequencies of stable state and saddle point of a specific hop are conducted from first-principles by using the VASP software package within a 3x3x3 superecell that contains 27 B2-NiAl cells, i.e., 54 crystal sites. In the calculation, the atoms involved in the hop are displaced in the direction of each Cartesian coordinate, and the Hessian matrix consisting of second derivatives of the energy with respect to atom displacement, is determined from the forces. The eigenvalues of the Hessian matrix are the squares of the normal vibration angular frequencies ω ($\nu = \omega / 2\pi$). If the Hessian matrix has one negative eigenvalue, then the corresponding structure is an activated state [153]. Figure 5-1 shows the calculated attempt frequency ν_0 for various diffusion paths, which shows that there is

no big difference among attempt frequencies for various diffusion paths and all of them are of 10^{12} Hz degree of magnitude.

To account for the environment dependence of the migration barriers, we used an approach described in ref [148], in which a kinetically resolved activation (KRA) barrier is introduced for each hop, defined as an averaged barrier over a back and forth hop. The actual barrier for a particular hop can then be reconstructed by adding the KRA barrier to the average energy of the end states of the hop, calculated with the cluster expansion, minus the energy of the initial state [148]. The KRA barriers are sensitive to any local disorder that may be present. For example, a NNN Al hop has a migration barrier of 1.5 eV, which is reduced to 0.75 eV if the hop occurs in the immediate vicinity of a Ni vacancy. Within our kinetic Monte Carlo simulations we tabulated KRA barriers for each elementary hop and for different local environments (determined by the occupancy in the nearest neighbor shell). This approach ensures that the concentrations of point defects and defect clusters within the kinetic Monte Carlo simulations are representative of those in thermal equilibrium (since the energies of the end states of the hop are calculated with the cluster expansion) and that the effect of any variations in composition and order on hop mechanisms and barriers are accurately accounted for. If important, cyclic hops, which are made up of sequences of elementary hops, will therefore spontaneously occur within the kinetic Monte Carlo simulations.

Having incorporated all possible diffusion hops in B2 NiAl compound, our kinetic Monte Carlo program will calculate the tracer diffusion coefficients for Ni and Al atoms since the tracer diffusion coefficients provides us with the most direct way to understand the physical mechanism under diffusion in multi-component compounds. The tracer diffusion coefficient of specie j is calculated as $\left\langle \left(\sum_{\xi} [\Delta \vec{R}_{\xi}^{j}(t)]^2 \right) \right\rangle$ / $(2d)tN_{\xi}[111]$ at each composition within KMC

simulations by averaging over trajectories, $\Delta\vec{R}_{\xi}^{j}(t)$ (the vector linking the end points of the trajectory of atom ξ of specie j after time t, N_{ξ} is the number of atoms of specie j, and d is the number of dimensions), at different times and over simulations that started from different initial configurations (obtained with canonical Monte Carlo.

A variety of alloy compositions were determined with grand canonical Monte Carlo simulations corresponding to an equilibrium vacancy concentration [93]. In the Ni-rich alloys, the Monte Carlo (MC) cell contained 12^3 B2-NiAl unit cells (3456 sites) and 1000 kMC passes were performed (one kMC pass corresponds to each atom on average having performed a hop), starting from 100 initial configurations. In the Al-rich alloy an MC cell with 44^3 B2-NiAl unit cells (170,368 sites) was used and 60 kMC passes were performed starting from 8 initial configurations. A significantly larger MC cell was required in the Al-rich alloy to obtain the correct equilibrium concentrations for antisite Al atoms, antisite Ni atoms and Al vacancies.

Figure 5-2 illustrates predicted tracer diffusion coefficients for both Ni and Al as a function of bulk alloy concentration (defined as $x_{Ni}/(x_{Ni}+x_{Al})$ where x_i refers to the fraction of bcc sites occupied by specie i) calculated at 1300 K. As is clearly evident from Fig. 5-2(a), the predicted tracer diffusion coefficients depend strongly on composition, exhibiting a minimum at stoichiometric NiAl. In Ni-rich alloys, the Ni tracer diffusion coefficient is larger than that of Al indicating a higher Ni mobility there. In Al-rich alloys, however, the tracer diffusion coefficients of Ni and Al are very similar, in spite of the fact that the Ni sublattice consists of a very high concentration of vacancies. While experimental measurements of Al tracer diffusion coefficients in B2-NiAl are not available, several measurements of Ni tracer diffusion coefficients have been performed [49,50]. The measurements of Hancock et al. [50] and Frank et al. [49] qualitatively exhibit similar trends with alloy composition as predicted here, however, quantitatively differ

from each other by as much as an order of magnitude in Al and Ni rich alloys (see Fig. 5-2b). Both measured an increase in the Ni tracer diffusion coefficient with increasing Ni concentration above stoichiometric NiAl. The Ni tracer diffusion coefficient measured by Hancock et al [50] exhibits a pronounced minimum at stoichiometric NiAl composition, while that measured by Frank [49] remains constant, as the alloy becomes Al rich. We emphasize that our predicted tracer diffusion coefficients are for a perfect crystal without dislocations and grain boundaries, while experimentally measured tracer diffusion coefficients are always performed on samples that will contain some extended defects that can act as short-circuit diffusion paths. The samples of Frank et al [49] were performed on single crystals such that grain boundary diffusion did not play a role in their measurements.

There are several sources of inaccuracies in the calculated tracer diffusion coefficients, which arise from the first-principle calculations, from the cluster expansion and from the kinetic Monte Carlo simulations.

First, there is an error due to the use of the generalized-gradient approximation in density functional theory, which is difficult to quantify and requires experimental information about a particular hop mechanism to enable a direct comparison with a calculated migration barrier.

In DFT calculations the energy cutoff, the *k*-point sampling and the size of the supercell are also sources of inaccuracies. In this thesis, a plane-wave basis set cutoff energy of 500eV was used, which is much higher than the required value for the Ni and Al. Convergence tests of the energy with respect to *k*-point grids indicated that *k*-point sampling errors are less than 5meV per $\mathrm{Ni}_{x_{Ni}}\mathrm{Al}_{x_{Al}}\varnothing_{x_V}$ formula unit, where $\varnothing$ stands for a vacancy. In section 4.3 we have shown that the estimated numerical error in calculated activation barriers due to the supercell size is of the order of 100-200meV.

In addition to the errors arising from first-principle calculations, an error can also come from the cluster expansion. We have checked the difference in activation energy between first-principles calculation and cluster expansion prediction for some of hops and found an error of the order of 40meV.

Finally, kinetic Monte Carlo will also introduce inaccuracies due to the averaging over a finite number of atomic trajectories. From Fig. 5-2 illustrates scatters in the calculated tracer diffusion coefficients. This scatter comes from kinetic Monte Carlo simulations and is of the order of a factor of 2.5. The scatter will decrease if averaging were performed aver more kinetic Monte Carlo runs starting from different initial states. However, to do this is not feasible based on our calculation capacity.

Although there are many types of numerical errors in the calculated migration barriers, they are unlikely to be completely correlated in a positive sense. Some error cancellation can be expected. Furthermore, systematic errors in the calculated activation barrier of 150meV will produce an error of factor three in the diffusion coefficient at 1300K since hopping rates depend exponentially on the activation barrier. This error in tracer diffusion coefficient is comparable to the magnitude of the scatter in calculated results from kinetic Monte Carlo and within the scatter in the experimental results. Furthermore, because these are systematic errors, they will not change the trend of the tracer diffusion coefficients over the bulk composition range.

5.3 Relative importance of various diffusion mechanisms in B2-NiAl compound

A unique advantage of the kinetic Monte Carlo simulations is that it allows us to track the frequency with which the various hops occur as a function of alloy composition, thereby providing insight about the dominant diffusion mechanisms responsible for atomic transport in

B2-NiAl. These relative frequencies are illustrated in Figure 5-3. It should be noted that the fractions for the cyclic hop mechanisms (i.e. 6JC, triple-defect) and hop sequences plotted in Fig. 5-3 do not correspond to the frequency with which the sequence itself occurs, but rather to the sum of the total number of sub-hops making up the sequence. Furthermore the plotted frequencies are upper bounds for the various hop sequences, as not all hop sequences come to completion, retracing steps before reaching the end of a sequence.

Around stoichiometry, the most frequent hop sequence is Ni-anti-site/Ni-vacancy back and forth hops, due to its relatively low migration barrier (~0.7 eV averaged over the back and forth hop directions [93]). These hops, however, do not contribute to macroscopic transport (and therefore the tracer diffusion coefficient) since a back and forth hop restores the Ni atom to its initial position. The next most frequent hop mechanism at stoichiometry is the triple-defect hop sequence in which a Ni anti-site next to a pair of Ni-vacancies perform a sequence of three hops that results in a net migration of the triple defect by a cubic lattice parameter. As the Ni concentration of the alloy is increased above stoichiometry, the dominant hop mechanism changes to the anti-structure-bridge (ASB) mechanism [52], whereby vacancies, which energetically prefer the Ni-sublattice, can migrate along percolating networks of nearest neighbor Ni-chains connected by Ni-anti-site atoms. Since the existence of the percolating networks requires Ni-anti-site atoms, the ASB sequence is only viable in Ni-rich alloys where off-stoichiometry is accommodated by Ni-anti-site atoms [52]. The average migration barrier for Ni-NN hops is comparatively low (~0.7 eV) and the migration of a vacancy along a percolating network of Ni-anti-site atoms does not result in any increased disorder, thereby making the ASB sequence a very effective mechanism to transport Ni ions. As a result, while Al predominantly migrates by means of the triple-defect mechanism, the Ni atoms can migrate via both the triple-

defect and the ASB mechanisms resulting in a Ni tracer diffusion coefficient exceeding that of Al above a threshold composition upon which the percolating NN Ni-pairs consisting of Ni anti-site atoms are formed.

In Al-rich alloys (only one concentration was considered in Al-rich B2-NiAl as very large Monte Carlo cells are required to ensure that equilibrium concentration for Al antisite, Ni antisite and Al vacancies present), the dominant diffusion mechanisms change again, with the triple-defect mechanism becoming less important and the ASB sequence involving Ni no longer viable. Instead Ni and Al transport is mediated by the 6JC (which as described above is in fact a sequence of three pair-atom hops) and what we will refer to as the Al-ASB sequence. The 6JC, while having high migration barriers for the first hop (above 2.3 eV) [93,58,129], become a dominant mechanism in Al-rich alloys due to the large concentration of Ni-vacancies. Its high frequency has an entropic origin since for a given Ni-vacancy there are 48 symmetrically equivalent pair-atom hops that can initiate the 6JC sequence. An important result in Fig. 5-3 is that Ni NNN hops are not significant at any composition, even in Al-rich alloys where the Ni vacancy concentration is very high, in large part due to its high migration barrier (~2.7eV) and since only six NNN hops are possible for a Ni vacancy.

The other dominant diffusion mechanism in Al-rich alloys involves pair-atom hops in which an Al on the Al sublattice and an anti-site Al simultaneously hop into a Ni vacancy. This hop mechanism, which is characterized by a low migration barrier (~1 eV) [93], can be compared to the Ni-ASB mechanism in that Al transport by this mechanism is greatly enhanced once a percolating network of Ni vacancies is established. We, therefore, refer to it as an Al ASB mechanism. While the kinetic Monte Carlo simulations predict a high frequency for this mechanism, the alloy composition is likely not Al-rich enough to result in a sufficiently high Ni-

vacancy concentration to form percolating networks [149]. Most of the pair-atom hops involving two Al atoms are therefore back and forth hops and do not contribute much to macroscopic Al transport. Hence at the Al-rich composition considered here, the Ni and Al tracer diffusion coefficients are similar in magnitude, relying for the most part on the 6JC mechanism for long-range transport [63].

5.4 Summary

In this chapter we have shown the technique and complexity of investigating diffusion mechanisms and predicting diffusion coefficients in a real material system – B2 NiAl compound. Combining diffusion theory, cluster expansion and kinetic Monte Carlo simulation, we systematically investigated various diffusion mechanisms and the calculated tracer diffusion coefficients for Ni and Al are in good agreement with the experiment results. For the first time, the relevant importance of various diffusion mechanisms is revealed in B2 NiAl. The above results clearly demonstrate a remarkable complexity of atomic diffusion in metallic alloys even for compounds such as B2-NiAl with its simple crystal structure. The decomposition of atomic transport into various hop mechanisms, as illustrated in Fig. 5-3, shows the tremendous sensitivity of the dominant diffusion mechanism to small changes in bulk alloy concentration. This understanding is not only intriguing from a scientific point of view, but is also of great relevance from an engineering standpoint as strategies to alter diffusion behavior in B2-NiAl through alloying will depend sensitively on composition. A ternary alloying addition that may, for example, have a tendency to pin down triple defects will only suppress diffusion in stoichiometric alloys, but will be less effective in diminishing transport in Ni-rich alloys where diffusion is dominated by the ASB-Ni mechanism. This has important implications in graded

multi-layer structures such as bond coats on turbine blades where interdiffusion can result in a change of the alloy composition. The approach used here, combining first-principles cluster expansion techniques with kinetic Monte Carlo simulations, will enable the study of diffusion in other complex alloys, oxides and semiconductors, unraveling unexpected atomic transport mechanisms that arise from varying degrees of short and long-range order at non-dilute concentrations.

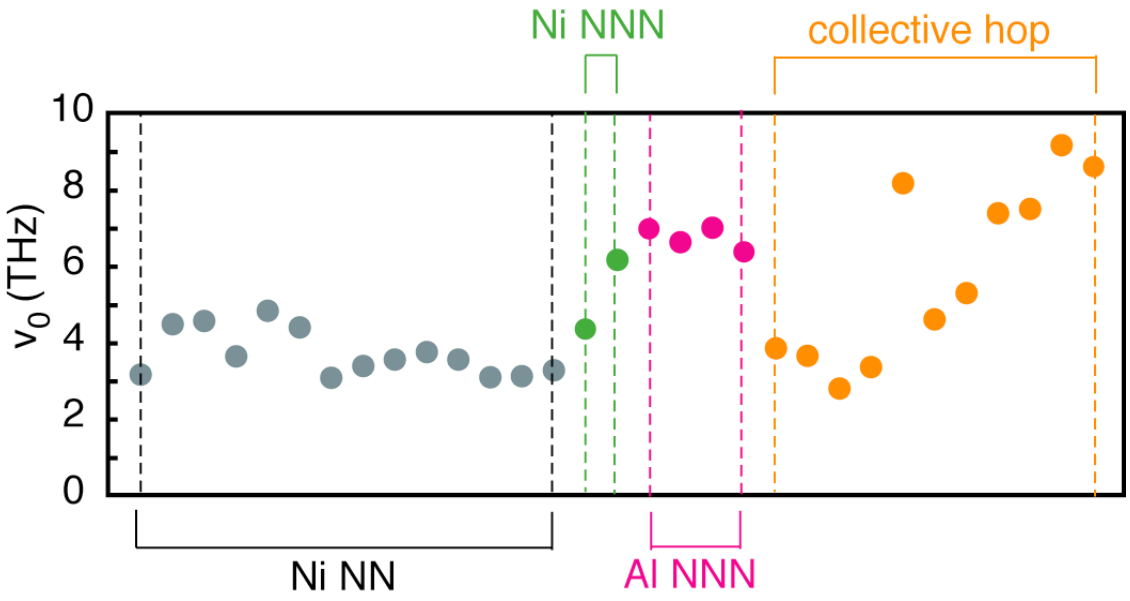

Figure 5-1 Calculated attempt frequencies for various diffusion hops in B2-NiAl compound.

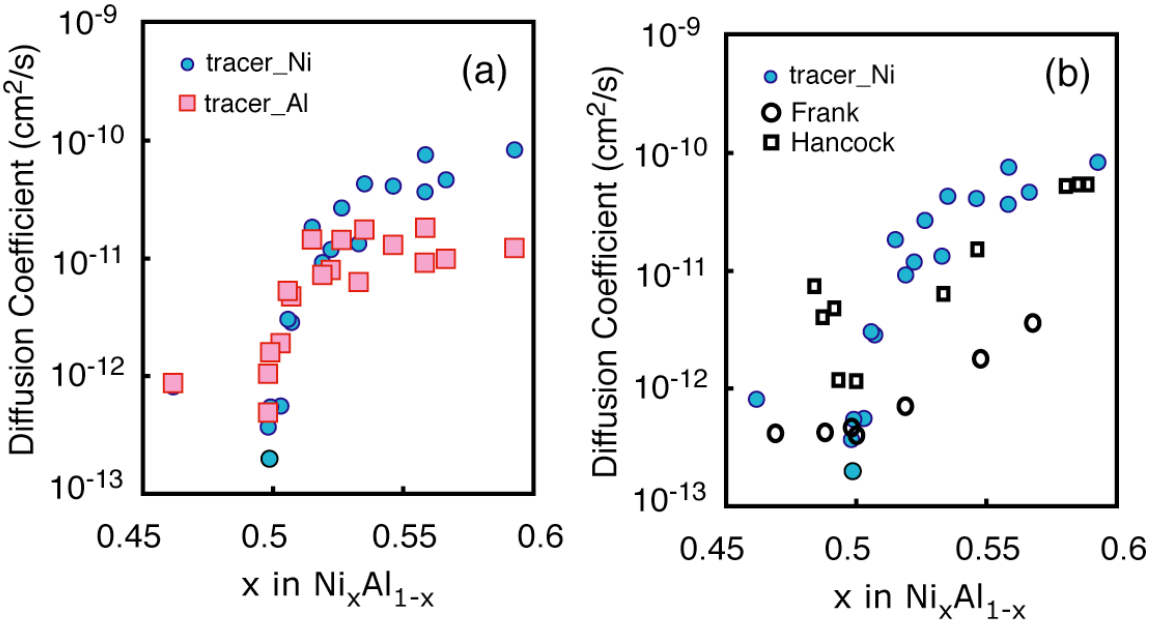

Figure 5-2 (a) Calculated tracer diffusion coefficients for Ni and Al at 1300K. Solid blue circles are Ni tracer diffusion coefficients and solid red squares are Al tracer diffusion coefficients. (b) Comparison of calculated Ni tracer diffusion coefficient (blue circles) at 1300K with experimental measurements of Ni tracer diffusion coefficients by Frank et al. (at 1300K, white circle) [49] and Hancock et al. (at ~1273K, white square) [50].

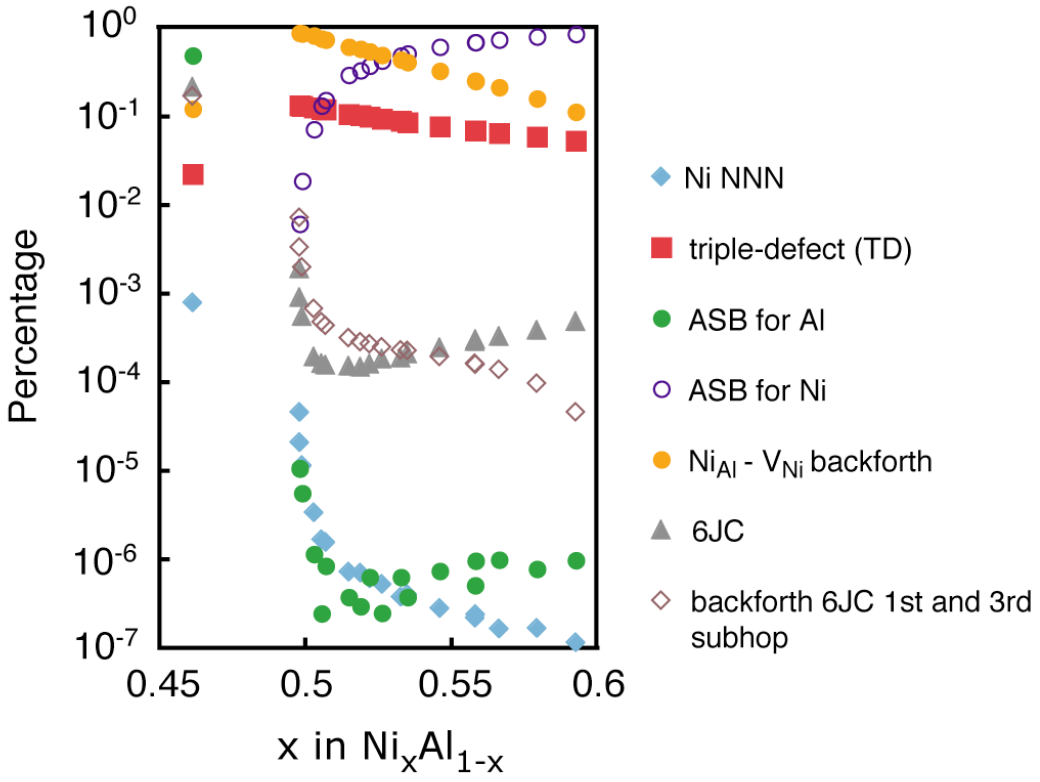

Figure 5-3 Calculated relative percentages of various diffusion hops in B2 NiAl compound as a function of composition at 1300K. Solid blue diamonds are percentages of Ni next-nearest-neighbor (NNN) hops; solid red squares are percentages of triple-defect (TD) hops; solid gray triangles are percentages of six-jump-cycle (6jc) hops; solid green circles are percentages of anti-bridge-structure hops for Al (ASB_Al); purple circles are percentages of anti-bridge-structure hops for Ni (ASB_Ni) and solid orange circles are percentages of back-and-forth hops involving Ni antisite (Ni_{Al}) and Ni vacancy (V_{Ni}). Brown diamonds are for back forth 6JC 1st and 3rd sub hops.

Chapter 6

Self-diffusion and interdiffusion in B2-NiAl compound

In chapter 5, we investigated the tracer diffusion coefficients for Ni and Al atoms in B2-NiAl compound. Based on the results we obtained from chapter 5, in this chapter we will further investigate self-diffusion and interdiffusion in the B2-NiAl compound at high temperature. Going beyond the mean field approximation, we investigated the system with a cluster expansion model to capture interactions among various defects. All well-known diffusion mechanisms and new mechanisms discovered from first principles were incorporated in the kinetic Monte Carlo simulation.

In this chapter we also investigate the thermodynamic factors in B2-NiAl compound and show that in Al-rich alloys the thermodynamic factor of Al is much greater than that of Ni while in Ni-rich alloys they are similar. This difference in thermodynamic factors results in a much higher self-diffusion coefficient of Al compared to that of Ni in Al-rich alloys given similar kinetic factors calculated in this region. This difference also results in two different interdiffusion coefficients depending on whether Ni or Al concentration gradient is used in Fick's first law. We will demonstrate that this difference in thermodynamic factors has its root in the specific characteristic of defects in B2 NiAl, i.e., the high vacancy concentration and asymmetric distribution of vacancies, between the Ni sublattice and Al sublattice.

6.1 Violation of one thermodynamic factor assumption

Interdiffusion is a very important phenomenon in solids and attracts attentions from both application area and theoretical research. For instance, as we have mentioned in chapter 1, the interdiffusion can lead to functional degradation in B2-NiAl compound, which serves as a bond coat between the Ni-rich superalloy substrate and the Al-rich TGO chemical barrier in gas turbine blades [38]. Although the crystal structure of B2-NiAl compound is simple, this compound has very complex defect type and structure [41], making it challenging to investigate interdiffusion in this system. There are many types of point defects and defect clusters that simultaneously exist in the B2-NiAl compound at finite temperature and the interaction among them cannot be simply ignored.

Due to the complex defects in B2-NiAl compound, the diffusion mechanism is not clear although many diffusion mechanisms have been proposed in last several decades [42,43,47-67], including nearest neighbor hop, next nearest neighbor hop, six-jump-cycle hop [47,63,66], anti-structural-bridge hop [52] and triple defect hop [49,67]. In chapter 5, we evaluated all these possible mechanisms as well as new mechanisms and our kinetic Monte Carlo simulations showed that Ni anti-structural bridge hop is the dominant hop in Ni-rich region and Al anti-structural hop is the dominant one in Al-rich region. Despite this clear understanding of diffusion hops in B2-NiAl compound, the effect of specific defect characteristic on the self-diffusion and interdiffusion coefficients of B2-NiAl at high temperature is not clear because the self-diffusion and interdiffusion coefficients depend on not only kinetic factors but also thermodynamic factors [135].

In previous analyses of self-diffusion and interdiffusion in most solids, equations derived within the assumption of a small vacancy concentration have always been used, which leads to a

single thermodynamic factor for both Ni and Al. This assumption is not appropriate for B2-NiAl compound because (i) the vacancy concentration can be as high as 15% in Al rich region; (ii) vacancies do not randomly distributed among the Ni sublattice and Al sublattice (most vacancies are on the Ni sublattice) and (iii) the concentration of vacancy depends on the bulk concentration of the compound [41-43]. All these specific characteristic of defects in B2-NiAl compound invalidate the conventional assumptions concerning vacancies and thermodynamic factors and have significant effects on self-diffusion and interdiffusion coefficients in B2-NiAl compound.

Some researchers have questioned this conventional assumption when studying chemical diffusion in alloys that have high vacancy concentration. For instance, using an model Ising binary ordered alloy Qin [136] argued from computer simulation that whenever the vacancy concentration is greater than 1%, the thermodynamic factors for chemical diffusion of the component A and B are different. Without knowing the vacancy concentration as a function of alloy composition, Bencze [137] roughly evaluated two different thermodynamic factors for Ni and Al in B2-NiAl compound from activity measurements while he admitted that there are problems in obtaining the thermodynamic factors from activity measurements in B2-NiAl compound due to the high vacancy concentration and the absence of the vacancy concentration profile as a function of bulk alloy composition. Thus, we will abandon the conventional assumption regarding vacancy concentration and thermodynamic factor in the present thesis and investigate the effect of specific defect characteristic on the intrinsic diffusion and interdiffusion in B2-NiAl compound from first-principle taking account of the defect concentration as a function of bulk alloy composition.

6.2. Self-diffusion coefficients in B2-NiAl compound

In a system such as B2-NiAl where the crystal sites are conserved, the atomic fluxes for substitutional diffusion mediated by vacancies can be written as the following phenomenological equations [138,139]:

$$J_{Ni} = -L_{NiNi}\nabla\mu_{Ni} - L_{NiAl}\nabla\mu_{Al} - L_{NiV}\nabla\mu_{V} \quad (6\text{-}1a)$$

$$J_{Al} = -L_{AlNii}\nabla\mu_{Ni} - L_{AlAl}\nabla\mu_{Al} - L_{AlV}\nabla\mu_{V} \quad (6\text{-}1b)$$

where J_i(i = Ni, Al or vacancy) is the fluxes of component i that is defined as the number of atoms crossing a unit area per unit time, L_{ij}'s are kinetic coefficients and $\nabla\mu_i$(i = Ni, Al or vacancy) is the chemical potential gradient of component i, As we have mentioned in section 2.4 that we take μ_V= 0 in our simulation since a vacancy is a non-conserved species in a fully equilibrated solid, its chemical potential μ_V must be zero, equations (6-1a) and (6-1b) becomes

$$J_{Ni} = -L_{NiNi}\nabla\mu_{Ni} - L_{NiAl}\nabla\mu_{Al} \quad (6\text{-}2a)$$

$$J_{Al} = -L_{AlNii}\nabla\mu_{Ni} - L_{AlAl}\nabla\mu_{Al} \quad (6\text{-}2b)$$

The atomic fluxes can also be expressed as the following equations according to Fick's first law within the assumption that μ_V = 0 (μ_V is the chemical potential of vacancy, see Chapter 4 for explaination):

$$J_{Ni} = -D_{Ni}\nabla C_{Ni} \quad (6\text{-}3a)$$

$$J_{Al} = -D_{Al}\nabla C_{Al} \quad (6\text{-}3b)$$

where D_i (i=Ni, Al or vacancy) is the self-diffusion coefficient and ∇C_i (i =Ni, Al or vacancy and $C_{Ni} + C_{Al} + C_V = 1$) is the gradient of volume based concentration of component i. The volume-based concentration can be converted to crystal site based concentration according

$$x_i = C_i\Omega, \quad (6\text{-}4)$$

where Ω is the volume per crystal site and x_i is the site based concentration of component i (i=Ni, Al or vacancy) defined as the number of sites occupied by component i as a fraction of total

crystal sites M, that is $x_i = N_i/M$, where N_i is the number of sites occupied by component i and M is the total number of crystal sites. It should be noted that $x_{Ni} + x_{Al} + x_V = 1$. The concentration and chemical potential of Ni, Al and vacancy V satisfy the Gibbs-Duhem relation, namely, $x_{Ni}d\mu_{Ni} + x_{Al}d\mu_{Al} + x_V d\mu_V = 0$. Since μ_V=0, the relation becomes

$$x_{Ni}d\mu_{Ni} + x_{Al}d\mu_{Al} = 0 \tag{6-5}$$

Combining equations (6-2) through (6-5) we can get the following well-known equations for self-diffusion coefficients [135,138]:

$$D_{Ni} = \left(\frac{\tilde{L}_{NiNi}}{x_{Ni}} - \frac{\tilde{L}_{NiAl}}{x_{Al}}\right)\frac{x_{Ni}}{k_B T}\left(\frac{d\mu_{Ni}}{dx_{Ni}}\right)_{\mu_V=0} \tag{6-6a}$$

$$D_{Al} = \left(\frac{\tilde{L}_{AlAl}}{x_{Al}} - \frac{\tilde{L}_{AlNi}}{x_{Ni}}\right)\frac{x_{Al}}{k_B T}\left(\frac{d\mu_{Al}}{dx_{Al}}\right)_{\mu_V=0} \tag{6-6b}$$

where $\tilde{L}_{ij} = \Omega k_B T L_{ij}$, k_B is the Boltzmann constant and T is the absolute temperature. It can be seen from equations (6-6) that the self-diffusion coefficient depends on two parts, one, $\left(\frac{\tilde{L}_{NiNi}}{x_{Ni}} - \frac{\tilde{L}_{NiAl}}{x_{Al}}\right)$ for D_{Ni}, is related to kinetic coefficients and the other, $\frac{x_{Ni}}{k_B T}\left(\frac{d\mu_{Ni}}{dx_{Ni}}\right)_{\mu_V=0}$ for D_{Ni}, is related to thermodynamic factor. We will define thermodynamic factors ϕ for Ni and Al by the following two equations:

$$\phi_{Ni} = \frac{x_{Ni}}{k_B T}\left(\frac{d\mu_{Ni}}{dx_{Ni}}\right)_{\mu_V=0} \tag{6-7a}$$

$$\phi_{Al} = \frac{x_{Al}}{k_B T}\left(\frac{d\mu_{Al}}{dx_{Al}}\right)_{\mu_V=0} \tag{6-7b}$$

Allnatt has shown that the kinetic coefficients can be expressed as the following equation [140,141]:

$$\tilde{L}_{ij} = \frac{\left\langle \left(\sum_{\varsigma} \Delta\vec{R}_{\varsigma}^{i}(t)\right)\left(\sum_{\xi} \Delta\vec{R}_{\xi}^{j}(t)\right)\right\rangle}{(2d)tM} \tag{6-8}$$

where $\Delta\vec{R}_{\varsigma}^{i}(t)$ is the vector linking the end points of the trajectory of atom ς of specie *i* (*i* = Ni or Al) after time t and it can be kept track of in the kinetic Monte Carlo simulation. *M* is the number of crystal sites and *d* is the dimension of the substitutional crystal structure (*d*=3 in our simulation to represent the 3-dimensional crystal). The brackets mean an ensemble average conducted at equilibrium. The $\tilde{L}_{ij}$ coefficients have the same units as a diffusion coefficient.

As for the thermodynamic factor ϕ, it has been shown [135] that the thermodynamic factor can be related to the variances of the number of Ni and Al atoms by the following equations:

$$\phi_{Ni} = x_{Ni}x_{Al}\frac{\theta_{NiNi}\theta_{AlAl} - \theta_{NiAl}^2}{x_{Ni}\theta_{NiAl} + x_{Al}\theta_{AlAl}} \tag{6-9a}$$

$$\phi_{Al} = x_{Al}x_{Ni}\frac{\theta_{AlAl}\theta_{NiNi} - \theta_{AlNi}^2}{x_{Al}\theta_{AlNi} + x_{Ni}\theta_{NiNi}} \tag{6-9b}$$

where θ_{ij} is defined in terms of the variances of Ni atoms (N_{Ni}) and Al atoms (N_{Al}) by

$$\theta_{NiNi} = \frac{M}{k_B TQ}\left(\left\langle N_{Al}^2\right\rangle - \left\langle N_{Al}\right\rangle^2\right), \tag{6-10a}$$

$$\theta_{NiAl} = \theta_{AlNi} = -\frac{M}{k_B TQ}\left(\left\langle N_{Ni}N_{Al}\right\rangle - \left\langle N_{Ni}\right\rangle\left\langle N_{Al}\right\rangle\right), \tag{6-10b}$$

$$\theta_{AlAl} = \frac{M}{k_B TQ}\left(\left\langle N_{Ni}^2\right\rangle - \left\langle N_{Ni}\right\rangle^2\right), \tag{6-10c}$$

where $Q = \left(\left\langle N_{Ni}^2\right\rangle - \left\langle N_{Ni}\right\rangle^2\right)\left(\left\langle N_{Al}^2\right\rangle - \left\langle N_{Al}\right\rangle^2\right) - \left(\left\langle N_{Ni}N_{Al}\right\rangle - \left\langle N_{Ni}\right\rangle\left\langle N_{Al}\right\rangle\right)^2$ and *M* is the total number of crystal sites. Using equations (6-9) and (6-10) we can calculate the thermodynamic factors by

keeping track of the number of Ni and Al atoms in the grand canonical Monte Carlo simulation [135,142].

Based on Monte Carlo simulation data we calculated the self-diffusion coefficients as a function of bulk composition of B2-NiAl. Figure 6-1 shows the calculated self-diffusion coefficients for Ni and Al atoms in B2-NiAl at 1300K. In Al-rich region, only one composition was investigated, as it is extremely difficult to get good statistics in reasonable time period in this region. A primary reason is that the concentration of point defects or defect clusters necessary to mediate diffusion hops are very dilute in this region so requiring large Monte Carlo supercells to reproduce the equilibrium defect concentration in the kinetic Monte Carlo simulation. Furthermore, the concentration of vacancies is very high in the Al-rich region so the number of hops is much larger than that in Ni-rich region. In a kinetic Monte Carlo simulation, all hops must be considered simultaneously during each hop event.

From Fig. 6-1 we can see that the Ni has a higher self-diffusion coefficient than Al in the Ni-rich region while Al has a higher self-diffusion coefficient than Ni in the Al-rich region with the cross at the composition of around 52%. As we have demonstrated in chapter 5 Ni has a higher tracer diffusion coefficient than Al in the Ni-rich region due to the anti-structural bridge mechanism while Al and Ni atom have similar tracer diffusion coefficients in Al-rich region. Compared with the tracer diffusion coefficients the self-diffusion coefficients exhibit a very different profile in the Al-rich region. This is a result of a difference in thermodynamic factors between Ni and Al.

As we have mentioned above in equation (6-6), the intrinsic diffusion coefficient depends on two parts, one is related to kinetic coefficients and the other is related to thermodynamic factor. We calculated the thermodynamic factors (Eq. (6-7a) and (6-7b)) using Monte Carlo

simulations. Figure 6-2 shows the results for Ni and Al at 1300K in B2-NiAl. From Fig. 6-2 we can see that Ni and Al have identical thermodynamic factors in Ni-rich region while they have very different values in the Al-rich region. In the Al-rich region, the thermodynamic factor of Al is much larger than that of Ni by several orders of magnitude. It is this large difference in thermodynamic factors that results in self-diffusion coefficients that differ qualitively from the tracer diffusion coefficients in Al-rich region. While Ni and Al have similar tracer diffusion coefficients, Al has a much larger self-diffusion coefficient than Ni in the Al-rich region.

6.3 Two thermodynamic factors in B2-NiAl compound

The reason for two thermodynamic factors in B2-NiAl compound can be shown as follows. The Gibbs-Duhem equation (6-5), which is under the restriction that $\mu_V = 0$, can be rewritten as

$$\frac{x_{Ni} d\mu_{Ni}}{k_B T dx_{Ni}} + \frac{x_{Al} d\mu_{Al}}{k_B T dx_{Al}} \frac{dx_{Al}}{dx_{Ni}} = 0. \tag{6-11}$$

According to the definition of thermodynamic factors for Ni and Al (equation (6-7a) and (6-7b)), equation (6-11) is equivalent to $\phi_{Ni} + \phi_{Al} \frac{dx_{Al}}{dx_{Ni}} = 0$, which indicates that

$$\frac{\phi_{Al}}{\phi_{Ni}} = -\frac{dx_{Ni}}{dx_{Al}}. \tag{6-12}$$

In a binary system where vacancies are so dilute that their composition can be neglected, $1 = x_{Ni} + x_{Al} + x_V \approx x_{Ni} + x_{Al}$. This indicates that as the bulk composition changes, the increase of one component is achieved by the decrease of the other component and consequently, $\frac{dx_A}{dx_B} = -1$, leading to $\phi_A = \phi_B$ by equation (6-12). In such a system, the thermodynamic factors of the two components are equal. However, in the B2-NiAl compound this is not the case. Our previous

investigation has shown that the equilibrium concentration of vacancy in B2-NiAl can reach up to 15% in Al-rich region at 1300K and as the bulk composition of B2-NiAl changes, the decrease in Ni concentration, x_{Ni}, is not achieved by the means of an increase in the Al concentration, x_{Al}. As a result, $\frac{dx_A}{dx_B} = -1$ does not hold any longer in the B2-NiAl compound and two different thermodynamic factors are necessary for calculating intrinsic diffusion coefficients.

A detailed analysis can be achieved by keeping track of the Ni concentration x_{Ni} and Al concentration x_{Al} in the Monte Carlo simulation and Fig. 6-3 shows the relationship between the Ni concentration x_{Ni} and the Al concentration x_{Al} as the bulk composition of B2-NiAl changes at 1300K. From Fig. 6-3 we can see that in the Ni-rich region $\frac{dx_{Ni}}{dx_{Al}}$ is almost -1 indicating that ϕ_{Ni} is almost identical to ϕ_{Al}. The reason for this is that in Ni-rich region (as demonstrated in our previous investigation) the major point defects are antisite Ni atoms and vacancies are dilute (Ni vacancy is at the 10^{-3} level and Al vacancy is at the 10^{-7}~10^{-6} level). Consequently as the bulk composition changes in the Ni-rich region the increase (decrease) in x_{Ni} is achieved by a decrease (increase) in x_{Al}, causing $\frac{dx_{Ni}}{dx_{Al}}$ equal to -1. We can also see from Fig. 6-3 that in the Al-rich region the absolute value of $\frac{dx_{Ni}}{dx_{Al}}$ is very large, indicating that ϕ_{Al} is much larger than ϕ_{Ni}. This is because in the Al-rich region (see chapter 4) the major point defect are Ni vacancies and its concentration is too high to be neglected (10^{-2} ~ 10^{-1} level). Consequently as the bulk composition changes in the Al-rich region the increase (decrease) in x_{Ni} is achieved by the decrease (increase) in the concentration of Ni vacancies while x_{Al} remains almost constant. This

results in a large negative value of $\frac{dx_{Ni}}{dx_{Al}}$ and explains the much larger thermodynamic factor of Al in Al-rich region (Fig. 6-2).

From the above simulation result and analysis we can see that it is the high vacancy concentration and asymmetric distribution of vacancies between the Ni sublattice and Al sublattice that results in two different thermodynamic factors in the Al-rich region in the B2-NiAl compound. Much larger thermodynamic factors of Al than that of Ni in the Al-rich region leads to much larger self-diffusion coefficient of Al than that of Ni in this region. In addition to having a significant effect on self-diffusion coefficients, these two different thermodynamic factors also affect the interdiffusion coefficients in B2-NiAl compound, as we will demonstrate in the next section.

6.4 Two interdiffusion coefficients in B2-NiAl compound

In the previous section we have shown that there are two different thermodynamic factors for Ni and Al respectively in the B2-NiAl compound and this has a significant effect on the self-diffusion coefficients in this compound. In this section we will demonstrate that two different thermodynamic factors also have consequences for the interdiffusion coefficients in B2-NiAl.

The flux of atoms A relative to the laboratory frame is called the interdiffusion flux of A and it can be shown that in a binary system such as B2-NiAl this definition of the interdiffusion flux results in following identity [143,144]:

$$\tilde{J}_{Ni} + \tilde{J}_{Al} = 0 \tag{6-13}$$

where $\tilde{J}_i$ (i = Ni or Al) is the interdiffusion flux of component i. The interdiffusion flux can also be expressed as the following equations according to Fick's first law:

$$\tilde{J}_{Ni} = -\tilde{D}_{Ni}\nabla C_{Ni} \tag{6-14a}$$

$$\tilde{J}_{Al} = -\tilde{D}_{Al}\nabla C_{Al} \tag{6-14b}$$

where $\tilde{D}_i$ (i = Ni or Al) is the interdiffusion coefficient of component i. Also from equation (6-4) and (6-12) it is clear that the following relationship holds: (assuming an equilibrium vacancy concentration)

$$\frac{\nabla C_{Ni}}{\nabla C_{Al}} = -\frac{\phi_{Al}}{\phi_{Ni}} \tag{6-15}$$

Combining equations (6-13), (6-14) and (6-15) it is straightforward to obtain the following relationship between $\tilde{D}_{Ni}$ and $\tilde{D}_{Al}$:

$$\frac{\tilde{D}_{Al}}{\tilde{D}_{Ni}} = \frac{\phi_{Al}}{\phi_{Ni}} \tag{6-16}$$

Equation (6-16) indicates that the interdiffusion coefficients in B2-NiAl expressed as $\tilde{D}_{Ni}$ or $\tilde{D}_{Al}$ are not necessarily same. Instead, the ratio between $\tilde{D}_{Ni}$ and $\tilde{D}_{Al}$ is equal to that between thermodynamic factors ϕ_{Ni} and ϕ_{Al}. As we have demonstrated in the previous section, the thermodynamic factor of Al is much larger that of Ni in Al-rich region in B2-NiAl. This therefore results in different interdiffusion coefficients depending on whether an Al concentration gradient ∇C_{Al} or a Ni concentration gradient ∇C_{Ni} is used in Fick's first law (Eq. 6-14). This phenomenon is intuitively understandable because in Al-rich region almost all vacancies are distributed on Ni sublattice and the concentration of Al vacancy is so dilute, yielding an almost constant concentration of Al in Al-rich region in the B2-NiAl compound. Consequently, typical gradients in the concentration of Al, ∇C_{Al}, will be much smaller than that of Ni, ∇C_{Ni}. At the same time, the absolute value of the interdiffusion flux of Ni, $\tilde{J}_{Ni}$, should be equal to that of Al, $\tilde{J}_{Al}$. Thus from equation (6-14a) and (6-14b) we can see that the interdiffusion coefficient $\tilde{D}_{Al}$ should be much larger than $\tilde{D}_{Ni}$ in Al-rich region.

In order to confirm the above analysis, we directly calculated the interdiffusion coefficients $\tilde{D}_{Al}$ and $\tilde{D}_{Ni}$ using our Monte Carlo simulation data. Since the interdiffusion flux $\tilde{J}_i$ of component i (i =Ni or Al) is measured relative to the laboratory frame while the intrinsic diffusion flux J_i of component i is measured relative to the moving crystal frame, the following relationship should hold [138,140,145,146]:

$$\tilde{J}_{Ni} = J_{Ni} + C_{Ni}v \tag{6-17a}$$

$$\tilde{J}_{Al} = J_{Al} + C_{Al}v \tag{6-17b}$$

where v is the velocity of the crystal lattice frame relative to the laboratory frame defined by [138,140,145,146]

$$v = -\Omega(J_{Ni} + J_{Al}) \tag{6-18}$$

Combining equations (6-17) and (6-18) with equations (6-3), (6-4), (6-6), (6-7) and (6-15) it is not difficult to obtain the following expressions for interdiffusion coefficients of Ni and Al in B2-NiAl compound:

$$\tilde{D}_{Ni} = \left[x_{Ni}\left(\frac{\tilde{L}_{AlAl}}{x_{Al}} - \frac{\tilde{L}_{AlNi}}{x_{Ni}} \right) + (1 - x_{Ni})\left(\frac{\tilde{L}_{NiNi}}{x_{Ni}} - \frac{\tilde{L}_{AlNi}}{x_{Al}} \right) \right] \phi_{Ni} \tag{6-19a}$$

$$\tilde{D}_{Al} = \left[x_{Al}\left(\frac{\tilde{L}_{NiNi}}{x_{Ni}} - \frac{\tilde{L}_{NiAl}}{x_{Al}} \right) + (1 - x_{Al})\left(\frac{\tilde{L}_{AlAl}}{x_{Al}} - \frac{\tilde{L}_{NiAl}}{x_{Ni}} \right) \right] \phi_{Al} \tag{6-19b}$$

All the quantities on the right-hand side of equation (6-19) can be obtained from Monte Carlo simulations. Figure 6-4 shows the calculated interdiffuson coefficients of Ni and Al in the B2-NiAl compound at 1300K. From Fig. 6-4 we can see that $\tilde{D}_{Al}$ and $\tilde{D}_{Ni}$ are almost identical in the Ni-rich region, which is consistent with the identical thermodynamic factors of Ni and Al in this region. On the other hand, in the Al-rich region $\tilde{D}_{Al}$ is much larger than $\tilde{D}_{Ni}$, which is

consistent with the fact that the thermodynamic factor of Al is much larger than that of Ni in the Al-rich region.

From the above we can see that two interdiffusion coefficients exist for B2-NiAl depending on whether an Al concentration gradient ∇C_{Al} or a Ni concentration gradient ∇C_{Ni} is used in Fick's first law. Figure 6-5 shows some experimentally measured [53,59,60,147] interdiffusion coefficients in B2-NiAl compound. All experiments report just one interdiffusion coefficient in Al-rich alloys, contrary to our prediction that two different interdiffusion coefficients emerge when the vacancy concentration becomes large. Comparing Fig. 6-4 to Fig. 6-5 we can see that our calculated interdiffusion coefficients are in satisfactory agreement with the experiment results in Ni rich alloys. However, in Al-rich alloys, neither of the calculated interdiffusion coefficients agrees with experiments. The experimental studies determined the interdiffusion coefficient $\tilde{D}$ by the Sauer-Freise treatment [151] adopted by Wagner [152]. The definition of $\tilde{D}$ according to the treatment of Wagner is [152]

$$\tilde{D} = \frac{V_m (y_{Al} J_{Ni} - y_{Ni} J_{Al})}{\nabla y_{Al}} \tag{6-20}$$

where V_m is the molar volume without considering vacancies, y_i is the mole fraction of component i without considering vacancies (that is, $y_{Ni} + y_{Al} = 1$), such that,

$$V_m = \Omega / (1 - x_V) \tag{6-21}$$

$$y_{Ni} = x_{Ni} / (1 - x_V) \tag{6-22a}$$

$$y_{Al} = x_{Al} / (1 - x_V) \tag{6-22b}$$

By using Eq. (6-3), (6-15), (6-21) and (6-22), it can be shown that Eq. (6-20) becomes

$$\tilde{D} = \frac{\left(x_{Al} \frac{D_{Ni}}{\phi_{Ni}} + x_{Ni} \frac{D_{Al}}{\phi_{Al}} \right) \phi_{Al}}{1 - x_V + x_{Al} \left(\frac{\phi_{Al}}{\phi_{Ni}} - 1 \right)} \tag{6-23}$$

Because the definition (6-20) is symmetric with respect to Ni and Al, it is also true that

$$\tilde{D} = \frac{\left(x_{Ni} \frac{D_{Al}}{\phi_{Al}} + x_{Al} \frac{D_{Ni}}{\phi_{Ni}} \right) \phi_{Ni}}{1 - x_V + x_{Ni} \left(\frac{\phi_{Ni}}{\phi_{Al}} - 1 \right)} \tag{6-24}$$

Hence, the right-hand sides of Eq. (6-23) and Eq. (6-24) are equal to each other. By Eq. (6-6), we can compare the numerator of the right-hand side of Eq. (6-23) with Eq. (6-19b) and it can be seen that this numerator is just an approximation of $\tilde{D}_{Al}$. Similarly, the numerator of the right-hand side of Eq. (6-24) is an approximation of $\tilde{D}_{Ni}$. Figure 6-4 also shows the calculated $\tilde{D}$ along with $\tilde{D}_{Al}$ and $\tilde{D}_{Ni}$.

Thus, what the experiments measured, based on the Sauer-Freise treatment which starts from Eq. (6-20), ($\tilde{D}$) is different from $\tilde{D}_{Ni}$ and $\tilde{D}_{Al}$ which are the diffusion coefficients that appear in Fick's first law. In Ni-rich alloys, the vacancy is very dilute and the theromodynamic factors of Al and Ni are very similar, such that the denominators of the right-hand sides of Eq. (6-23) and (6-24) are almost 1. Consequently, $\tilde{D} \approx \tilde{D}_{Ni} \approx \tilde{D}_{Al}$ holds in Ni-rich alloys. However, in Al-rich alloys, the thermodynamic factors of Al and Ni are very different and thus denominators of the right-hand sides of Eq. (6-23) and (6-24) deviate significantly from 1. As a result, the value of $\tilde{D}$ is not equal to $\tilde{D}_{Ni}$ and $\tilde{D}_{Al}$.

From the above analysis we can see that we should compare the calculated value of $\tilde{D}$ instead of $\tilde{D}_{Ni}$ and $\tilde{D}_{Al}$ with the experimental results [53,59,60,147]. This comparison shows that in Ni-rich alloys the calculated $\tilde{D}$ agrees well with experimental results, however, in Al-rich alloys the calculated value is smaller than experimental results. This discrepancy could have two explainations. First, all experiments [53,59,60,147] measured the interdiffusion coefficients using polycrystalline sample while our simulation does not take account of the role of grain

boundary diffusion. It has been shown by the experiments that the tracer diffusion coefficient of Ni in polycrystalline B2-NiAl [50] is much larger than that in single crystal samples [49] (Fig. 5-2(b)). Another possible explanation for this disagreement may have its origin in the standard textbook assumption that the chemical potential of vacancies is zero since the dislocations and grain boundaries act as vacancy sources and sinks. However, in Al-rich B2-NiAl compound the concentration of vacancies is so high that it may locally deviate from its equilibrium value because insufficient dislocation and grain boundaries cannot effectively regulate an equilibrium concentration, leading to a vacancy chemical potential that is not zero.

6.5 Summary

In this chapter we have systematically investigated the self-diffusion and interdiffusion coefficients in the B2-NiAl compound from first-principles

Our investigation has shown that there are two different thermodynamic factors for Ni and Al in the Al-rich region while they are almost identical in Ni-rich region. In the Al-rich region the thermodynamic factor of Al is much larger than that of Ni resulting in a much larger self-diffusion coefficient for Al than for Ni. We have also shown that, due to the high vacancy concentration in Al rich B2-NiAl, there are two interdiffusion coefficients depending on whether interdiffusion is treated in terms of Al concentration gradients or Ni concentration gradients. However, the definition of interdiffusion coefficient measured from experiments is different from those in Fick's first law; these two types of definitions give similar values of interdiffusion coefficients in compounds with dilute vacancy while very different values in materials with high vacancy concentration.

Our investigation also shows that the specific characteristic of defect in B2-NiAl compounds, i.e. the high vacancy concentration and asymmetric distribution of vacancies between Ni sublattice and Al sublattice, is the reason for two different thermodynamic factors in Al-rich region and the resulting self-diffusion and interdiffusion coefficients in this composition region of B2-NiAl compound.

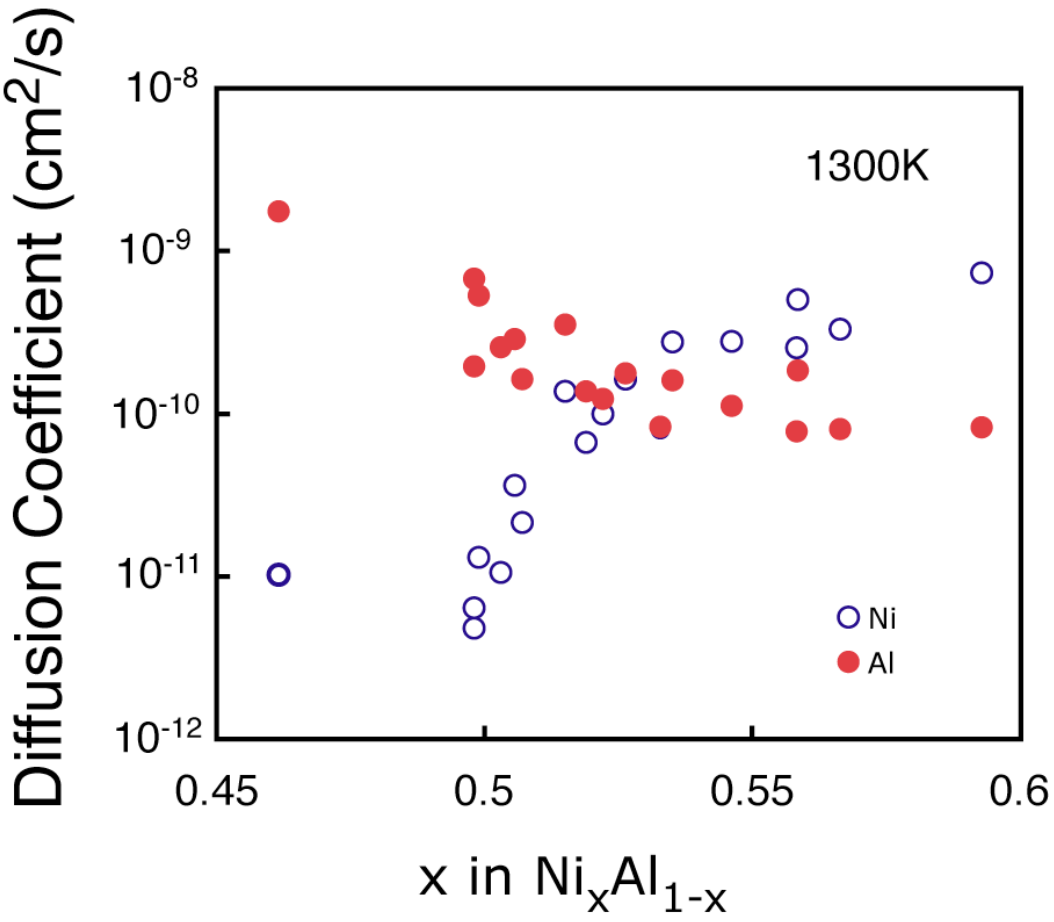

Figure 6-1 Calculated intrinsic diffusion coefficients for Ni (blue empty circles) and Al (red solid circles) in B2-NiAl at 1300K.

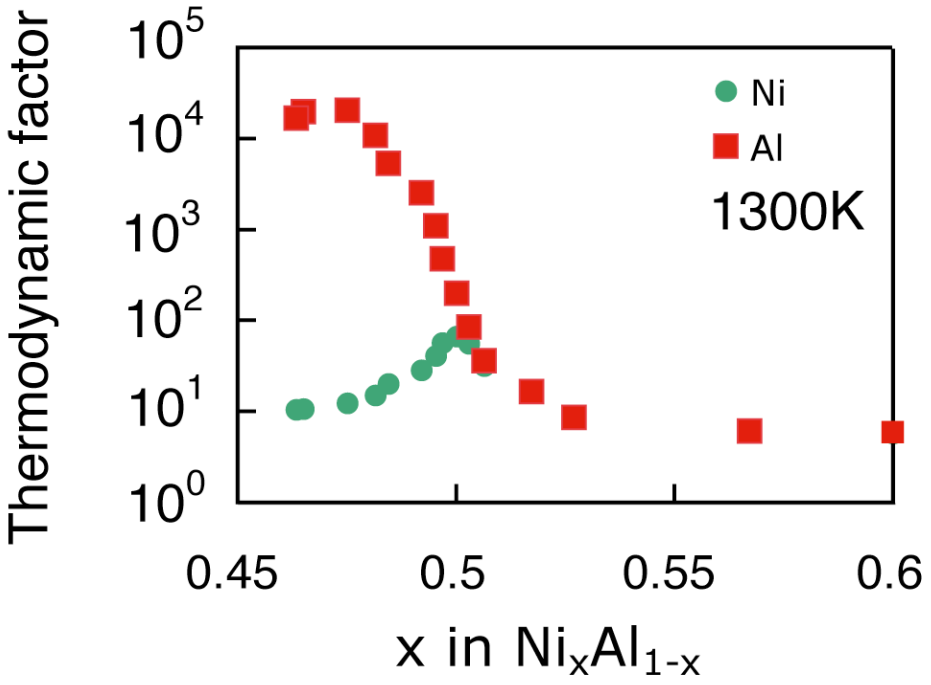

Figure 6-2 Calculated thermodynamic factors for Ni (green solid circles) and Al (red solid squares) in B2-NiAl at 1300K.

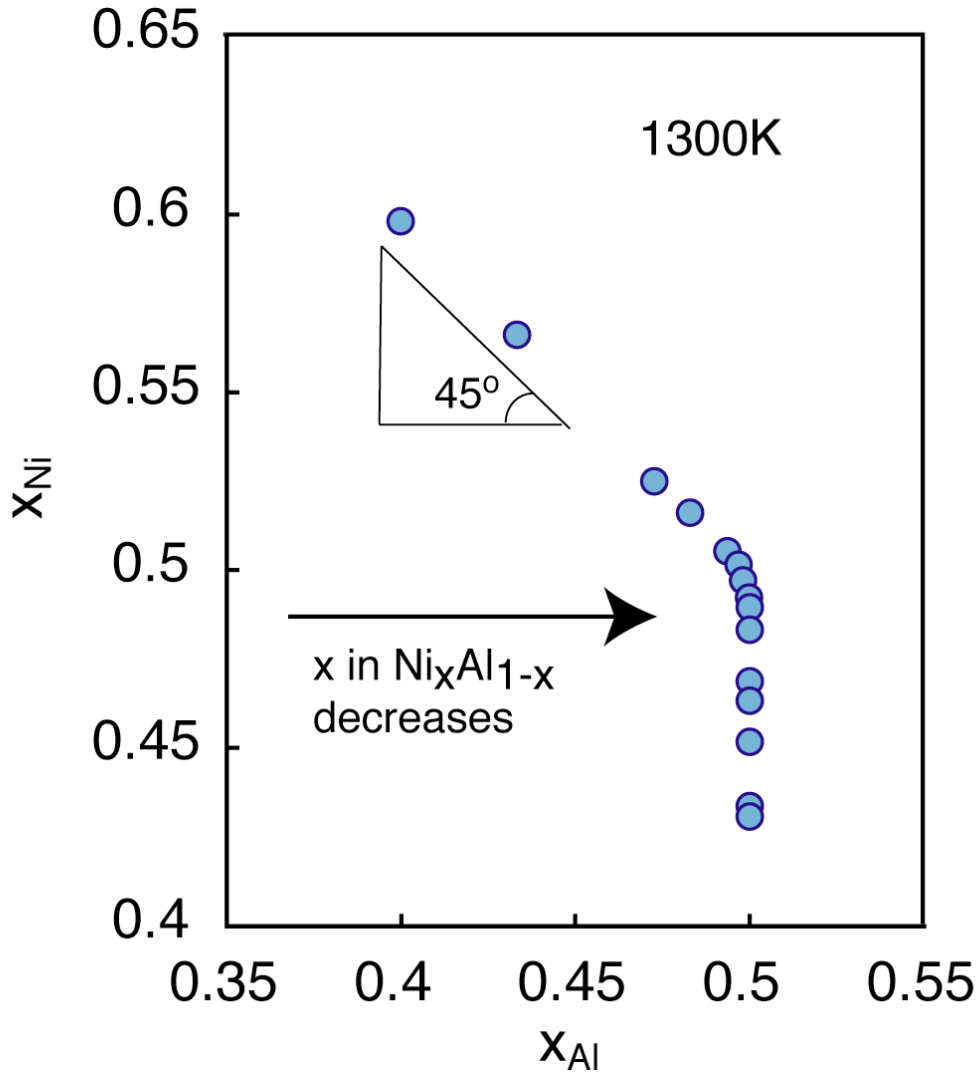

Figure 6-3. Relationship obtained from Monte Carlo simulation between Ni concentration, x_{Ni}, and Al concentration, x_{Al}, in B2-NiAl at 1300K.

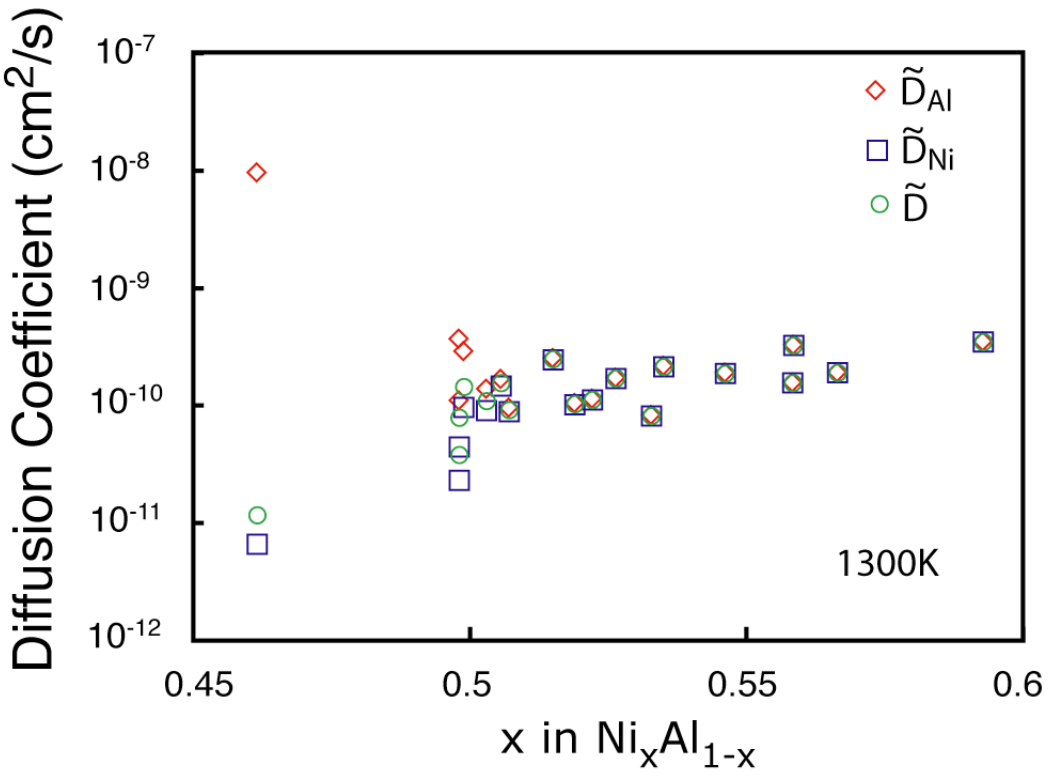

Figure 6-4 Interdiffusion coefficients calculated for Ni (blue squares), Al (red diamonds) and Wagner's definition (green circles) in B2-NiAl at 1300K.

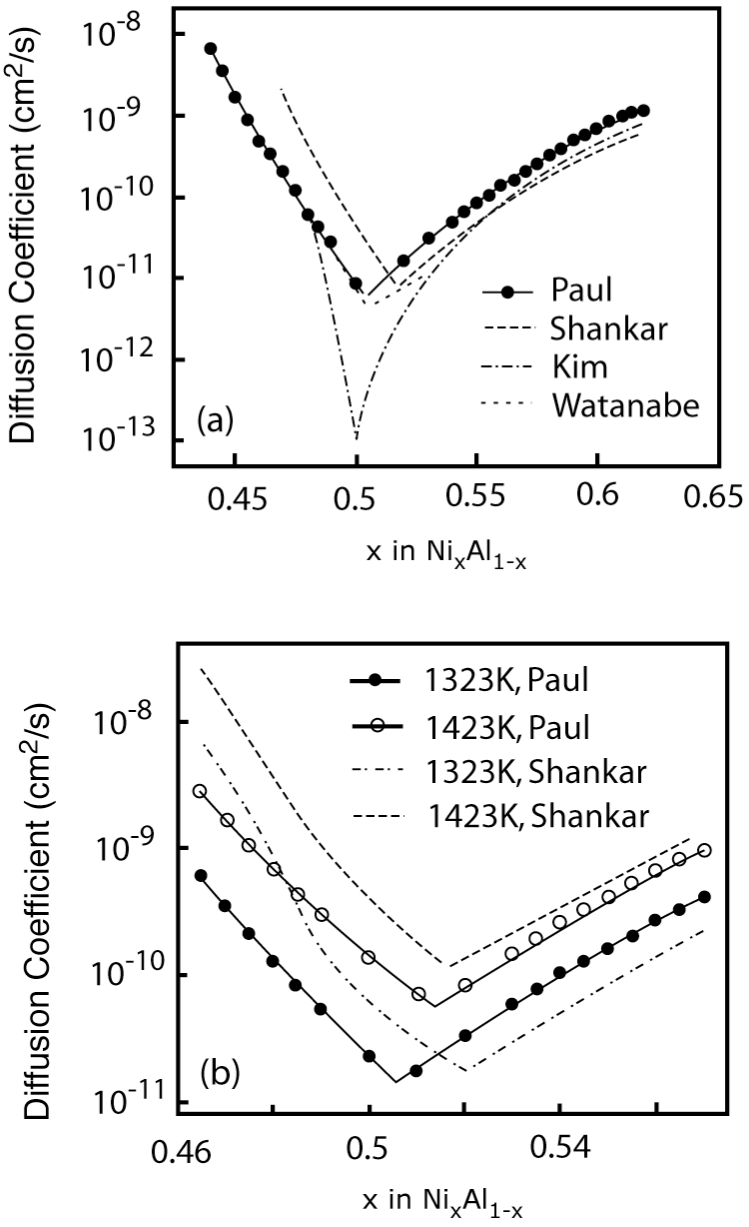

Figure 6-5. Experimental interdiffusion coefficients for B2-NiAl: (a) 1273K; (b) 1323K and 1423K. Data reported by Paul, Shankar, Kim, and Watanabe (see Ref. 59, 60, 53, and 147).

Chapter 7

Conclusion

In this thesis, we systematically investigated the thermodynamic and kinetic properties in an interstitial solid, the Ti-H system, and a substitutional solid, the Ni-Al system, from first-principles.

For the Ti-H system, the phase stability was investigated by accounting for the configurational degree of freedom, vibrational degrees of freedom and anisotropic states of stress. We find that:

(1) The tetragonal γ-TiH phase is predicted (within GGA) to be unstable relative to hcp Ti (α phase) and the fcc based δ-TiH_2. Zero point vibrational energy significantly affects the formation energies in this system and makes the γ phase even less stable relative to hcp Ti and δ-TiH_2. The coherency strains between hydride precipitates and the hcp Ti matrix stabilize γ-TiH relative to α-Ti and δ-TiH_2, explaining why it is observed experimentally. We also find that hydrogen prefers octahedral sites at low hydrogen concentration and tetrahedral sites at high concentration. Both harmonic vibrational as well as electronic origins for the cubic to tetragonal phase transformation of TiH_2 were investigated and we argue that anharmonic vibrational degrees of freedom are likely to play an important role in stabilizing cubic TiH_2.

For the Ni-Al system, we investigated the equilibrium defect concentration, interaction among defects, migration barriers for various diffusion mechanisms. We find that:

(2) The B2-NiAl compounds exhibits a variety of complex atomic hop mechanisms and can accommodate high concentrations of diffusion mediating defects. In this thesis, we systematically investigated important hop mechanism in B2-NiAl from first principles and discovered a low barrier collective hop involving a pair of Al atoms that can mediate the anti-structural bridge mechanism for Al diffusion. We also investigated the defect structure in B2-NiAl with Monte Carlo simulations, accounting for interactions among defects with a first-principles parameterized cluster expansion. An energetic attraction between Ni anti-site atoms and Al anti-site atoms leads to an increase in the Al anti-site concentration for Ni-rich B2-NiAl compounds, which is opposite to that predicted by mean field treatments. The inclusion of interactions among defects is also essential to predict the concentration of triple defects. We also predict a dramatic increase in the number of second and third nearest neighbor pairs occupied by an Al anti-site and a Ni-vacancy as the B2-NiAl alloy becomes Al rich and Ni rich. These pairs are essential for the anti-structural bridge mechanism for Al-diffusion.

To reveal the relative importance of various diffusion mechanisms for B2-NiAl, we performed a comprehensive kinetic Monte Carlo simulation of diffusion in B2-NiAl. Our model avoids the simple assumptions such as only allowing single atom nearest- and next-nearest-neighbor hops, non-interaction among defects, dilute vacancy and uniform vacancy concentration. These assumptions do not hold in B2 NiAl in which the vacancy concentration can reach 15%. From our simulations we find that:

(3) The Ni-anti-structural-bridge hop is the dominant hop for Ni diffusion in Ni-rich alloys and the Al-anti-structural-bridge hop is the dominant hop for Al diffusion in Al-rich alloys. Combined with ASB-Al, the six-jump-cycle is also a major type of hop in Al-rich side due to the relative high concentration of Ni vacancies in spite of the high migration barrier.

Compared to the hops mentioned above, the triple-defect hop mechanism has a relatively constant effect over the whole composition range contributing to both Ni and Al diffusion. Furthermore, we have demonstrated the importance of simultaneous multi-atom hops in mediating atomic transport. These are very important in understanding the diffusion phenomenon in a compound with such a simple structure – B2 NiAl. It can be reasonably thought that in a real material system having a much more complicated structure than B2, the simplified textbook assumptions about diffusion are also likely to break down. In such a system, collective hops involving many atoms are likely to happen; vacancy concentrations may depend strongly on bulk composition and might not be dilute. Furthermore, interactions among defects are complicated and too important to neglect. Our model provides a tool to study diffusion process with much more realistic assumptions and lays a solid foundation for further investigation.

In analyzing macroscopic metrics of diffusion in B2-NiAl, we find that:

(4) There are two different thermodynamic factors for Ni and Al in Al-rich alloys while they are almost identical in Ni-rich alloys. In Al-rich alloys the thermodynamic factor of Al is much larger than that of Ni causing the self-diffusion coefficient and interdiffusion coefficient of Al to be much larger than those of Ni. On the other hand, in Ni-rich region the interdiffusion coefficients of Al and Ni are identical and the self-diffusion coefficient of Ni is higher than that of Al due to the kinetic factors. The definition of interdiffusion coefficient measured from experiments is different from those in Fick's first law; these two types of definitions give similar values of interdiffusion coefficients in compounds with dilute vacancy while very different values in materials with high vacancy concentration. Our investigation also shows that the specific characteristic of defects in the B2-NiAl compound, i.e. the high vacancy concentration and asymmetric distribution of vacancies between Ni sublattice and Al sublattice, is the reason

for two different thermodynamic factors in Al-rich region and the resulting self-diffusion and interdiffusion coefficients in this composition region of B2-NiAl compound.

Appendix A

Here we describe a method to determine values for the relative chemical potentials, $\tilde{\mu}_{Ni}$ and $\tilde{\mu}_{Al}$, corresponding to an equilibrium vacancy concentration determined by μ_V=0. The chemical potentials, μ_i (i=Ni, Al or vacancies), are related to the Gibbs free energy of the solid at fixed temperature T according to

$$\mu_i = g(T, x_{Ni}, x_{Al}) + (\delta_{iNi} - x_{Ni})\frac{\partial g}{\partial x_{Ni}} + (\delta_{iAl} - x_{Al})\frac{\partial g}{\partial x_{Al}} \qquad \text{(A1)}$$

where $g(T, x_{Ni}, x_{Al})$ is the free energy of a B2 NiAl crystal normalized by the number of crystal sites, $x_i = N_i/M$ is the fraction of crystal sites occupied by component i (Ni, Al or vacancies) and δ_{ij} is the Kronecker delta (the free energy per crystal site depends only on x_{Ni} and x_{Al} since $x_{Ni} + x_{Al} + x_V = 1$). Using Eq. (A1), it is possible to write the relative chemical potentials $\tilde{\mu}_i$ as the partial derivative of g with respect to x_i according to

$$\tilde{\mu}_i = \mu_i - \mu_V = \frac{\partial g}{\partial x_i} \qquad \text{(A2)}$$

showing that this quantity is a measure of the change in free energy as component i is added at the expense of a vacancy (keeping the number of crystal sites constant). Combining Eq. (A1) for the vacancy chemical potential μ_V and Eq. (A2) for i=Ni and Al, yields

$$\mu_V = g(T, x_{Ni}, x_{Al}) - x_{Ni}\tilde{\mu}_{Ni} - x_{Al}\tilde{\mu}_{Al} \qquad \text{(A3)}$$

By setting μ_V=0, we obtain a constraint between $\tilde{\mu}_{Ni}$ and $\tilde{\mu}_{Al}$ that defines a path in chemical potential space corresponding to an equilibrium vacancy concentration. It is along this path in

$\tilde{\mu}_{Ni}$ and $\tilde{\mu}_{Al}$ space for which μ_V=0 that we must calculate the equilibrium concentrations $x_{Ni}(\tilde{\mu}_{Ni},\tilde{\mu}_{Al})$ and $x_{Al}(\tilde{\mu}_{Ni},\tilde{\mu}_{Al})$ as well as the equilibrium defect concentrations for the B2 NiAl compound within grand canonical Monte Carlo simulations.

Before we can determine the path in $\tilde{\mu}_{Ni}$ and $\tilde{\mu}_{Al}$ space satisfying μ_V=0, we must know $g(T,x_{Ni},x_{Al})$. This crystal free energy is accessible with free energy integration of grand canonical Monte Carlo results. To this end, we introduce a grand canonical free energy of a B2-NiAl crystal with *M* sites as

$$\Phi(T,\tilde{\mu}_{Ni},\tilde{\mu}_{Al}) = G(T,\overline{N}_{Ni},\overline{N}_{Al}) - \overline{N}_{Ni}\tilde{\mu}_{Ni} - \overline{N}_{Al}\tilde{\mu}_{Al} \qquad \text{(A4)}$$

where $\overline{N}_{Ni}$ and $\overline{N}_{Al}$ are average concentrations calculated within the grand canonical ensemble (fixed *M*, *T*, $\tilde{\mu}_{Ni}$ and $\tilde{\mu}_{Al}$) and $G(T,\overline{N}_{Ni},\overline{N}_{Al})$ is the total free energy of the crystal with *M* sites (i.e., $G(T,\overline{N}_{Ni},\overline{N}_{Al}) = M \cdot g(T,x_{Ni},x_{Al})$). The differential of Φ can be conveniently written as

$$d(\beta\Phi) = \overline{\Omega}d\beta - \beta\overline{N}_{Ni}d\tilde{\mu}_{Ni} - \beta\overline{N}_{Al}d\tilde{\mu}_{Al} \qquad \text{(A5)}$$

where $\beta=1/k_BT$ and $\overline{\Omega}$ is the average grand canonical energy. By numerically integrating Eq. (A5) along a particular trajectory in β, $\tilde{\mu}_{Ni}$, $\tilde{\mu}_{Al}$ space, it is possible to relate the grand canonical free energy at one set of thermodynamic boundary conditions (T_o, $\tilde{\mu}_{Ni_0}$, $\tilde{\mu}_{Al_0}$) to another (T, $\tilde{\mu}_{Ni}$, $\tilde{\mu}_{Al}$). At various increments along the trajectory, values for $\overline{\Omega}$, $\overline{N}_{Ni}$ and $\overline{N}_{Al}$ of Eq. (A5) can be calculated with grand canonical Monte Carlo simulations. A convenient reference state to use as starting point for the integration of Eq. (A5) is one in which the grand canonical free energy can easily be calculated. For B2-NiAl such a reference state could correspond to the perfectly ordered alloy at a temperature close to zero Kelvin where Φ can be calculated with a low temperature expansion [10,133]. The free energy $G(T,\overline{N}_{Ni},\overline{N}_{Al})$ can then be calculated using Eq.

(A4), which when normalized by M yields $g(T, x_{Ni}, x_{Al}) = G(T, N_{Ni}, N_{Al})/M$, to be used in Eq. (A3) to determine the path in $\tilde{\mu}_{Ni}$ and $\tilde{\mu}_{Al}$ space for which μ_V=0.

Appendix B

Here we describe an ideal solution model to calculate the free energy of dilute hcp Ti-H system. Due to the fact that the hcp host is stable only at very dilute hydrogen concentration, we applied an ideal dilute solution model to the hcp host structures. Energy for adding an isolated H atom in either a tetrahedral interstitial site or an octahedral interstitial site within hcp Ti host was calculated in a 36-atoms unit cell. Comparison with the calculations within a 96-atoms cell indicates that this is well converged with supercell size.

Suppose that our hcp Ti host has M Ti atoms, so this crystal will have $N_t = 2M$ tetrahedral interstitial sites and $N_o = M$ octahedral interstitial sites. If we insert n H atoms into interstitial sites of hcp Ti, with n_t H atoms at the tetrahedral interstitial sites and n_o H atoms at the octahedral interstitial sites (the dilute concentration of H atoms insures that $n_t + n_o = n << M$), then the formation energy of this resulting dilute solution is

$$E = \tilde{E} + n_t \Delta E_t + n_o \Delta E_o, \tag{B1}$$

where $\tilde{E}$ is the formation energy of hcp Ti (with reference state of fcc Ti and δ-TiH_2). ΔE_t, the energy change due to inserting one H atom into a tetrahedral interstitial site in hcp Ti host, is defined as

$$\Delta E_t = E_t - \tilde{E}, \tag{B2}$$

where E_t is the formation energy of hcp Ti with one H atom inserted into a tetrahedral interstitial site; similarly, ΔE_o, the energy change due to inserting one H atom into an octahedral interstitial

site in hcp Ti host, is defined as

$$\Delta E_o = E_o - \tilde{E}, \tag{B3}$$

where E_o is the formation energy of hcp Ti with one H atom inserted into an octahedral interstitial site. The partition function of this Ti-H dilute solution can be derived as

$$Q = \sum_{n_t=0}^{n} C_{N_t}^{n_t} C_{N_o}^{n_o} \exp(-\beta E), \tag{B4}$$

where $\beta = \frac{1}{k_B T}$ with k_B the Boltzmann constant and T absolute temperature. Hence the free energy of the dilute solution is

$$G = -\frac{1}{\beta} \ln Q. \tag{B5}$$

Applying the maximum term method and Sterling's approximation, we can obtain the expression for G:

$$\begin{aligned} G = \tilde{E} - \frac{1}{\beta}\{&(N_t \ln N_t - N_t) - (n_t^* \ln n_t^* - n_t^*) - [(N_t - n_t^*)\ln(N_t - n_t^*) - (N_t - n_t^*)] + \\ &(N_o \ln N_o - N_o) - [(n - n_t^*)\ln(n - n_t^*) - (n - n_t^*)] - \\ &[(N_o - n + n_t^*)\ln(N_o - n + n_t^*) - (N_o - n + n_t^*)] - \\ &\beta[n_t^* \Delta E_t + (n - n_t^*)\Delta E_o]\}, \end{aligned} \tag{B6}$$

where

$$n_t^* = \frac{-(cn - cN_o - N_t - n) - \sqrt{(cn - cN_o - N_t - n)^2 - 4(1-c)N_t n}}{2(1-c)} \tag{B7}$$

with $c = \exp[\beta(\Delta E_t - \Delta E_o)]$ and $n = 3Mx$, where x is the H concentration in TiH_{3x}.

Thermodynamic properties such as Gibbs free energy G, chemical potential $\mu = \frac{\partial G}{\partial n}$ were calculated as a function of H concentration x and temperature T using Eq. (B6). The

calculated free energies were used to compete with those of fcc host structures to construct the whole phase diagram of TiH_{3x} system.

References

1. J. M. Sanchez, F. Ducastelle, D. Gratias, Physica A **128**, 334 (1984).
2. D. de Fontaine, in *Solid State Physics,* edited by H. Ehrenreich (Academic Press, NY, 1994), p. 33.
3. M. H. F. Sluiter, Y. Watanabe, D. de Fontaine, Y. Kazazoe, Phys. Rev. B **53**, 6136 (1996).
4. A. Van der Ven, M. K. Aydinol, G. Ceder, G. Kresse, J. Hafner, Phys. Rev. B **58**, 2975 (1998).
5. D. Carlier, A. Van der Ven, C. Delmas, G. Ceder, Chem. Mater. **15**, 2651 (2003).
6. A. Van de Walle, G. Ceder, J. Phase Eq. **23**, 348 (2002).
7. C. Wolverton, V. Ozolins, A. Zunger, Phys. Rev. B **57**, 4332 (1998).
8. K. M. Rabe, J. D. Joannopoulos, Phys. Rev. Lett. **59**, 570 (1987).
9. W. Zhong, D. Vanderbilt, K. M. Rabe, Phys. Rev. Lett. **73**, 1861 (1994).
10. A. Van de Walle, M. Asta, Model. Simul. Mater. Sci. and Eng. **10**, 521 (2002).
11. M. E. Arroy, Yi de Dompablo, A. Van der Ven, G. Ceder, Phys. Rev. B **66**, 064112 (2002).
12. P. D. Tepesch et al. J. Am. Cer. Soc. **79**, 2033 (1996).
13. L. Schlapbach and A. Zuttel, Nature (London) **414**, 353 (2001).
14. H. K. Birnbaum, M. L. Grossbeck, and M. Amano, J. Less-Common Met. **49**, 357 (1976).
15. D. S. Shih, I. M. Robertson, and H. K. Birnbaum, Acta Metall. **36**, 111 (1988).
16. S. Takano and T. Suzuki, Acta Metall. **22**, 265 (1974).
17. J. P. Hirth and J. R. Rice, Metall. Trans. A **11**, 1501 (1980).
18. R. A. Oriani and P. H. Josephic, Acta Metall. **22**, 1065 (1974).
19. A. Van der Ven and G. Ceder, Acta Mater. **52**, 1223 (2004).
20. A. Van der Ven and G. Ceder, Phys. Rev. B **67**, 060101(R) (2003).
21. C. D. Beachem, Metall. Trans. **3**, 437 (1972).
22. H. K. Birnbaum and P. Sofronis, Mater. Sci. Eng., A **176**, 191 (1994).
23. G. Lu, Q. Zhang, N. Kioussis, and E. Kaxiras, Phys. Rev. Lett. **87**, 095501 (2001).
24. C. Q. Chen, S. X. Li, and K. Lu, Acta Mater. **51**, 931 (2003).
25. C. Q. Chen, S. X. Li, H. Zheng, L. B. Wang, and K. Lu, Acta Mater. **52**, 3697 (2004).
26. D. F. Teter, I. M. Robertson, and H. K. Birnbaum, Acta Mater. **49**, 4313 (2001).
27. G. H. Kim, C. H. Chun, S. G. Lee, and J. Y. Lee, Acta Metall. Mater. **42**, 3157 (1994).
28. N. Michel et al., J. Alloys Compd. **330**, 280 (2002).
29. H. H. Lee, K. Y. Lee, and J. Y. Lee, J. Alloys Compd. **239**, 63 (1996).
30. T. Schober and W. Schafer, J. Less-Common Met. **74**, 23 (1980).
31. B. Bogdanovic and M. Schwickardi, J. Alloys Compd. **253**, 1 (1997).
32. J. E. Bailey, Acta Metall. 11, **267** (1963).
33. G. J. C. Carpenter, Acta Metall. **26**, 1225 (1978).
34. H. L. Yakel, Acta Crystallogr. **11**, 46 (1958).
35. H. Numakura and M. Koiwa, Acta Metall. **32**, 1799 (1984).

36. H. Numakura, M. Koiwa, H. Asano, and F. Izumi, Acta Metall. **36**, 2267 (1988).
37. H. Numakura, M. Koiwa, H. Asano, and F. Izumi, Scr. Metall. **20**, 213 (1986).
38. J. R. Nicholls, Advances in Coating Design for High Performance Gas Turbines. MRS Bulletin 659 (2003).
39. V. K. Tolpygo and D. R. Clarke, Acta Mater. **52**, 5115 (2004).
40. V. K. Tolpygo and D. R. Clarke, Acta Mater. **52**, 5129 (2004).
41. J. Bradley and A. Taylor, Proceedings of the Royal Society of London **A159**, 56 (1937).
42. P. A. Korzhavyi, A. V. Ruban, A. Y. Lozovoi, Y. Vekilov, I. A. Abrikosov, B. Johansson, Phys. Rev. B **61**, 6003 (1999).
43. Y. Mishin, M. J. Mehl, D. A. Papaconstantopoulos, Phys. Rev. B **65**, 224114 (2002).
44. M. P. Gururajan and T. A. Abinandanan, Intermetallics **8**, 759 (2000).
45. A. Van der Ven, J. C. Thomas, Q. Xu, B. Swoboda and D. Morgan, Physical Review B **78,** 104306 (2008).
46. A. Van der Ven and G. Ceder, Physical Review Letters **94,** 045901 (2005).
47. S. Divinski and C. Herzig, Intermetallics **8,** 1357 (2000).
48. S. Divinski, Y.S. Kang, W. Loser and C. Herzig, Intermetallics **12**, 511 (2004).
49. S. Frank, S. Divinski, U. Sodervall and C. Herzig, Acta Materialia **49**, 1399 (2001).
50. G.F. Hancock and B. Mcdonnel, Physical Status Solidi A: Applied Research **4**, 143 (1971).
51. Herzig and S. Divinski, Intermetallics **12**, 993 (2004).
52. R. Kao and Y.A. Chang, Intermetallics **1**, 237 (1993).
53. S. Kim and Y.A. Chang, Metallurgical and Materials Transactions A: Physical Metallurgy and Materials Science **31,** 1519 (2000).
54. Y. Mishin and D. Farkas, Scripta Materialia **39**, 625 (1998).
55. Y. Mishin and D. Farkas, Defect and Diffusion Forum **143**, 303 (1997).
56. Y. Mishin and D. Farkas, Philosophical Magazine A-Physics of Condensed Matter Structure Defects and Mechanical Properties **75**, 169 (1997).
57. Y. Mishin and D. Farkas, Philosophical Magazine A-Physics of Condensed Matter Structure Defects and Mechanical Properties **75**, 187 (1997).
58. Y. Mishin, A.Y. Lozovoi and A. Alavi, Physical Review B **67,** 014201 (2003).
59. A. A. Paul, Kodentsov and F.J.J. van Loo, Journal of Alloys and Compounds **403**, 147 (2005).
60. S. Shankar and L.L. Seigle, Metallurgical Transactions A Physical Metallurgy and Materials Science **9**, 1467 (1978).
61. Meyer and M. Fahnle, Physical Review B **59**, 6072 (1999).
62. Y. Minamino, Y. Koizumi and Y. Inui, Defect and Diffusion Forum **194–199,** 517 (2001).
63. M. Arita, M. Koiwa and S. Ishioka, Acta Metallurgica **37**, 1363 (1989).
64. S. Divinski and C. Herzig, Defect and Diffusion Forum **203–205,** 177 (2002).
65. S. Divinski, S. Frank, U. Sodervall and C. Herzig, Defect and Diffusion Forum **194–199,** 487 (2001).
66. W. Elcock and C.W. McCombie, Physical Review **109,** 6 (1958).
67. N.A. Stolwijk, M. Van Gend and H. Bakker, Philosophical Magazine **A42**, 783 (1980).
68. R. K. Pathria. *Statistical Mechanics, second edition*. Butterworth Heinemann. (1996).
69. D. A. McQuarrie. *Statistical Thermodynamics*. University Science Books, (1973).
70. A. Zunger. In P. E. A. Turchi and A. Gonis, editors, *Statics and Dynamics of Alloy Phase Transformations*, p. 361. Plenum, New York, (1994).
71. P. Hohenberg and W. Kohn. Phys. Rev., **136**, B864 (1964)

72. K. Binder and D. W. Heermann. *Monte Carlo Simulation in Statistical Physics*. Springer Verlag, (1988).
73. N. W. Ashcroft and N. D. Mermin. *Solid State Physics*. Saunders College Publishing, (1976).
74. O. Madelung. *Introduction to Solid State Theory*. Springer Verlag, (1978).
75. R. M. Martin, *Electronic Structure*. Cambridge Unversity Press, (2004).
76. M. Born and J. R. Oppenheimer, Ann. Physik **84**, 457 (1927).
77. D. R. Hartree, Proc. Cambridge Phil. Soc. **24**, 89 (1928).
78. S. Jenkins, *An Introduction to Solid State Many-Body Theory*, University of Exeter, (1997).
79. V. Fock, Z. Phys. **61**, 126 (1930).
80. W. Kohn and L. J. Sham, Phys. Rev. **140**, A1133 (1965).
81. J. P. Perdew and K. Burke, Int. J. Quant. Chem. **57**, 309 (1996).
82. F. Herman, J. P. Van Dyke, and I. P. Ortenburger, Phys. Rev. Lett. **22**, 807 (1969).
83. P. S. Svendsen and U. von Barth, Phys. Rev. B **54**, 17402 (1996).
84. M. C. Payne, M. P. Ter, d. C. Allan, T. A. Arias and J. D. Joannopoulos, Reviews of Modern Physics, **64**,1045 (1992).
85. J. P. Perdew and Y. Wang, Phys. Rev. B **45**, 13244 (1992).
86. J. P. Perdew, K. Burke, and M. Ernzerhof, Phys. Rev. Lett. **77**, 3865 (1996).
87. D. J. Singh. *Planewaves, Pseudopotentials and the LAPW Method*. Kluwer Academic Publishers, (1994).
88. J. C. Phillips and L. Kleinman. Phys. Rev. **116**, 287 (1959).
89. P. E. Blochl, Phys. Rev. B **50**, 17953 (1994).
90. G. Kresse and J. Furthmuller, Phys. Rev. B **54**, 11169 (1996).
91. G. Kresse and J. Furthmuller, Comput. Mater. Sci. **6**, 15 (1996).
92. G. Kresse and D. Joubert, Phys. Rev. B **59**, 1758 (1999).
93. Q. Xu and A. Van der Ven, Intermetallics, **17**, 319 (2009).
94. Q. Xu and A. Van der Ven, Phys. Rev. B **76**, 064207 (2007).
95. V. Ozolins, C. Wolverton, and A. Zunger, Phys. Rev. B **57**, 6427 (1998).
96. A. Seko, K. Yuge, F. Oba, A. Kuwabara, I. Tanaka, and T. Yamamoto, Phys. Rev. B **73**, 094116 (2006).
97. A. Van der Ven and G. Cedar, Phys. Rev. B **71**, 054102 (2005).
98. H. R. Tang, A. Van der Ven, and B. L. Trout, Phys. Rev. B **70**, 045420 (2004).
99. D. J. Siegel, C. Wolverton, and V. Ozolins, Phys. Rev B **75**, 014101 (2007).
100. R. R. Picard and R. D. Cook, J. Am. Stat. Assoc. **79**, 575 (1984).
101. J. Shao, J. Am. Stat. Assoc. **88**, 486 (1993).
102. G. L. W. Hart, V. Blum, M. J. Walorski, and A. Zunger, Nat. Mater. **4**, 391 (2005).
103. F. Lechermann and M. Fahnle, Physical Review B **63**, 012104 (2000).
104. D. D. Morgan. Computational Studies of Alloy Phase Stability. PhD dissertation, University of California, Berkeley, Department of Physics, (1998).
105. V. Ozolins. Structural and Vibrational Properties of Transition Metal Systems from Ab initio Electronic-Structure Calculations. PhD dissertation, Royal Institute of Technology, Stockholm, Sweden, Department of Physics, (1996).
106. P.D. Tepesch, G.D. Garbulsky and G. Ceder, Physical Review Letters **74**, 2272 (1995).
107. C. Han, A. Van der Ven, G. Ceder and B.J. Hwang, Physical Review B **72**, 205409 (2005).
108. S. Ross, *Introduction to Probability Models*, 7th ed., Academic Press (2000).

109. F. M. Bulnes, V. D. Pereyra, and J. L. Riccardo, Collective surface diffusion: n-fold way kinetic Monte Carlo simulation, Phys. Rev. E **58**, 86 (1998).
110. G. H. Vineyard, Frequency factors and isotope effects in solid-state rate processes, J. Phys. Chem. Solids **3**, 121 (1957).
111. R. Gomer, Diffusion of adsorbates on metal surfaces, Reports on Progress in Physics **53**, 917 (1990).
112. G. Ceder, Comput. Mater. Sci. **1**, 144 (1993).
113. A, Van de Walle and G, Ceder, Rev. Mod. Phys. **74**, 11 (2002).
114. S. Baroni, S. de Gironcoli, A. Dal Corso, and P. Giannozzi, Rev. Mod. Phys. **73**, 515 (2001).
115. S. Wei and M. Y. Chou, Phys. Rev. Lett. **69**, 2799 (1992).
116. H. J. Monkhorst and J. D. Pack, Phys. Rev. B **13**, 5188 (1976).
117. M. Methfessel and A. T. Paxton, Phys. Rev. B **40**, 3616 (1989).
118. C. Kittel, *Introduction to Solid State Physics*, 6th ed. (Wiley, New York, 1986).
119. G. J. Ackland, Phys. Rev. Lett. **80**, 2233 (1998).
120. W. Wolf and P. Herzig, J. Phys.: Condens. Matter **12**, 4535 (2000).
121. A. Van de Walle, M. Asta, and G. Ceder, CALPHAD: Comput. Coupling Phase Diagrams Thermochem. **26**, 539 (2002).
122. K. M. Rabe and U. V. Waghmare, Phys. Rev. B **52**, 13236 (1995).
123. U. V. Waghmare and K. M. Rabe, Phys. Rev. B **55**, 6161 (1997).
124. W. Zhong, D. Vanderbilt, and K. M. Rabe, Phys. Rev. B **52**, 6301 (1995).
125. F. Ducastelle, R. Candron, and P. Costa, J. Phys. (paris) **31**, 57 (1970).
126. M. Gupta, Solid State Commun. **29**, 47 (1979).
127. R. C. Bowman, E. L. Venturini, B. D. Craft, A. Attalla, and D. B. Sullenger, Phys. Rev. B **27**, 1474 (1983).
128. M. Gupta, Phys. Rev. B **25**, 1027 (1982).
129. K. A. Marino and E. A. Carter, Phys. Rev. B **78**, 184105 (2008).
130. M. Ellner, S. Kek and B. Predel, Journal of the Less Common Metals **154**, 207 (1989).
131. P. Nash, M.F. Singleton and J.L. Murray, *Phase diagrams of binary nickel alloys*, ASM International, Materials Park, OH (1991).
132. A. Lutze-Birk and H. Jacobi, Scripta Meterialia **9**, 761 (1975).
133. F. Kohan, P.D. Tepesch, G. Ceder and C. Wolverton, Computational Materials Science **9**, 389 (1998).
134. M. Kogachi, T. Tanahashi, Y. Shirai, and M. Yamaguchi, Determination of vacancy concentration and defect structure in the B2 type NiAl β-phase alloys, Scripta Materialia **34**, 243 (1996).
135. A. Van der Ven, H. Yu, K. Thornton and G. Ceder, Progress in Materials Science. In press.
136. Z. Qin and G. E. Murch, Philosophical Magazine A **71**, 323 (1995).
137. L. Bencze, D. D. Raj, D. Kath, W. A. Oates, L. Singheiser and K. Hilpert, Metallurgical and Materials Transactions B **35B**, 867 (2004).
138. R. E. Howard, A. B. Lidiard, Rep. Prog. Phys. **27**, 161(1964).
139. K. W. Kehr, K. Binder, S. M. Reulein, Phys. Rev. B **39**, 4891 (1989).
140. A. R. Allnatt, A. B. Lidiard, *Atomic Transport in Solids* (Cambridge University Press, Cambridge, 1993).
141. A. R. Allnatt, J. Chem. Phys. **43**, 1855 (1965).
142. T. L. Hill, *Statistical Mechanics*, (Dover Publications, New York, 1987).

143. R. Haase, *Thermodynamics of Irreversible Processes* (Addison Wesley, Reading, MA, 1969).
144. J. S. Kirkaldy and D. J. Young, *Diffusion in the Condensed State* (Institute of Metals, London, 1987).
145. R. W. Balluffi, S. M. Allen, W. C. Carter, *Kinetics of Materials*, (Hoboken, N. J.:Wiley-Interscience, 2005).
146. M. E. Glicksman, *Diffusion in Solids* (Wiley-Interscience, 2000).
147. M. Watanabe, Z. Horita, M. Nemoto, Defect Diffus. Forum **143-147**, 345 (1997).
148. A. Van der Ven, G. Ceder, M. Asta, and P. D. Tepesch, Physical Review B **64,** 184307(2001).
149. I. V. Belova, G. E. Murch, Intermetallics **6**, 115-119 (1998).
150. J. R. Nicholls, MRS bulletin **28**, 659 (2003).
151. F. Sauer, V. Freise, Z. Electrochem **66,** 353 (1962).
152. C. Wagner, Acta Met. **17**, 99 (1969).
153. J. Simons, *An Introduction to Theoretical Chemistry* (Cambridge University Press, 2003).